POLITECNICO DI TORINO

Master's Degree in Mechanical Engineering

Master's Degree Thesis

Torsional analysis of crank mechanism and Front End Auxiliary Drive system of a P0 hybrid powertrain for light duty application

Supervisors

Prof. Enrico GALVAGNO

Ing. Luca TIEZZI

Candidate

Luca COLANTONI

ID: 302525

October 2023

Master's Degree Thesis

Torsional analysis of crank mechanism and Front End Auxiliary Drive system of a P0 hybrid powertrain for light duty application

Supervisors	Candidate
Prof. Enrico GALVAGNO	Luca COLANTONI
Ing. Luca TIEZZI	ID: 302525

October 2023

Abstract

The automotive industry is currently undergoing a significant transformation due to increased attention to pollution levels. The European Commission is aiming for a zero-emission scenario by 2035, and as such, stricter EURO regulations will be implemented to achieve this goal. Light-duty vehicles and passenger vehicles are the primary focus of this process.
The compliance to the latest standards is strongly affecting to the engine mechanical design with the need to introduce new configurations. The most widely adopted solution is hybridization, which involves coupling an electric machine with an internal combustion engine. This requires a substantial redesign of the transmission system to manage torque split and accommodate the new architecture.
A case study from FPT Industrial involving the redesign of a light-duty engine with a new P0 hybrid engine is considered. The company's concern is understanding if the new design is compliant with their targets. It is a strong point of discussion because the P0 configuration introduces strong torques on the front-end auxiliary drive (FEAD) system.
After building a model for the crankshaft and the FEAD system, a torsional dynamic analysis will be performed to discuss whether the design is compliant to the targets. Furthermore, the introduction of two mechanical components, torsional vibrations damper (TVD) and vibrations decoupler, will be discussed. The TVD and the decoupler are the widest solutions to the problems introduced by the P0 hybrid design.
In the second part of the study the effect of the TVD and decoupler on company's targets will be assessed, showing their strong contribution in limiting the vibrations helping the two systems to be compliant to the requirements.

Acknowledgements

Vorrei ringraziare innanzitutto chi mi ha seguito durante questo progetto di tesi e ne ha permesso la realizzazione.
Il mio tutor aziendale Luca Tiezzi, è stato un supporto costante durante i sei mesi passati presso FPT Industrial. Mi ha trasmesso le sue conoscenze riguardo il tema trattato, iniziandomi all'approccio aziendale del System Engineering del quale rappresenta un punto di riferimento in tutta l'azienda.
Il gentilissimo professor Galvagno, è stato invece di grande supporto per conciliare l'approccio aziendale con quello accademico, più rigoroso. Nell'ultima parte del progetto il suo aiuto si è dimostrato indispensabile per lo sviluppo del codice MATLAB, uno dei capitoli di cui sono più orgoglioso.
Ci tengo a ringraziare i colleghi e, più in generale, l'azienda FPT Industial che mi ha ospitato per lo svolgimento di questo progetto mettendomi a disposizione le loro risorse e facendomi sentire a mio agio sin dall'inizio.
Un ringraziamento speciale va alla mia famiglia, che mi ha sempre sostenuto durante questi anni a Torino dandomi consigli preziosi nei momenti più difficili.
Infine, vorrei ringraziare tutti i miei amici, da quelli di lunga data, a quelli conosciuti in questi anni. La loro presenza ha rappresentato un posto sicuro dove trovare svago e supporto, indispensabili per trascorrere con serenità il mio percorso al Politecnico.

Table of Contents

List of Figures

Acronyms

EU: European Union
ATS: After treatment system
NOx: Nitrogen oxides
DOC: Diesel oxidation catalyst
HC: Hydro carbonates
DPF: Diesel particulate filter
CO: Carbon monoxide
ICE: Internal combustion engine
NVH: Noise, vibrations and harshness
EOM: Equations of motion
SDOF: Single degree of freedom
FRF: Frequency response function
FEAD: Front End Auxiliary Drive
TVD: Torsional vibrations damper
FEM: Finite element method
CAD: Computer aided design
ODE: Ordinary differential equation

Chapter 1

Introduction

The European Union is committed to achieving climate neutrality by 2050, delivering on the commitments under the Paris Agreement.
The Green Deal was introduced for reaching the 2050 goal. It is a package of policy initiatives which aims to set the EU on the path to a green transition with the goal of reaching climate neutrality by 2050. It underlines the need for a holistic and cross-sectoral approach in which all relevant policy areas contribute to the ultimate climate-related goal. The package includes initiatives covering the climate, the environment, energy, transport, industry, agriculture, and sustainable finance – all of which are strongly interlinked.
For what concerns the climate, energy and transport-related transitions, the Fit for 55 package was introduced aiming to put into law the ambitions of the Green Deal. The main focus of the Fit for 55 package is cutting the greenhouse gas emissions in the European union by at least of 55% by 2030 with respect to 1990 levels [1].
This process encompasses all the design aspects of the automotive industry, but the companies prioritize the solutions that maximize the emissions reduction while minimizing the costs. Before the implementation of the EURO 6 standard, an improved after treatment system (ATS) was the main strategy to comply with the new emissions limits. With the introduction of EURO 5 standard, spark ignition engines required an anti-particulate filter to reduce the number of particulate particles. For compression ignition engines, the latest requirements demanded a more complex ATS with the simultaneous action of three components: the selective

catalytic reduction (SCR) for NOx, the diesel oxidation catalyst (DOC) for HC and CO emissions, and the diesel particulate filter (DPF). These components rely on chemical reactions; thus, their efficiency was enhanced by researching on the materials involved. This process was sufficient to meet the EURO 6 standard, but the EURO 7 standard will impose even stricter limits that are now challenging the automotive industry. The new rules that will be effective by July 1st 2025 are paving the way towards the full electrification of the urban transportation means. Therefore, although the ATS efficiency is still relevant, the most effective design solution is the powertrain hybridization. The powertrain hybridization can limit the pollutant emissions of the internal combustion engine (ICE) by increasing the powertrain overall efficiency. There are two types of hybrid vehicles:

- Non-plug-in hybrids
- Plug-in hybrids

The first type is the simpler solution and involves an ICE connected to a small electric machine. This enables only a few electric features such as the energy recuperation during braking and the torque boost for larger electric machines. Even with these limited features, it still represents a good solution in terms of pollutant emissions because of the increased powertrain overall efficiency that reduces fuel consumption.
The plug-in hybrid configuration consists of an ICE connected to a larger electric machine that allows the full electric operation of the vehicle.
As the name implies, it can be externally charged and offers more features of an electric vehicle to the hybrid one. This solution is even better than the non-plug-in hybrid but is more complex to be implemented and therefore more expensive for the customer. As it can be inferred, these new designs require a new powertrain architecture and thus a redesign of the mechanical structure with possibly the addition of new mechanical components.
This study focuses on the redesign of the F1A engine from the company FPT Industrial from IVECO Group. F1A is an in-line 4 cylinder 2.3 liters diesel engine, one of the best selling engines of the company and it is used in the IVECO Daily light duty truck, the top selling product of IVECO.

Figure 1.1: FPT Industrial logo [2]

The company is redesigning this engine to comply with the EURO 7 standards by means of hybridization. The new application consists of a P0 hybrid engine.
In this type of hybrid architecture, the electric machine is coupled with the ICE by means of the front-end auxiliaries drive system (FEAD). The FEAD is the system composed of auxiliary pulleys that enables the power transmission from the engine to the auxiliaries. In the P0 architecture, one of the auxiliaries is the electric machine pulley that enables both the energy recuperation during braking and the boost contribution from the electric machine to the ICE. This type of hybrid is very challenging from the mechanical point of view because it requires a precise design of the FEAD system to allow the optimal performance of the electric machine. The resisting and motor torques introduced by the electric machine are the main concern of the project since they induce higher vibrations on the crank mechanism and FEAD systems with the possibility of structural or fatigue failure [3].
The design process needs to be compliant with the company guidelines from the system engineering approach to be satisfied for the starting the production. Therefore, for both the crank mechanism and the FEAD system, the design process based on the torsional analysis will be performed, assessing whether the systems meet the requirements and discussing the addition of certain mechanical components to improve the performance of the systems.

Chapter 2

System Engineering approach

FPT Industrial's design process is strictly linked to the system engineering approach, which main steps are summed up in the following V table.

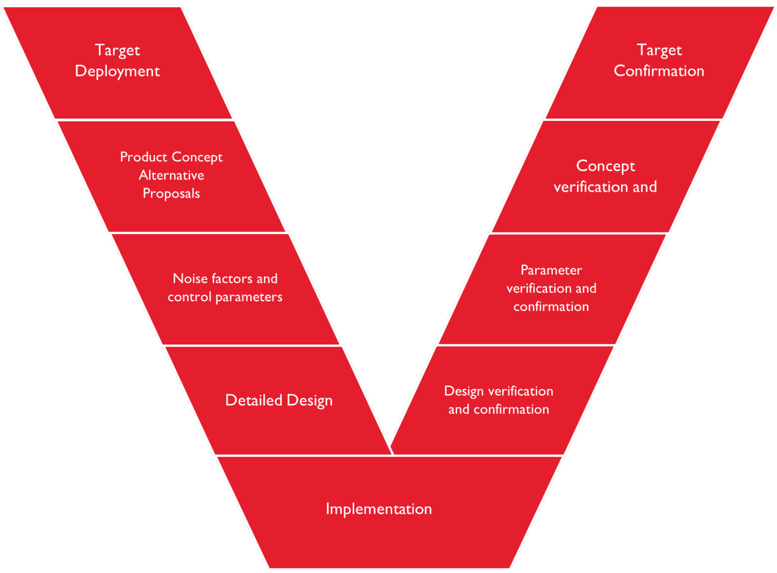

Figure 2.1: System Engineering desing process

The design process begins with the target definition for the system under analysis, generally based on the company's guidelines or the supplier experience.

A crucial phase is the evaluation of the alternative proposals from the internal design department or the external supplier. Once the best proposal is selected, a detailed design is specified based on the key parameters to act for the design. The implementation step connects the design part to the verification phase where the performance of the selected design are evaluated by means of virtual simulations or bench tests if necessary. The bench test is an expensive tool that is used only in case of doubtful values from the virtual validation phase, such as target not met or accurate evaluation of high-risk designs.
If all the steps just mentioned are completed, the company approves the proposed design and confirms the target defined at the beginning as adequate for that system. Since this case study focuses on an ongoing design, it will not be possible to follow the full path just described, mainly because bench tests are yet to be performed. Therefore, once the possible designs for the systems are described, a simulation model will be created, discussing the systems' compliance with the company targets already set.

2.1 Crank mechanism system

The crank mechanism is an essential component for every internal combustion engine. It is part of the power transmission system, and it is responsible in converting the reciprocating movement of the piston into a rotating movement to be sent to the transmission. It is mainly composed by the crankshaft and other mechanical components such as pistons, piston pin and connecting rods.

2.1.1 Components

The main part of the crank mechanism is the crankshaft which components are reported hereafter.

- Crankpin
  It is rigidly linked to the connecting rod, another mechanical component jointed to the piston that together with the crankpin allow the conversion from the vertical movement of the piston into a rotating one [4].

- Journals
  They are responsible to fix the crankshaft to the engine block by means of hydrodynamic bearings that allow the rotation of the shaft while constraining its position.

- Crank Web
  It is needed to connect the crankshaft to the journals. Its height determines half of the stroke of the cylinder.

- Crank web counterweights
  Additional inertial elements designed to limit the engine irregularities.

- Oil passage and oil seals
  They allow the correct lubrication to the bearing mounted on the journals.

- Flywheel mounting flange
  A flange at the end of the crankshaft that allows the connection of the flywheel by means of screws.

An example of crankshaft with a detail on each of its components is provided hereafter.

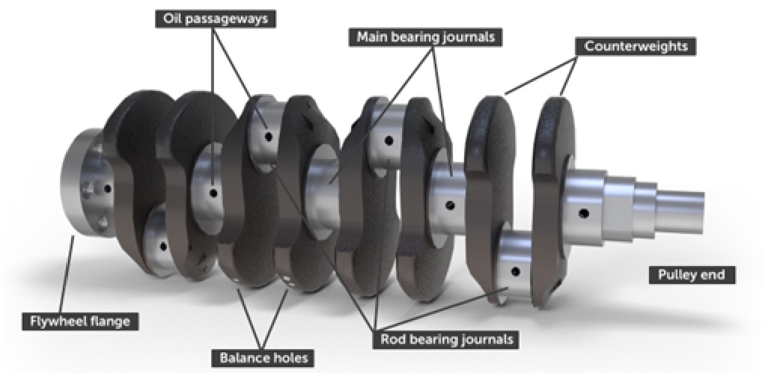

Figure 2.2: Example of crankshaft and its components [4]

In addition to the crankshaft, the crank mechanism is composed of the following elements, shown in figure 2.3.

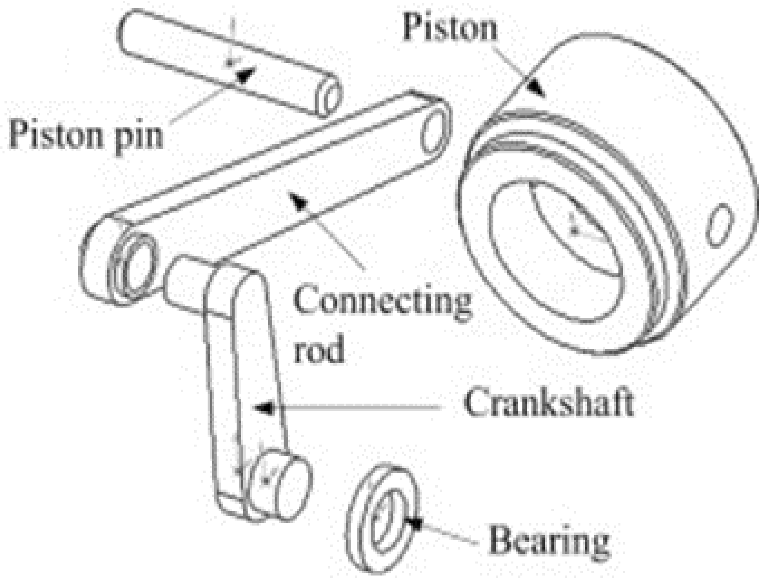

Figure 2.3: Example of crank mechanism and its components [5]

- Piston
  It is hit by the pressure from the combustion in the combustion chamber, it moves from the top dead center to the bottom dead center accordingly to the combustion process.

- Piston pin
  Joints the connecting rod to the piston, allowing a relative rotation movement.

- Connecting rod
  Joints the piston with the crankshaft generating the reciprocating movement.

2.2 Front-end auxiliaries drive system

The front-end auxiliaries drive system is a critical component in today's vehicles because it enables to send energy to the accessories such as the air conditioner, water pump and the alternator. The mechanical rotational power of the crank mechanism is transmitted to the auxiliaries by means of a belt mounted on the crankshaft front-end pulley and all the auxiliaries' pulleys. The belt tension is ensured by some idler pulleys. An example of FEAD system is shown in figure 2.4.

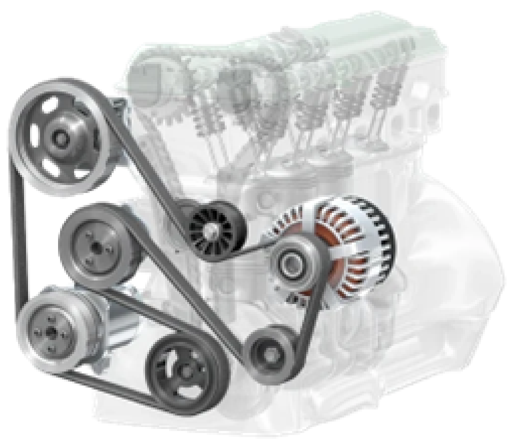

Figure 2.4: Example of FEAD system [6]

The design of these systems has always to deal with torsional vibrations to ensure the fatigue resistance of the belt. Furthermore, during the design it is crucial to define the position of the auxiliaries keeping compliant with the engine room and the correct transmission ratio to each pulley.

2.2.1 F1A P0 hybrid configuration

The FEAD system of the engine under analysis is quite different from the example just shown because of the P0 hybrid configuration. As anticipated, in this hybrid architecture the mechanical link between the ICE and the electric machine occurs at the FEAD system, thus introducing a pulley connected to the electric motor. For this application, the electric machine works as a belt starter generator (BSG). The BSG is a key element for non-plug-in hybrid applications. It replaces both the engine starter and the alternator, enabling the start and stop function, recuperation and boost phase and providing current to the air conditioner, thus reducing the number of pulleys in the FEAD.
For this specific application, the electric machine has a further function linked to the pollutant emissions. The battery is indeed used to provide current to the ICAT, an electric resistance module used to heat up the ATS when needed. This function provides lots of benefits from the emissions point of view. In fact, all the components of the ATS need a certain temperature to perform the chemical

reactions at the highest efficiency. The company noticed that during the typical duty cycle of this engine, which is mainly used for city shipping, it happened quite often that the ATS worked below the optimal temperature. To support this function, a powerful battery was needed. A 48V one was chosen for the purpose, the maximum battery size for non-plug-in hybrids.
However, the BSG introduces an elevated level of complexity in the design of the FEAD system because it generates high values of resistant and boost torques to enable the recuperation and boost phases, thus stressing more the belt. From the mechanical point of view, this solution required a new type of tensioner in the FEAD system. As shown in figure 2.4, for ICE applications, the tensioner pulley is fixed. However, considering the two different working conditions of the engine (boost and recuperation), the FEAD system has to change its equilibrium conditions according to the change of the torque from the BSG. This required the design of an automatic tensioner, able to rotate under the different loading conditions. In figure 2.5 an example of automatic tensioner for BSG applications from the company provider DAYCO is shown.

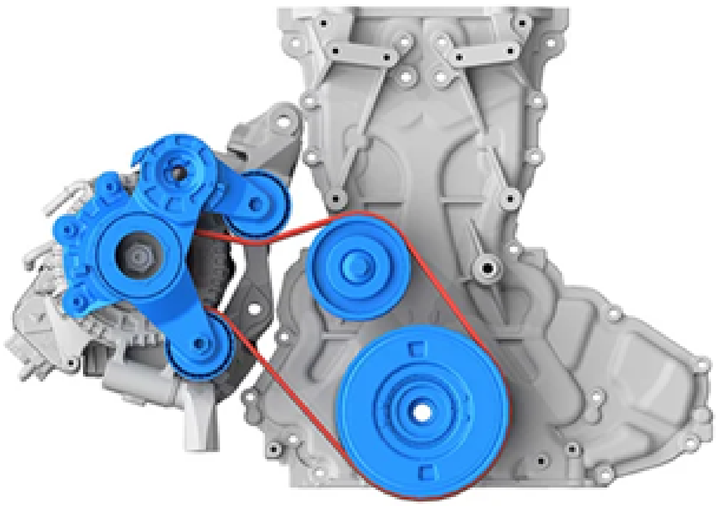

Figure 2.5: FEAD with BSG and automatic tensioner from DAYCO [7]

The automatic movement of the tensioner is achieved by means of a double rotational degree of freedom that are responsible for the higher complexity of the system.

2.3 System requirements

System engineering is heavily reliant on the definition of objectives for each system. As such, the primary crank mechanism, and the FEAD system objectives will be evaluated through virtual validation using GT-Ise.
A summarizing table, shown in figure 2.6, presents the objectives that will be discussed, which will then be explained in greater detail in subsequent paragraphs. For each of them the company crosses the product target influenced by the system target, e.g. an high external ring amplitude of the crankshaft influences the NVH of the engine.

System Target	Target value	Performance (Power & Torque)	Fuel Consumption	Emissions	NVH	Weight	Size / Packaging	Maintenance	Engine brake performance	Durability	Reliability	Startability	Serviceability Installation	Draveability
TVD External ring amplitude	0,5 °				x			x		x				
ternal torque	2640 N							x		x				
Global belt slippage	6%		x		x			x						
Tensioner movement-SIDE	10 °		x		x			x				x		
Tensioner movement-MAIN	10 °		x		x			x						
Average belt tension	2100 N				x			x				x		
x belt tension	4200 N							x				x		
n belt tension	> 0 N				x			x				x		
Hub load on auxiliaries pulleys	3200 N									x				
Slip torque	760 N							x		x		x		
fax flapping	10%				x			x			x			

Figure 2.6: Summarizing table of targets

2.3.1 External ring amplitude

The torsional vibrations amplitude is a key factor to be monitored when dealing with crank mechanisms, even more when a complex FEAD system is connected to the crankshaft. Nowadays a crucial component for the crank mechanism vibrations' control is the torsional vibrations damper (TVD). It is a component made of two inertia rings jointed with an elastomeric stiffness. It is placed on the front-end hub of the crank mechanism as shown in figure 2.7.

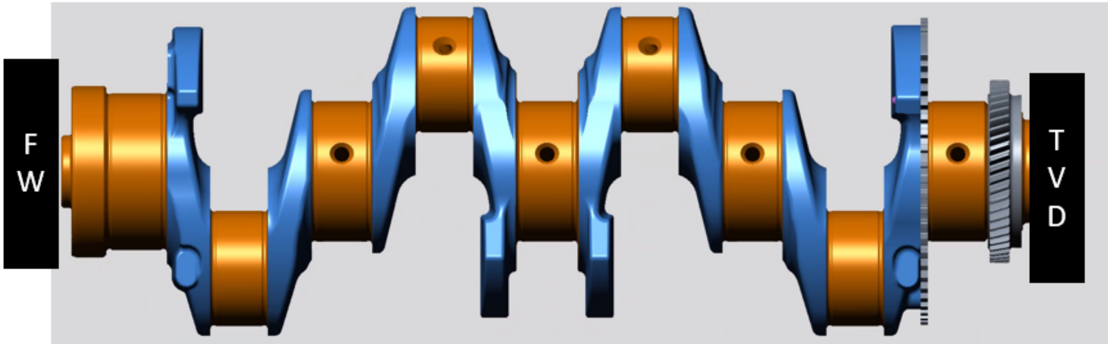

Figure 2.7: Schematic representation of crank mechanism with TVD applied

A detail on the assembly of a TVD is reported in figure 2.8.

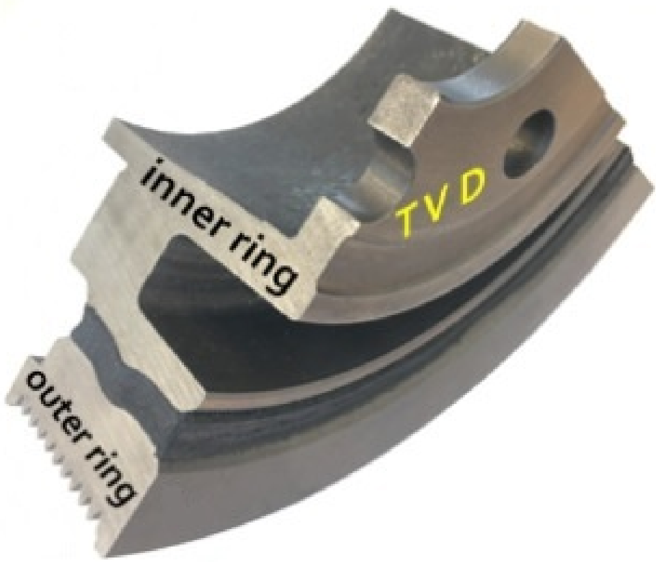

Figure 2.8: Section of a TVD highlighting internal and external rings

Its working principle will be discussed in specific in this chapter.
The company sets a target for the TVD external ring amplitude to make sure that the seismic inertia doesn't rotate over a certain limit both for NVH requirements and durability of the component itself.

2.3.2 Internal torque

For what concerns the crankshaft structural and fatigue verification, the company set a target on the internal torques allowable relying on its staircase testing.
The staircase testing method is based on applying increasing loading to the specimen until it breaks thus obtaining the fatigue limits even for a complex component such as the crankshaft.
Since it is based on reiterated tests on different specimens, this procedure has a strong statistic background, and its results are accepted with a certain reliability.
The fatigue limit is set by taking the mean value from the staircase method with a 50% of reliability, decreasing it of a further 10% of the standard deviation (red curve in figure 2.10). Figure 2.9 shows an example of this test on a cylindrical specimen.

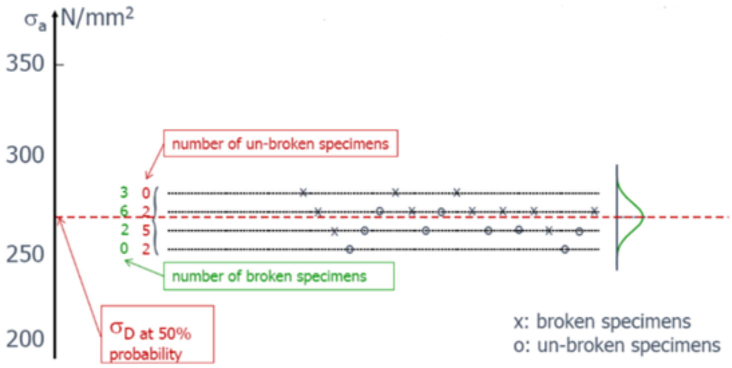

Figure 2.9: Example of staircase test on a cylindrical specimen

The staircase testing on the crankshaft in analysis led to the the Haigh diagram shown in figure 2.10, where the fatigue limits are related to the crankpins that happened to be the least resistant component under the torsional motion of the crankshaft.

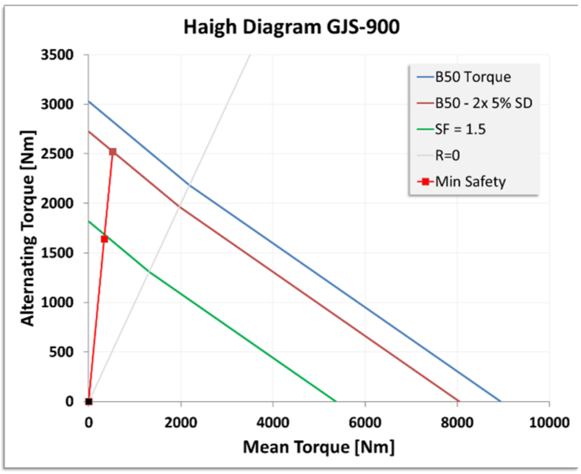

Figure 2.10: Crankshaft's Haigh diagram from staircase testing

The curves reported in figure 2.10 represent in detail:

- blue: mean value of fatigue limit from the staircase method with 50% of accuracy;
- red: mean value of fatigue limit reduced of 10% of the standard deviation;
- green: the acceptable limit for a safety factor =1.5.

2.3.3 Slip torque

In addition to monitoring internal torques for structural and fatigue verification of the crankshaft, it is also important to monitor the front-end slip torque. During the rotation of the crankshaft, the front-end pulley is subject to two torques, one from the engine, the other from the FEAD. These two torques are instantaneously equal and opposite the one to the other and the possibility of untightening the joint is to be considered.
Figure 2.11 shows a detail on the four-bolts front-end pulley joint and the two torques applied to that pulley.

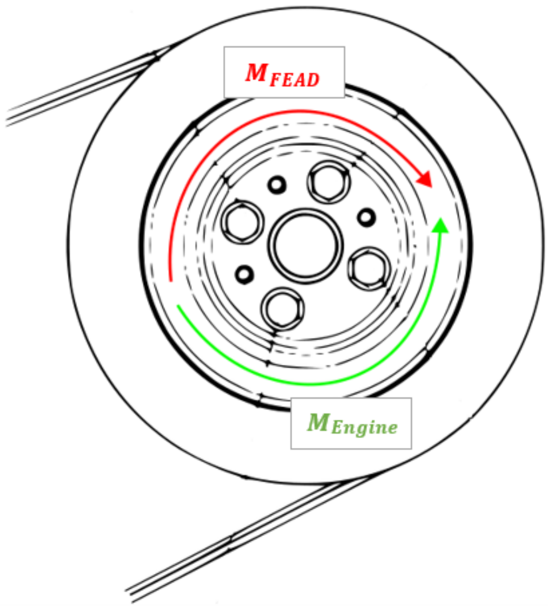

Figure 2.11: Torques acting on the front-end pulley

2.3.4 Pulley global slip

The FEAD system main requirement is the correct torque transmission. For this purpose, a crucial parameter is the pulley global slip. It considers how much each pulley is slipping with respect to the motor pulley, in this case the front-end pulley. The pulley global slip is measured in percentage and represent the relative speed difference between the front-end pulley and the pulley in analysis considering the transmission ratio as shown in equation 2.1.

$$\text{Pulley global slip } \% = \left| \frac{\omega_{\text{drv}} \cdot r_{\text{drv}} - \omega_i \cdot r_i}{\omega_{\text{drv}} \cdot r_{\text{drv}}} \right| \cdot 100 \tag{2.1}$$

2.3.5 Belt tension

For what concerns the belt life, the belt tension is the most important parameter to be considered both for dynamic and fatigue verification. For this reason, based on the belt producer's data a maximum belt tension was set as a target. Furthermore, the minimum tension allowable was set as grater than 0 N to guarantee the torque transmission.

2.3.6 Main and side arm peak-to-peak amplitude

While the above mentioned targets are always considered for the crank mechanism and FEAD system, these targets are specific for this type of FEAD system. Considering the mobility of the main plate and side arm the company set a maximum rotation value such that the configuration of the pulleys could work properly, also considering the maximum room available.

2.3.7 Hubloads

As shown in figure 2.12, the high torques introduced by the BSG pulley lead to high reaction forces on the pulleys' supports.

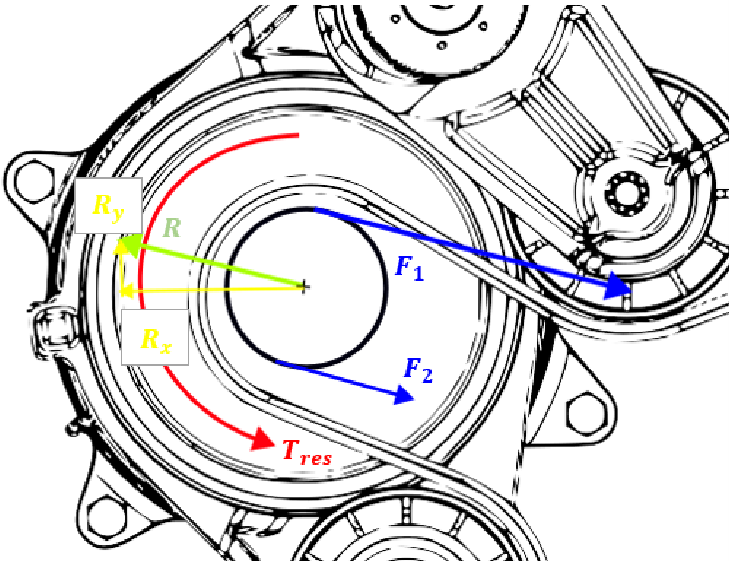

Figure 2.12: Free body diagram of the BSG pulley

This implied the definition of a maximum allowable force for the pulleys based on the structural and fatigue limits from the bearing's producer.

2.3.8 Flapping

Another point of attention for the belt safety is ensuring that its lateral movement is below a certain limit. The lateral movement is called flapping and it is computed in percentage as shown in equation 2.2.

$$\text{Belt flapping } \% = \left(\frac{\text{lateral displacement on pulley}}{\text{belt free span}}\right) \cdot 100 \tag{2.2}$$

where the belt free span is the length of belt that is not in contact to any pulley starting from the last touching point where the lateral displacement is evaluated. This concept can be clearly explained in figure 2.13.

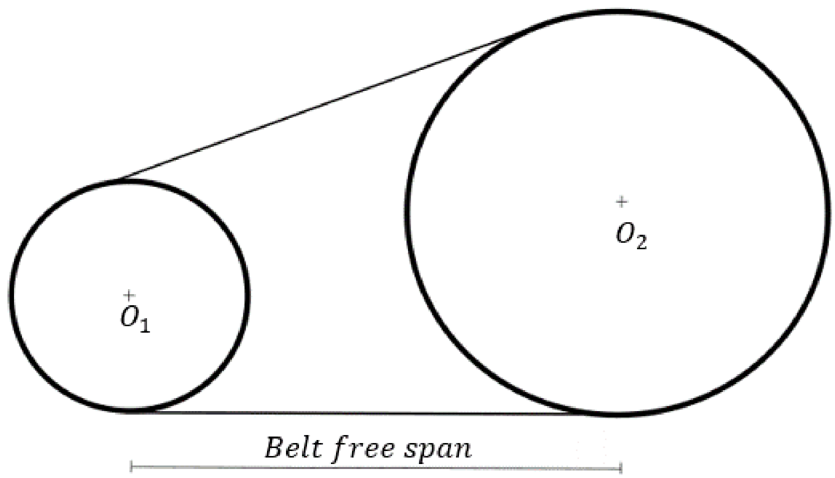

Figure 2.13: Detail on belt free span

2.4 Possible designs

2.4.1 Torsional dynamic damper

When addressing torsional vibrations in crankshafts, the primary concern is the amplitude of the vibrations. In the company's design process, a specific target for vibration amplitude at the front-end pulley must be met to ensure both fatigue resistance and optimal working conditions for the FEAD system, which is directly connected to the crankshaft.

To achieve it, a damping element must be incorporated into the design. In terms of crankshaft design, the most used component is the torsional dynamic damper (also called tuned mass damper or torsional vibration damper). This is typically applied to the front-end hub of the crankshaft to reduce the amplitude of torsional vibrations, but it requires precise tuning to achieve optimal performance [8].

2.4.2 Physical working principle

The torsional dynamic damper is an application of the tuned mass damper for torsional systems. The tuned mass damper is generally made of a spring and a mass to be added to a system but also a damping component should be considered in this case due to the elastomeric material.
Therefore, from a starting system, by adding a tuned mass damper, another degree of freedom is added increasing the complexity [9].
In figure 2.14 it is shown a simple mass-spring-damper single degree of freedom system to which a tuned mass damper is added.

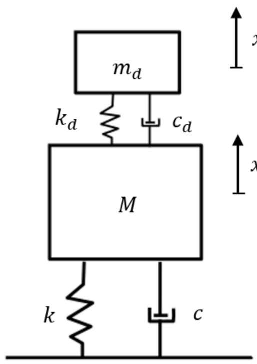

Figure 2.14: Single degree of freedom system with tuned mass damper

As can be stated from the drawing, the damper mass and stiffness are not of the same order of magnitude of the others in the system. Besides, the aim is to make the added mass move fast thus absorbing the kinetic energy of the main mass. In this way it is possible to achieve a damping action on the main mass while the seismic mass moves with high amplitude.
From the design perspective, the mass and the stiffness of the dynamic damper need to be finely tuned to get this effect. At the same time, it is also of interest to check whether the seismic mass is moving with an amplitude higher than the maximum allowed.

Starting from the single degree of freedom system, known its resonance frequency ω_{res} , the mass and the stiffness are tuned in such a way that:

$$\omega_{\text{res}} = \sqrt{\frac{k_d}{m_d}} \tag{2.3}$$

Therefore, a new single degree of freedom system is linked to the main one having a natural frequency equal to the resonance frequency to be canceled.
Performing the frequency response analysis of the system when the tuned mass damper is added, the effect of this component can be clearly evaluated solving the EoM 2.4.

$$\begin{bmatrix} M & 0 \\ 0 & m_d \end{bmatrix} \ddot{x} + \begin{bmatrix} c + c_d & -c_d \\ -c_d & c_d \end{bmatrix} \dot{x} + \begin{bmatrix} k + k_d & -k_d \\ -k_d & k_d \end{bmatrix} x = \begin{bmatrix} F(t) \\ 0 \end{bmatrix} \tag{2.4}$$

Where the generalized displacement vector x is:

$$x = \begin{bmatrix} x_1 \\ x_2 \end{bmatrix} \tag{2.5}$$

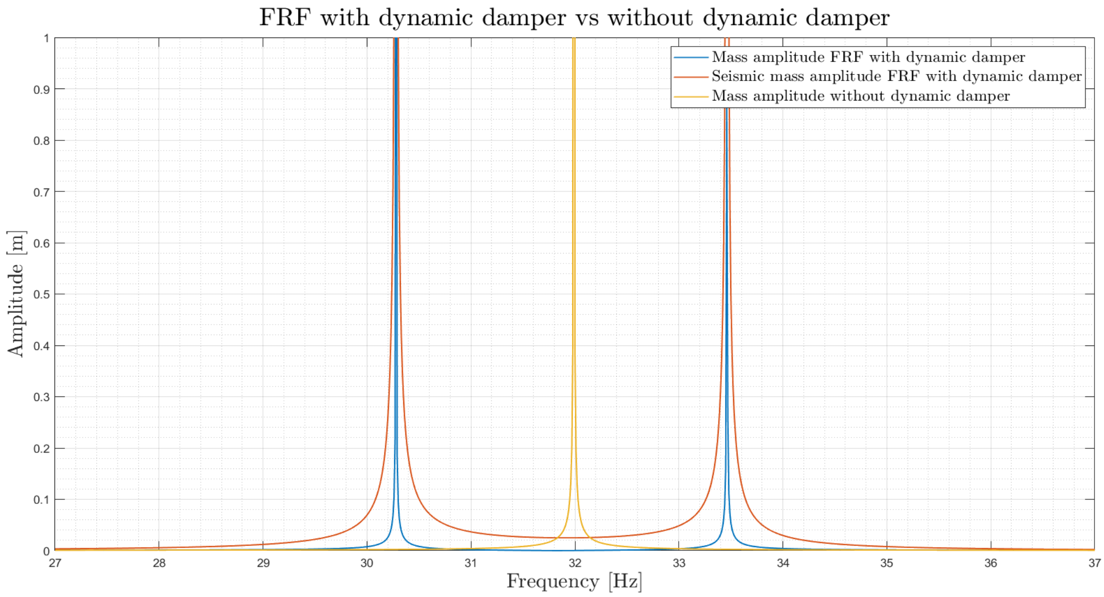

Figure 2.15: FRF comparison between SDOF with and without dynamic damper

As it can be seen in figure 2.15, the resonance peak becomes an anti-resonance with null amplitude, but two other peaks are introduced because there are now two degrees of freedom.
The design process is also focused on the magnitude of the stiffness and mass components. In fact, by keeping constant their ratio and increasing the seismic mass, it is possible to decrease the amplitude of vibrations of the seismic mass itself, it could be useful for certain applications. Another effect of this practice is that the two peaks move away from the anti-resonance as the seismic mass increases. A detail on the effect of the seismic mass is shown in figure 2.16.

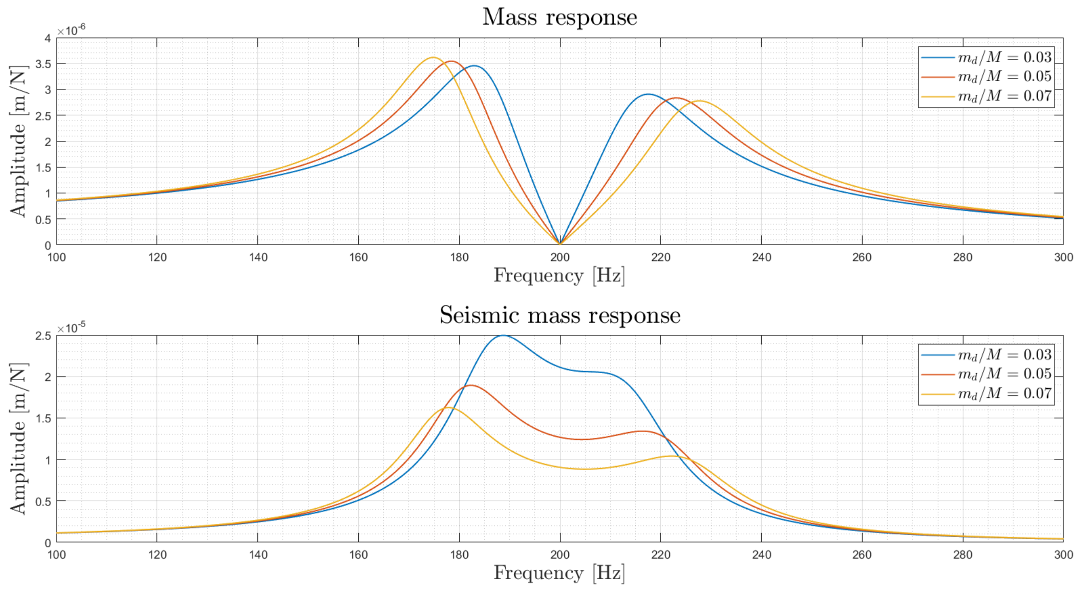

Figure 2.16: Seismic mass effect on tuned mass damper response

It is also possible to discuss the effect of the damping from the elastomeric material of the TVD stiffness. As figure 2.17 shows, that value of stiffness affects both the seismic and the main mass. The two peaks of the main mass decrease their amplitude and start to merge together while the amplitude of the seismic mass response decreases.

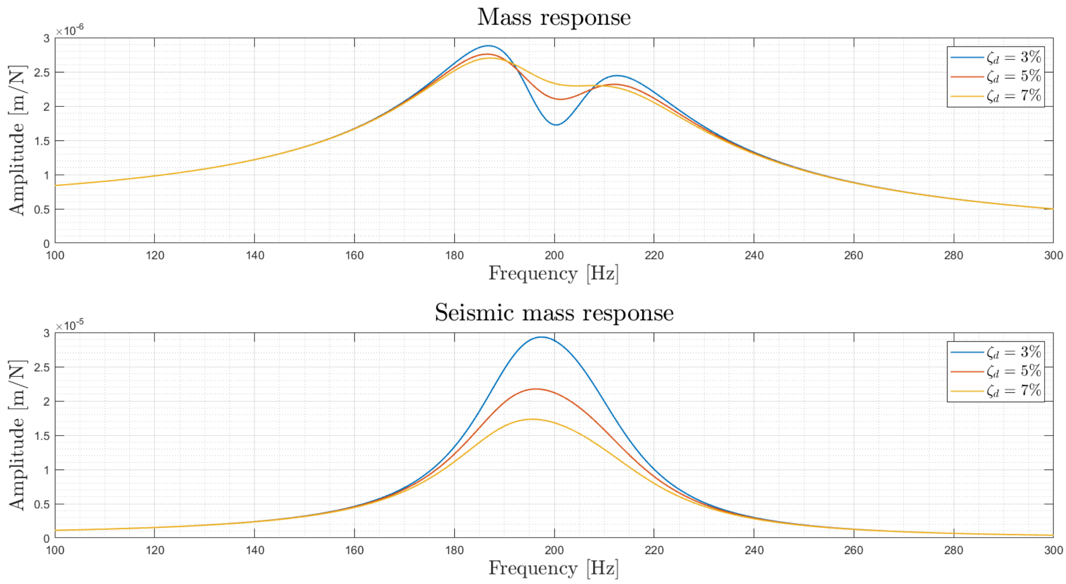

Figure 2.17: c_d effect on tuned mass damper response

This application is therefore ideal if the resonance appears inside the working frequency range as in crankshaft systems. As will be shown in chapter 3, due to the decomposition of the pressure profile with a sum of up to twenty harmonics, many external excitations are introduced thus many peaks that often happen to be inside the range of interest. At the same time, the crankshaft is made of many degrees of freedom that imply many resonance frequencies but in general only the first two imply peaks inside the working frequency range. Since it is common that a peak appears in the frequency range the TVD solution happens to be very popular in crankshaft systems' designing [10].
A torsional vibration damper is linked to the crankshaft at the front-end hub by means of an elastic ring that works as a stiffness, jointed to an external ring that introduces an inertia. An example of torsional vibration damper is shown in figure 2.18.

Figure 2.18: Example of real TVD [11]

As an alternative, it is also possible to use a torsional damper. It is the equivalent of a damper for non-rotating systems and generally the damping action is achieved by energy dissipation of a viscous fluid between inner and outer ring, as shown in figure 2.19.

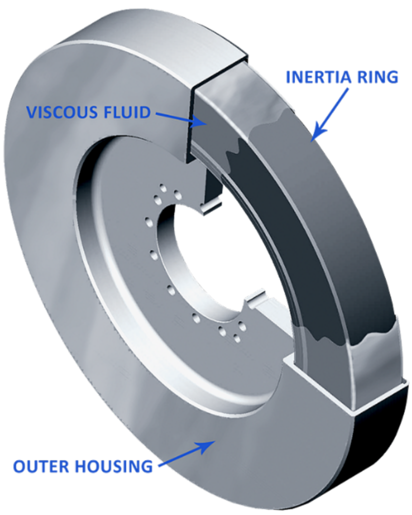

Figure 2.19: Example of viscous torsional damper [12]

For this application the equivalent mechanical system could be represented as in figure 2.20.

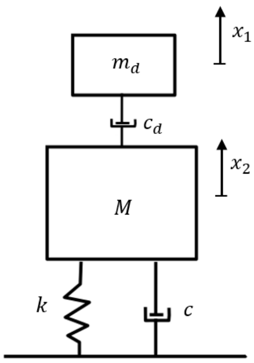

Figure 2.20: Single degree of freedom system with viscous damper

Which EoM can be written as reported in equation 2.6.

$$\begin{bmatrix} M & 0 \\ 0 & m_d \end{bmatrix} \ddot{x} + \begin{bmatrix} c + c_d & -c_d \\ -c_d & c_d \end{bmatrix} \dot{x} + \begin{bmatrix} k & 0 \\ 0 & 0 \end{bmatrix} x = \begin{bmatrix} F(t) \\ 0 \end{bmatrix} \tag{2.6}$$

This solution is used for heavy duty applications and allows to decrease the main mass amplitude of more than one resonance without creating other resonances, as shown in the FRF plot shown in figure 2.21.

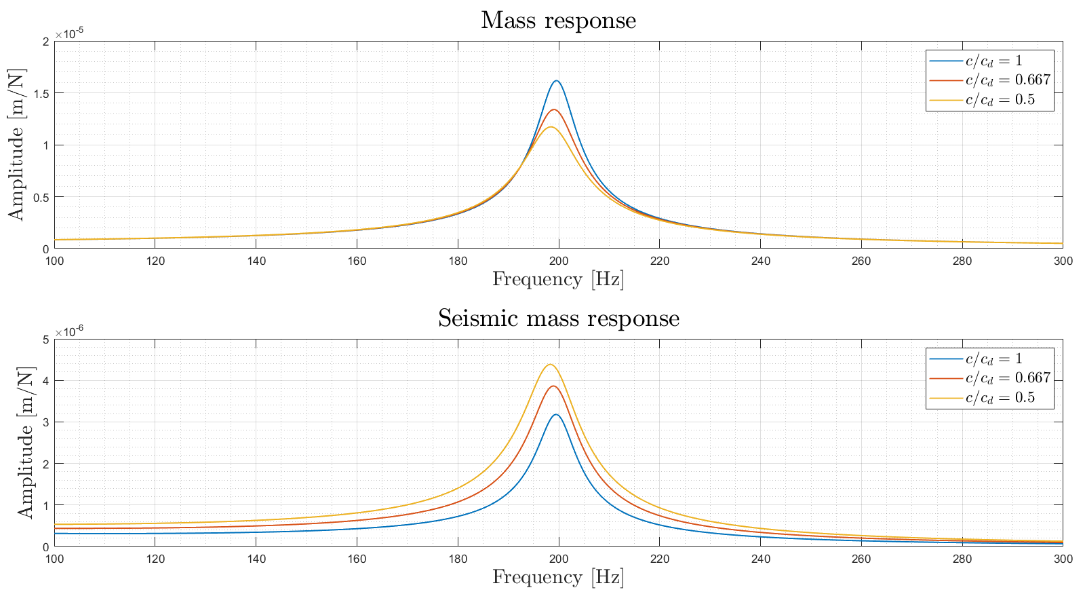

Figure 2.21: Viscous damping effect on peaks amplitude

Again, it is possible to increase the seismic mass if its response amplitude is too high, as reported in figure 2.22

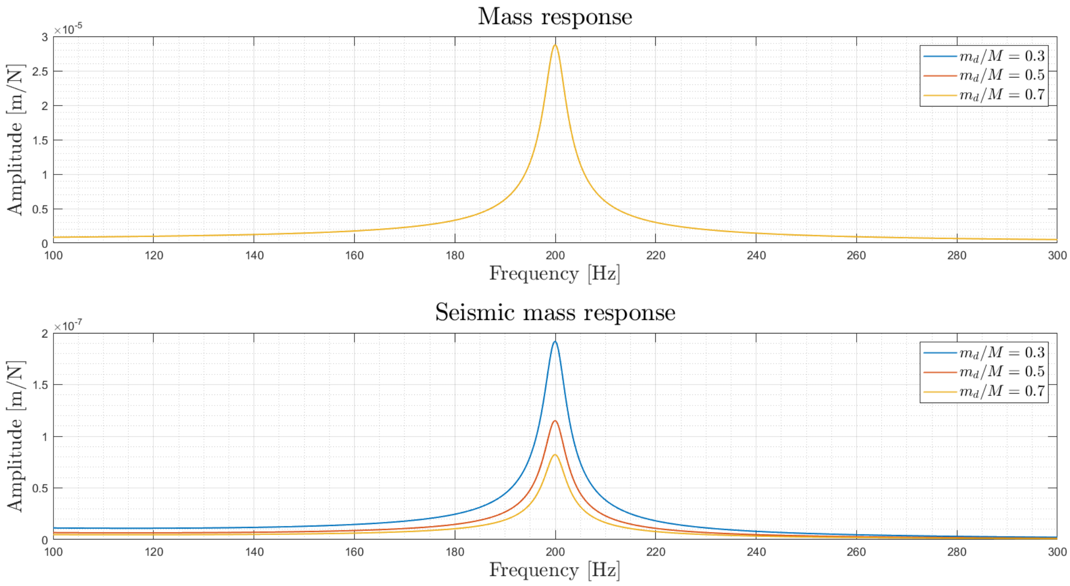

Figure 2.22: Seismic mass effect with viscous damper

2.4.3 TVD tuning procedure

As anticipated, the inertia-to-stiffness ratio between the internal and external rings of these mechanical components is a pivotal factor in optimizing performance. In this particular application, a rubber TVD is utilized, which precludes the possibility of fine-tuning the rubber stiffness to an exact value as recommended by best practices.

The design process typically initiated by suppliers takes into account the inertias of the TVD's inner and outer rings. These values significantly influence the system's natural frequencies and consequently, the frequencies at which resonances occur. The Campbell diagram of the crankshaft is constructed assuming a certain stiffness for the TVD. The initial assumption is based on a typical stiffness value for the application; generally, the TVD stiffness is orders of magnitude lower than that of the crankshaft. This aids in determining which natural frequency needs to be adjusted by introducing the TVD.

The Campbell diagram shown in figure 2.23, represents the natural frequencies of the undamped crank mechanism and their intersection with the tilted lines identifies a critical speed .
Therefore, the Campbell diagram is used to identify which natural frequency introduces more critical speeds in the frequency range of interest (in this case, 1000-4000 rpm).
This process is carried out considering only the most powerful harmonics - for a 4-cylinder engine, these are typically even ones, in accordance with the phasing of engine moments. In this application the most critical harmonic comes from order 8 that crosses the first natural frequency in the working frequency range with an external torque stronger than the ones from orders 6 and 10.

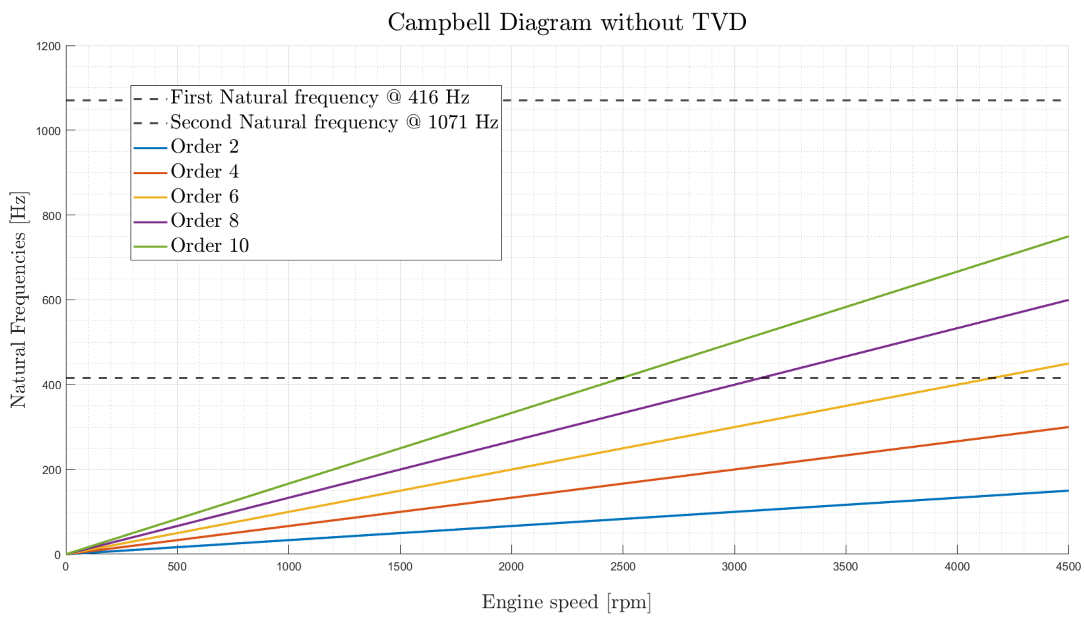

Figure 2.23: Example of Campbell diagram for TVD tuning

Upon establishing the tuning frequency, a more precise stiffness value can be calculated. However, due to the inherent limitations in the manufacturing process of the rubber stiffness, achieving optimal stiffness with high precision is unfeasible. Consequently, only a stiffness range can be realized.
Given this constraint, TVD suppliers typically establish a tolerance value around the natural frequency that needs to be adjusted. In this application, the supplier

set the tuning frequency to 270 ± 20 Hz, which value will be discussed in chapter 6. This value is not exactly equal to the first natural frequency since the damping is to be considered and it introduces a strong effect on the tuning process.
Another approach could be tuning the TVD on a frequency where a resonance occurs.

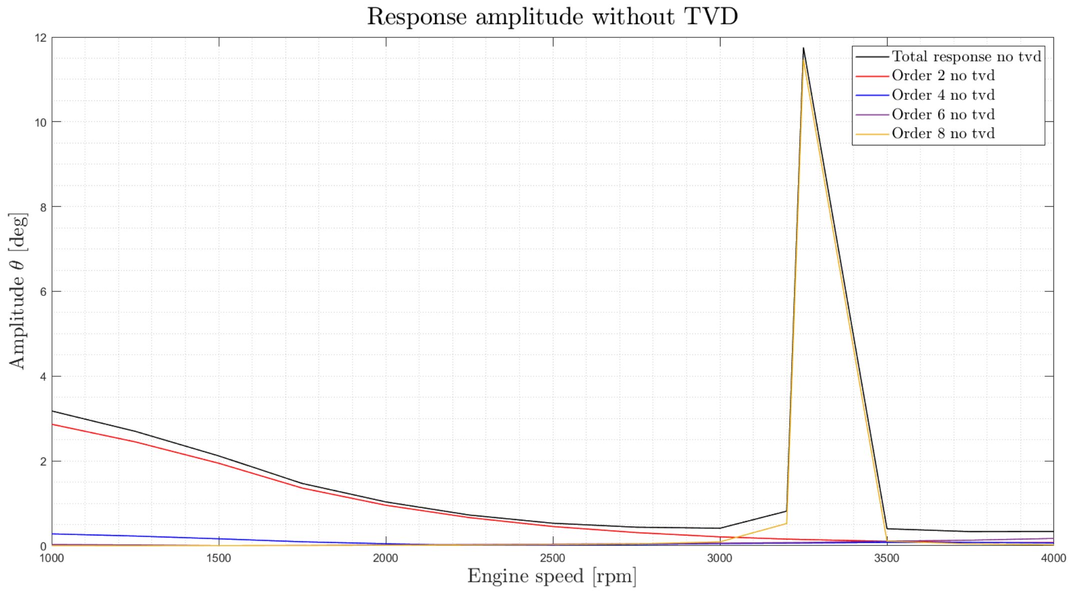

Figure 2.24: Crank mechanism hub response without TVD

Figure 2.24 shows the hub response simulated with the MATLAB model developed in chapter 6. A resonance peak, excited by the order 8 is highlighted at 3250 rpm. This engine speed could be translated into 433 Hz frequency of order 1. Therefore, the TVD could be tuned to that frequency instead of 270 Hz. However this approach will be proven to be not optimal because it is not based on the Campbell diagram, as it should be for rotating systems. In chapter 6, a comparison between the tuning at 270 Hz and 433 Hz will be shown.
In the next chapters it will be shown the positive effect of the TVD also on the internal torques in the crankshaft so to fulfill the requirements for fatigue loading.

2.5 Torsional decoupler

The torsional decoupler is a mechanical component that is becoming more and more popular in FEAD design. In the last years, the new engine design strategy is leading to the reduction of the idling speed to improve the fuel efficiency or, as for the case in analysis, to the introduction of P0 electric machines.
These solutions imply a strong increase of torsional vibration levels that increase the stresses brought to the FEAD system. The torsional decoupler is designed to limit this phenomenon and decrease the noises while the crankshaft is working [13].

Figure 2.25: Example of decoupler from DAYCO [14]

2.5.1 Physical working principle

The torsional decoupler is designed to act as a filter for the engine irregularities. This effect is achieved by introducing a rotational backlash.

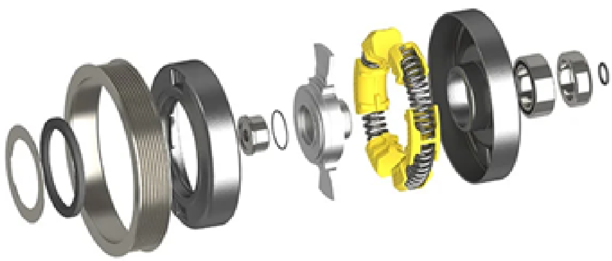

Figure 2.26: Detail on decoupler components from DAYCO [14]

The decoupler looks very similar to the TVD, made of an internal and an external ring jointed by means of a stiffness. The main feature of the decoupler is the type of stiffness that is used, where a spring with an hysteretic characteristic represents the best alternative. Figure 7.10 shows a possible torque vs angle characteristic of a decoupler stiffness.

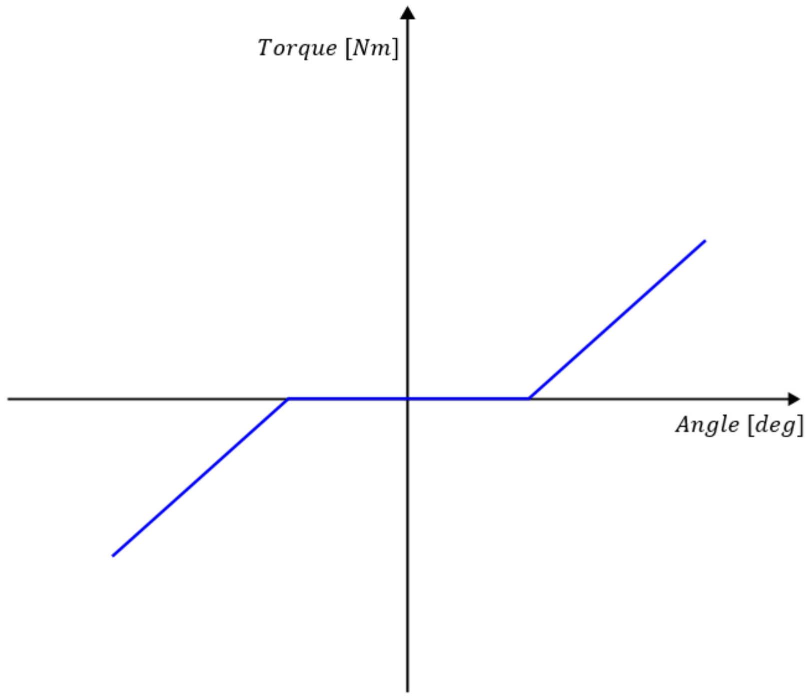

Figure 2.27: Example of a decoupler stiffness characteristic

The characteristic is designed according to the engine such that for low angles of rotation between the hub and the external ring no torque is transmitted since the energy is dissipated through the hysteretic cycle of the stiffness characteristic. Therefore, the decoupler uncouples the torsional motion towards the front-end side when the relative rotation between hub and external ring is too low thus cutting the engine irregularities that could damage the pulley system.
As shown in figure 7.10, this effect is achieved by means of a rotational backlash that transmits null torque for a set free angle to delete the torque transmission when it is not needed.
In figure 2.28 the engine speed at the internal ring of the decoupler and the external

one is compared.The picture shows a significant effect of the decoupler on the engine speed profile, narrowing the peaks leading to a lower irregularity.

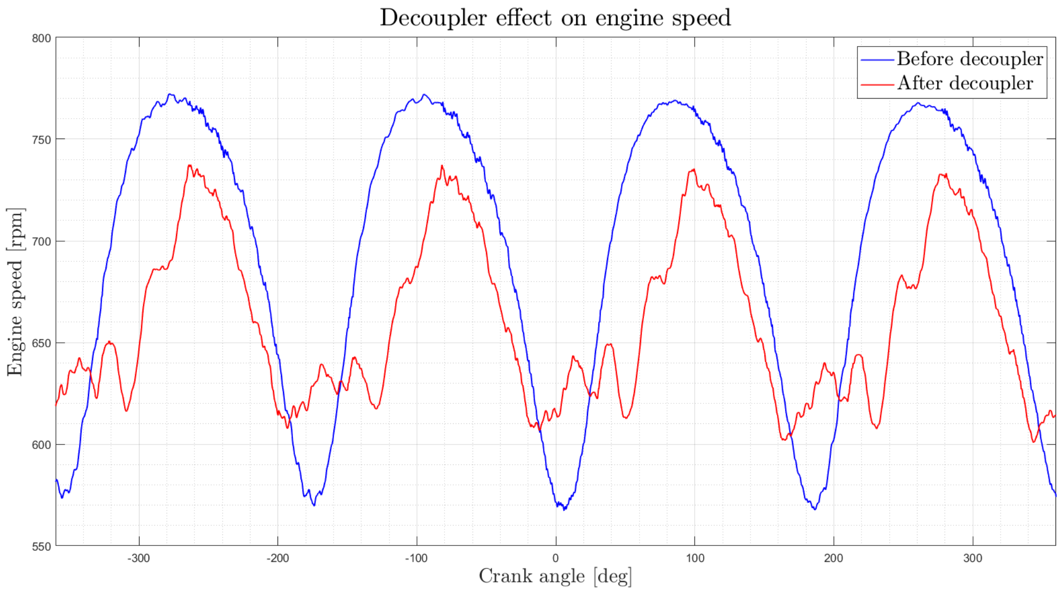

Figure 2.28: Decoupler effect on engine speed profile along a combustion cycle

This clarifies the positive effect introduced by the decoupler for everything that concerns the crankshaft dynamics and consequently the FEAD dynamics.

Chapter 3

Crank mechanism dynamic model for lumped parameters approach

The crank mechanism is a complex rotating machine that contains reciprocating components, resulting in dynamic problems. The design process is often arduous, and it may not always be possible to ensure optimal working conditions, as happens for machines containing only rotating elements. In some cases, even significant vibrations cannot be mitigated, necessitating extensive experimentation to achieve acceptable vibration amplitudes.
One of the primary challenges in the design of crank mechanism arises from the inherent asymmetry of the system, which may lack any symmetry planes. Unlike rotors, crank mechanisms cannot be precisely balanced, resulting in non-zero inertia forces and complicating the mitigation of vibrations. This precludes the uncoupling of axial, torsional, and flexural behavior typically applied to beam-like elements.
The complexity of crank mechanism design is further compounded by the presence of external forces and the forces exerted by hot gases on the pistons of internal combustion engine (ICE). These contributions are not harmonic but periodic, necessitating the remodulation of external excitation through a Fourier transform of the signal into a sum of harmonic components with frequencies that are multiples

or rational fractions of the machine's rotational speed.
From a design standpoint, the dynamic analysis of a crank mechanism focuses on torsional modes that generate the most hazardous vibrations. Consequently, during the design process, torsional vibrations are treated as uncoupled from axial and flexural vibrations, despite this being a crude approximation.
This approach is justified as it avoids introducing additional complexity into the physical model while still accounting for the most significant contributions to vibration amplitude.
Therefore, the design process often involves parallel experimentation to ensure that strong vibrational contributions from bending and axial modes are not being neglected [10].

3.1 Equations of motion

The analysis of torsional vibrations typically involves the construction of an equivalent lumped parameter torsional system, comprising a number of flywheels equal to the number of crank mechanisms, interconnected by straight shafts as depicted in the figure below.

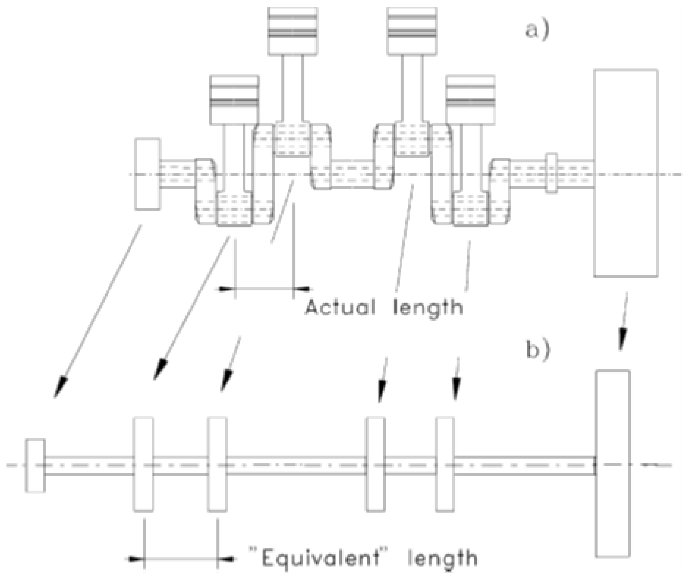

Figure 3.1: Crank mechanism equivalent lumped model [10]

The shaft connecting the flywheels are defined with a constant section and an equivalent length such that their torsional stiffness matches the one of their referring bank. This equivalent system allows to study the torsional behaviour separately from axial and bending modes.
The characterization of the equations of motion (EoM) will be performed by means of the Lagrangian approach based on a referring simple crank mechanism reported in figure 3.2. It is composed of a disc, with a crankpin in B on which the connecting rod PB, whose center of mass is G, is articulated. It may happen that the line of motion of point P is not passing through the axis of the shaft so, an offset d will be introduced even if it is assumed small. Assuming:

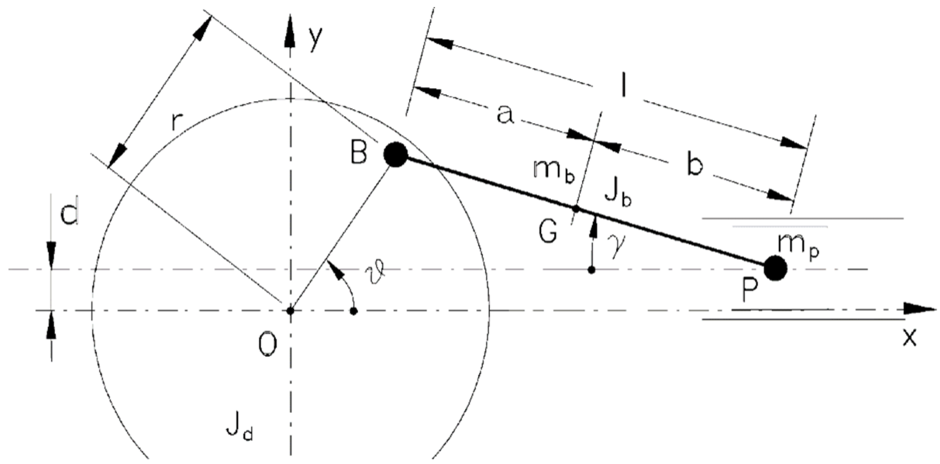

Figure 3.2: Model for representing the crank mechanism [10]

- J_d moment of inertia of the disk;
- J_b moment of inertia of the connecting rod about is center of mass G;
- m_b mass of the connecting rod;
- m_p mass of piston and piston pin.

The coordinates of points B,G and P can be expressed with respect to the O_{xy} reference frame as a function of the crank angle θ.

$$\overline{(B-O)} = \begin{pmatrix} r\cos(\theta) \\ r\sin(\theta) \end{pmatrix} \tag{3.1}$$

$$\overline{(G-O)} = \begin{pmatrix} r\cos(\theta) + a\cos(\gamma) \\ r\sin(\theta) - a\sin(\gamma) \end{pmatrix} \tag{3.2}$$

$$\overline{(P-O)} = \begin{pmatrix} r\cos(\theta) + l\cos(\gamma) \\ d \end{pmatrix} \tag{3.3}$$

where it is possible to link the angle γ to θ by the equation 3.4:

$$r\sin(\theta) = d + l\sin(\gamma) \tag{3.4}$$

that implies:

$$\sin(\gamma) = \alpha\sin(\theta) - \beta \tag{3.5}$$

where α and β are defined as:

$$\alpha = \frac{r}{l} \quad \text{and} \quad \beta = \frac{d}{l} \tag{3.6}$$

The Lagrangian approach build the mass matrix of the system by computing the total kinetic energy of it. For a crankshaft system, there are two contributions to the kinetic energy: the rotational and the translational kinetic energies.

<u>Disk</u>

The rotational kinetic energy of the disk is:

$$T_d = \frac{1}{2}J_d\dot{\theta}^2 \tag{3.7}$$

<u>Piston</u>

The rotational kinetic energy of the piston is:

$$T_p = \frac{1}{2}m_pV_p^2 \tag{3.8}$$

It is evaluated starting from the piston velocity by differentiating the equation 3.9 with respect to time.

$$V_p = -r\dot{\theta}\sin(\theta) - l\dot{\gamma}\sin(\gamma) = -r\dot{\theta}\left[(1 + \frac{\alpha\cos(\theta)}{\cos(\gamma)})\sin(\theta) - \frac{\beta\cos(\theta)}{\cos(\gamma)}\right] \tag{3.9}$$

Considering that V_p is related to $\dot{\theta}$ it is possible to define a function $f_1(\theta)$ that allows to write the kinetic energy of the reciprocating masses as:

$$T_p = \frac{1}{2} m_p r^2 \dot{\theta}^2 f_1(\theta) \tag{3.10}$$

where:

$$f_1(\theta) = \left[(1 + \frac{\alpha \cos(\theta)}{\cos(\gamma)}) \sin(\theta) - \frac{\beta \cos(\theta)}{\cos(\gamma)} \right]^2 \tag{3.11}$$

Connecting rod

For what concerns the connecting rod, since it is roto-translating its total kinetic energy is again composed of a rotational and translational terms that can be easily evaluated by building a lumped parameter system that splits the two contributions. The lumped equivalent system can be represented as in figure 3.3.

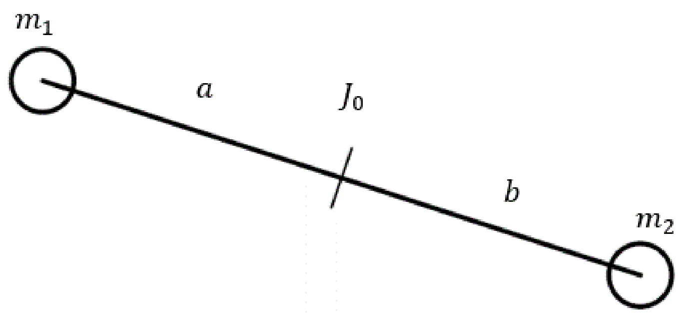

Figure 3.3: Sketch of the lumped parameter model of a connecting rod [10]

Therefore, the equivalent parameters of the connecting rod are computed imposing that the total mass of the equivalent system is m_b:

$$m_b = m_1 + m_2 \tag{3.12}$$

$$m_1 = m_b \frac{b}{l} \tag{3.13}$$

$$m_2 = m_b \frac{a}{l} \tag{3.14}$$

$$J_0 = J_b - (m_1 a^2 + m_2 b^2) = J_b - m_b a b \tag{3.15}$$

These three parameters contribute to three different kinetic terms:

- m_1 is fixed on the disk so it is only rotating;
- m_2 is fixed on the piston so it is only translating;
- J_0 is rotating with a rotational speed $\dot{\gamma}$.

To keep the total kinetic energy as a function of only one rotational speed, it is possible to define another function of θ , $f_2(\theta)$ so that:

$$T_{J_0} = \frac{1}{2} J_0 \dot{\gamma}^2 = \frac{1}{2} J_0 \dot{\theta}^2 f_2(\theta) \tag{3.16}$$

where:

$$f_2(\theta) = \alpha^2 \left(\frac{\cos(\theta)}{\cos(\gamma)} \right)^2 \tag{3.17}$$

Therefore, the total kinetic energy of the system is made of three contributions:

1. Rotation of disk and the fixed mass m_1;
2. Rotation of the connecting rod;
3. Translation of the piston mass and the fixed mass m_2.

Therefore, the total kinetic energy can be written as a function of $f_1(\theta)$, $f_2(\theta)$ and $\dot{\gamma}$ as:

$$T = \frac{1}{2}\dot{\theta}^2 \left[J_d + m_1 r^2 + (m_2 + m_p) r^2 f_1(\theta) + J_0 f_2(\theta) \right] = \frac{1}{2} J_{eq}(\theta) \dot{\theta}^2 \tag{3.18}$$

where $J_e q(\theta)$ is an equivalent moment of inertia that allows to describe the whole system's kinetic energy as a function of the angular velocity $\dot{\gamma}$.
When dealing with torsional vibrations, the motion of each section of the crankshaft can be expressed as a superimposition of a rigid-body rotation with angular velocity Ω and a vibrational motion expressed by the torsional rotation $\phi_z(t)$. The angle θ is therefore:

$$\theta(t) = \Omega t + \phi_z(t) \tag{3.19}$$

and the kinetic energy (3.18) is:

$$T = \frac{1}{2} J_{eq}(\theta)(\Omega + \dot{\phi}_z)^2 \tag{3.20}$$

The interesting quantity for vibration analysis is the deviation from steady state speed $\dot{\phi_z}$ so, applying the Lagrangian approach to a single crank, the following EOM will come up:

$$J_{eq}\ddot{\phi}_z + \frac{1}{2}(\Omega + \dot{\phi}_z)^2 \frac{\partial J_{eq}(\theta)}{\partial \theta} = M \tag{3.21}$$

where M is the external moment on the crank including elastic and damping terms and force applied on the piston.
The equation 3.21 is a second-order differential equation in ϕ_z where the derivatives of Ω with respect to time vanish because we assume a constant engine mean speed. Since M is a function both of time and ϕ_z the approach is based on some simplifications of the EoM (3.22) aiming to get a linear differential equation with constant coefficients.
The first simplification is to replace the variable moment of inertia with two contributions: a constant and a variable one. The variable will be accounted as an external contribution that is exciting the system and it will be discussed later, for now it will be put inside the external moment M. This approach substitutes each crank with a constant moment of inertia and external inertia torques variable in time, acting together with the external forces due to the working fluid and the other parts of the system.
Furthermore, the angle ϕ_z is assumed to be small enough to be neglected in the expression of θ. The equation consequently reduces to:

$$\overline{J_{eq}}\ddot{\phi}_z = M - \frac{1}{2}\Omega^2 \frac{\partial J_{eq}(\Omega t)}{\partial(\Omega t)}. \tag{3.22}$$

$\overline{J_{eq}}$ and the external inertia torques are computed by resorting to the series expansions of functions $f_1(\theta)$ and $f_2(\theta)$ which can be expressed as trigonometric series of angle θ as a function of nondimensional parameters α and β, as expressed in equations 3.23 and 3.24.

$$f_1(\theta) = a_0 + \sum_{i=1}^{7} a_i \cos(i\theta) + \sum_{i=1}^{6} b_i \sin(i\theta) \tag{3.23}$$

$$f_2(\theta) = c_0 + \sum_{i=1}^{7} c_i \cos(i\theta) + \sum_{i=1}^{6} d_i \sin(i\theta) \tag{3.24}$$

The plot of the two series in figure 3.4 that the trigonometric series lead to a perfect approximation of $f_1(\theta)$ and $f_2(\theta)$. These results are obtained by considering seven $\cos(\theta)$ terms and six $\sin(\theta)$ terms.

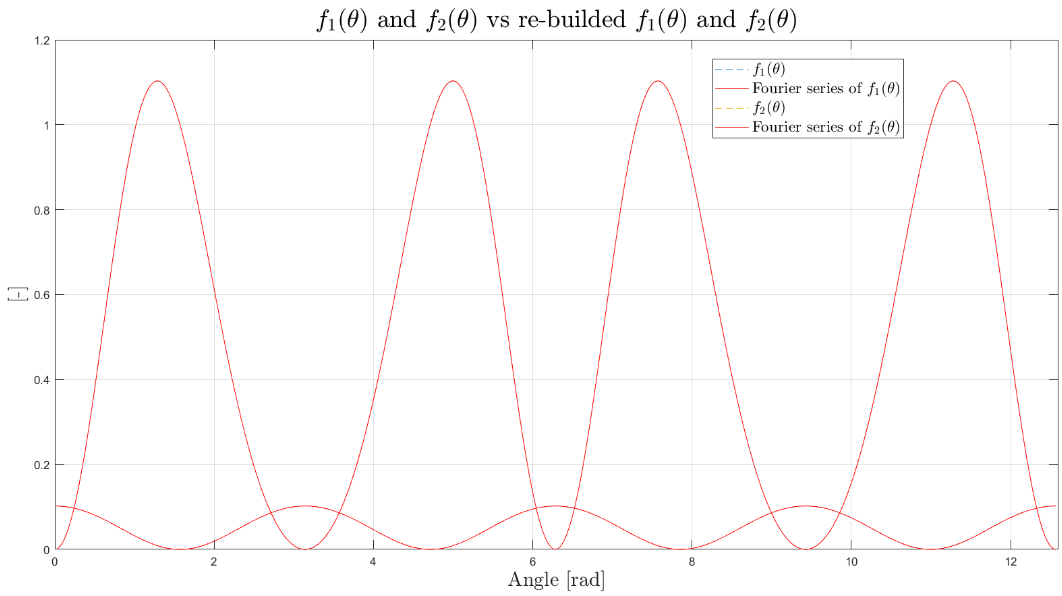

Figure 3.4: $f_1(\theta)$ and $f_2(\theta)$ vs re-builded $f_1(\theta)$ and $f_2(\theta)$

Under this approach the equivalent moment of inertia can be written as:

$$J_{eq} = \overline{J_{eq}} + \sum_{i=1}^{7} J_{c_i} \cos(i\theta) + \sum_{i=1}^{6} J_{s_i} \sin(i\theta) \tag{3.25}$$

where:

$$\overline{J_{eq}} = J_d + m_1 r^2 + a_0(m_2 + m_p) r^2 + J_0 c_0 = J_d + m_1 r^2 + \frac{(m_2 + m_p)}{2} r^2 \tag{3.26}$$

$$J_{c_i} = a_i (m_2 + m_p) r^2 + J_0 c_i \tag{3.27}$$

$$J_{s_i} = b_i(m_2 + m_p)r^2 + J_0 d_i \tag{3.28}$$

The method just presented can lead to very rough estimations of the crankshaft behaviour if the inertia forces due to reciprocating masses are high. Still, it represents a valid approach mainly because the design of these systems aims at reducing the mass of reciprocating elements. Furthermore, this approach represents the only one that allows to predict the behaviour of a complex machine without resorting to more complex and demanding Multibody-FEM simulation.
Since the accuracy is still good, many simulations softwares are based on this approach, including the one used for the simulations for this project.

3.2 Forced vibrations

In general, reciprocating machines are loaded by forces variable in time which often excite torsional vibrations of the shaft. As mentioned in the free vibrations part, under the made assumptions, the variable component of the inertia torque is considered as an external forcing function. Therefore, the total external moment will be variable in time with a known time history made of the sum of a driving torque and the inertia torque acting on each flywheel of the equivalent system.
For what concerns the driving torque, the pressure of the gases in the cylinder is a function of time and can be treated with the Lagrangian approach by means of the virtual work that introduces as states the equation 3.29 where δs is the virtual displacement that corresponds to $\delta\theta$:

$$\delta s = \frac{V_p}{\dot{\theta}}\delta\theta, \quad \delta L = p(t)A\delta s = p(t)rA\sqrt{f_1(\theta)}\delta\theta \tag{3.29}$$

Where $f_1(\theta)$ is defined in the equation 3.11. Therefore, the driving torque function can be obtained by deriving with respect to δs:

$$M_m(t) = \frac{d(\delta L)}{d(\delta\theta)} = p(t)Ar\left[\left(1 + \frac{\alpha\cos(\theta)}{\cos(\gamma)}\right)\sin(\theta) - \frac{\beta\cos(\theta)}{\cos(\gamma)}\right] \tag{3.30}$$

As done for the internal moment coming from the variability of the crankshaft inertia this moment is modeled by means of the Fourier transform so that it is possible to model a periodic excitation into a sum of a high number of harmonics.

It follows:

$$M_m(t) = A_0 + \sum_{k=1}^{m} A_k \cos(k\Omega' t) + \sum_{k=1}^{m} B_k \sin(k\Omega' t) \tag{3.31}$$

where:

$$A_0 = \frac{1}{2\pi} \int_0^{2\pi} M_m d(\Omega' t) \tag{3.32}$$

$$A_k = \frac{1}{\pi} \int_0^{2\pi} M_m \cos(k\Omega' t) d(\Omega' t) \tag{3.33}$$

$$B_k = \frac{1}{\pi} \int_0^{2\pi} M_m \sin(k\Omega' t) d(\Omega' t) \tag{3.34}$$

And m=20 should an enough number harmonics for an accurate description of the motor torque. This number will be discussed in the MATLAB model chapter with data from the F1A application.
Or alternatively, with the exponential formulation:

$$M_m(t) = \sum_{k=1}^{m} M_{m_k} e^{i(k\Omega' t + \Phi_{m_k})} \tag{3.35}$$

Where M_{m_k} is the amplitude of the harminic k of the driving torque and ϕ_{m_k} is the phase of the harmonic k of the driving torque that are defined from the above mentioned integral formulations as follows:

$$M_m(t) = \sum_{k=1}^{m} M_{m_k} e^{i(k\Omega' t + \Phi_{m_k})} \tag{3.36}$$

$$\Phi_{m_k} = \arctan\left(\frac{A_k}{B_k}\right) \tag{3.37}$$

An important mention is about the fundamental harmonic Ω'. It is strictly correlated to the pressure cycle period and must be linked to the mechanical behavior discussing the type of combustion. It represents a link between the thermal and mechanical behavior of the engine. It is defined for two-strokes or four-strokes engines as:

- $\Omega' = \Omega$ for two-strokes engines;
- $\Omega' = \frac{\Omega}{2}$ for four-strokes engines;

These relations are justified because in two-strokes-engines p(t) is periodic with fundamental frequency equal to the rotational velocity Ω of the shaft. Differently,

in four-strokes engines the period of the function p(t) is doubled implying half of the fundamental frequency i.e. $\frac{\Omega}{2}$.
Considering an in-line four cylinder engine with time evenly spaced cylinder, the cranks that fire subsequently must make an angle of $\frac{4\pi}{4}$, implying a configuration of the crankshaft with 180° angle between subsequent cylinders.
This configuration guarantees the best balancing of inertia forces that can be even improved reshaping the crank webs with an addition of weights, as done in the F1A crankshaft.
For the thermal optimization of the cylinders, a firing order is chosen to prevent those two contiguous cylinders are not firing immediately one after the other.
Thus, even if it is impossible to guarantee it for a four-cylinder engine, the widest used firing orders are generally 1-3-4-2 or 1-4-3-2.

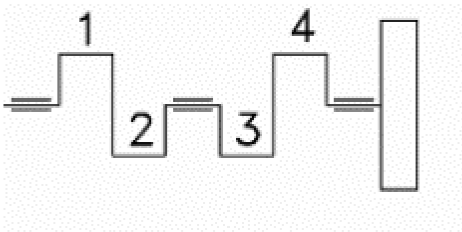

Figure 3.5: Sketch of an in-line 4-cylinders crankshaft with 1-3-4-2 firing order

A temporal displacement in the combustion process of each cylinder results in n sequential thermodynamic combustion cycles, where n represents the number of cylinders. This enables the calculation of a phase angle to account for the fact that the engine torque is composed of the superposition of all torques acting on the crankshaft, taking into consideration the delay between them.
The phase angle δ is computed as:

$$\delta = \frac{720°/2}{n} = 90° \text{ for four-cylinder 4-stoke engines} \tag{3.38}$$

This concept is summed up in the star diagram of the engine that allows to understand how many cylinders are contributing to the motor moment for each harmonic.

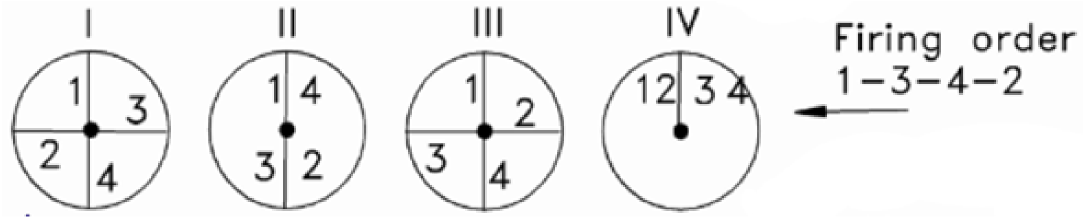

Figure 3.6: Star diagram for a four-cylinder engine with firing order 1-3-4-2

As illustrated by the star diagram, at each even harmonic, the contributions of different cylinders superimpose. Specifically, at every two multiples of k, at least two cylinders provide an in-phase torque, while at every four multiples of k, all four contributions are in phase, thus introducing a stronger external moment.
This is a crucial concept from a design perspective as it predicts which harmonic orders pose the greatest risk. For a four-cylinder engine, the most hazardous harmonic is the fourth, referred to as order two. As the harmonics progress, their contribution to the total engine torque decreases due to the Fourier decomposition of the pressure cycle.
This implies that even though the eighth harmonic is composed of contributions from each of the four cylinders, it does not provide a torque comparable to that of the fourth harmonic because each cylinder introduces a lower external moment. This is why an engine with a higher number of cylinders typically exhibits more uniform torque output, resulting in reduced vibration issues.
Therefore, the total external moment that considers both the inertial moment and the motor moment can be rewritten with the exponential formulation as:

$$M_{\text{tot}} = M_i(t) + M_m(t) = \sum_{k=1}^{m\approx 20} M_{i_k} e^{i(k\Omega' t + \Phi_{i_k} + \delta_{j_k})} + \sum_{k=1}^{m\approx 20} M_{m_k} e^{i(k\Omega' t + \Phi_{m_k} + \delta_{j_k})} \tag{3.39}$$

This final expression of the external moment implies that, for each odd harmonic there is only a contribution of the inertia moment while for even harmonics the total moment is from the sum of the two contributions.

Chapter 4

Crankshaft HyperMesh model

While the data necessary for crankshaft analysis using GT-Ise can be estimated using approximated formulas derived from literature, a finite element method (FEM) approach is preferred and also used to assess the accuracy of said semi empirical formulations. This approach involves generating a finite element discretization from a detailed CAD model of the system under analysis. FEM is a powerful computational tool for analyzing such systems and is widely applied across various physical fields due to its ability to accurately model complex geometries. In contrast, the aforementioned formulas are only applicable to simple, standardized geometries and thus cannot yield precise results for dynamic analyses. The FEM approach relies on the discretization of the geometry into a large number of elements with simple shapes.
The geometry composed of individual units is referred to as a mesh, and its accurate definition is crucial in this phase of the study. Once a high-quality mesh has been established, the software applies the Ordinary Differential Equations (ODEs) to all the elements to calculate the desired property [10].
This analysis' main focus are:

- the estimation of lumped parameters (such as inertias and torsional stiffnesses) needed for populating the dynamic model in GT-Ise;

- a detailed representation of the modal analysis, i.e. computation of the natural frequencies and normal modes.

An overview of the CAD model of the crankshaft imported on HyperMesh is reported in figure 4.1.

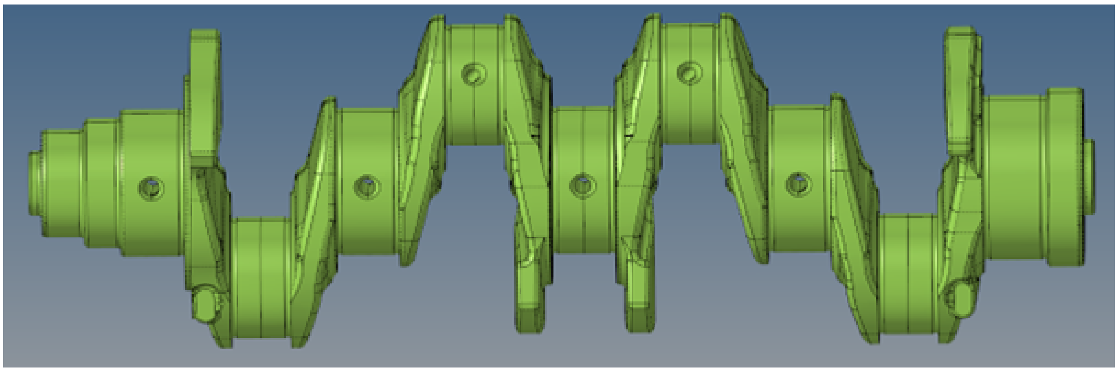

Figure 4.1: Overview of the crankshaft CAD model

4.1 Flywheel inertia

The flywheel inertia is highly affecting the torsional behavior of the crankshaft since it generally represents the 90% of the total inertia of the system. Therefore, it was crucial to add it properly. Figure 4.2 shows an example of flywheel for light duty vehicles.

Figure 4.2: Example of a single mass flywheel [15]

The flywheel inertia is often treated as a lumped parameter in vibration mechanics because of the great value of inertia that introduces.

In conclusion, in HyperMesh a point mass and inertia in the z axis were defined and placed at the interface between crankshaft and inertia as shown in the following figure.

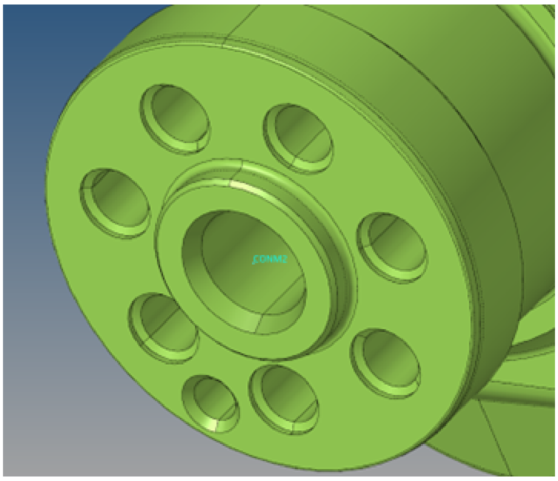

Figure 4.3: Focus on the node where a lumped mass and inertia of the flywheel were added

4.2 Rotating masses

To conduct a precise modal analysis, it is essential to accurately account for the dynamic behavior of rotating components, such as the connecting rod.

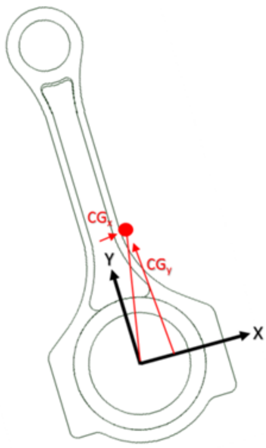

Figure 4.4: Connecting rod COG representation

In the Hypermesh model, this can be achieved by introducing the rotating mass. It is an equivalent lumped mass that provides the same external inertia moment of the crank mechanism of the relative cylinder. It is computed by the formula 4.1 once the COG location is known and it is added to the center of the crankpin as a lumped mass connected with RBE2 rigid elements.

$$m_{\text{rotating}} = \frac{\text{Mass} \cdot (\text{length} - \text{CG})}{\text{Length}} \tag{4.1}$$

The COG location was computed on the CAD model of the connecting rod.

4.3 Rigid connections

The lumped masses and inertias were rigidly linked to the crankshaft using RBE2 elements in Hypermesh. This constrained all six degrees of freedom of the shaft to the lumped masses, ensuring that the added node moved consistently with the corresponding part of the crankshaft.
As shown in the figure 4.5, RBE2 elements link the central node to the crankshaft using multiple elements jointed to their corresponding node on the surface.

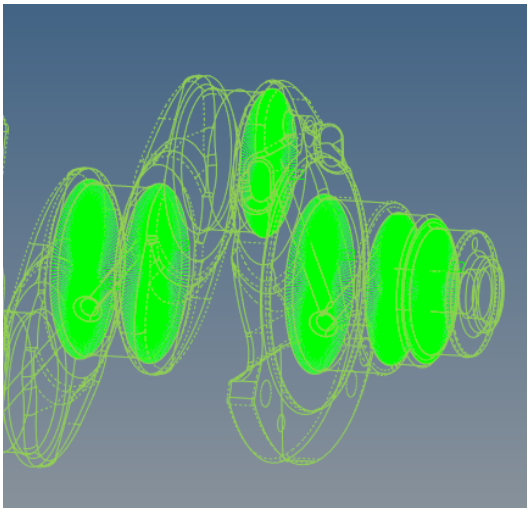

Figure 4.5: Detail on RBE2 elements

RBE2 elements play a crucial role in computing torsional stiffnesses and will be used in subsequent steps of the HyperMesh model.

4.4 Mesh

The most important requirement for the FEM model was represented by a suitable mesh for the purpose that allows to discretize correctly the system and get the results best fitting to real results.
The process was of defining a 2D mesh of the surface and then implementing the 3D one to describe the whole crankshaft. The 2D allowed to edit the mesh with the highest possible flexibility so that all the requirements were fulfilled.
As a first step the whole crankshaft was imported on Hypermesh from a company CAD file. Before defining the mesh, it was necessary to edit the edges that weren't strictly needed for the computation. Indeed, the CAD had many edges that could imply an excessive constraint to the mesh building.
This is because the surface mesh is automatically generated to match all the edges of the model. Furthermore, many edges were constraining small areas that could create errors while generating the 2D mesh due to irregular triangles.
As reported in the following picture, the dotted lines represent the removed edges while the continuous ones the edges kept before starting meshing.

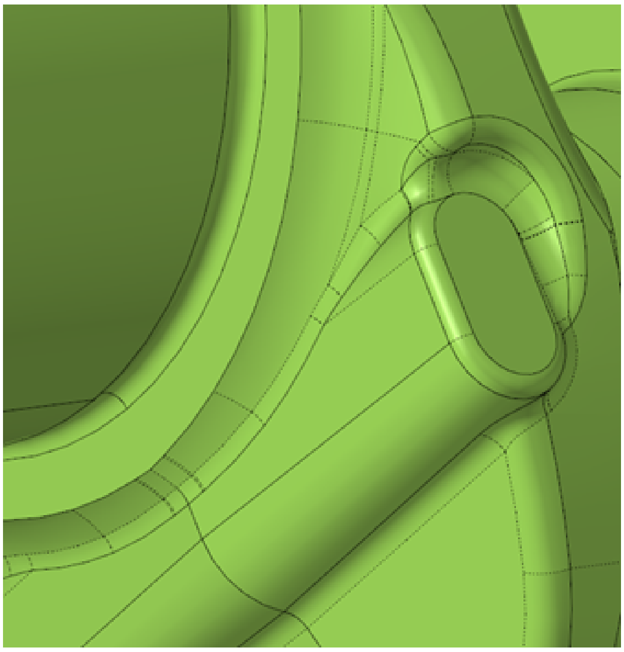

Figure 4.6: Detail on the deleted edges before starting meshing

In the first part, different mesh sizes were defined according to the level of accuracy needed in the parts of the crankshaft. In specific, the highest definition was implemented at the joints of the single components as reported in the following picture.

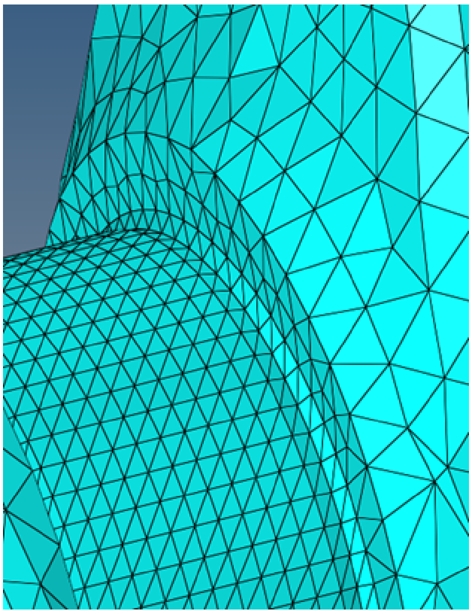

Figure 4.7: Detail on the different mesh sizes used

It can be seen the difference in resolution between the crankpin and the crank web that was chosen as the element with the lowest needed resolution. At the same time, it was necessary to guarantee the compliance of the number of nodes between jointed surfaces as the mesh must be continuous.
A further setting that was the triangle type. As it can be seen, for cylindrical part, rectangular triangles were considered because they have the best fit according to company's experience.
Another important point was meshing the oil holes. Even though at the beginning they were not considered the focus of the meshing procedure, it was necessary to use a higher mesh resolution to get a shape closer to the reality. In the following pictures it is shown how changing the resolution allowed to move from a completely wrong shape to a more suitable one.
The first mesh type (figure 4.8) is not even providing a through hole whilst the

second (figure 4.9) provides almost a cylindrical shape. This was a key requirement for a suitable 3D mesh.

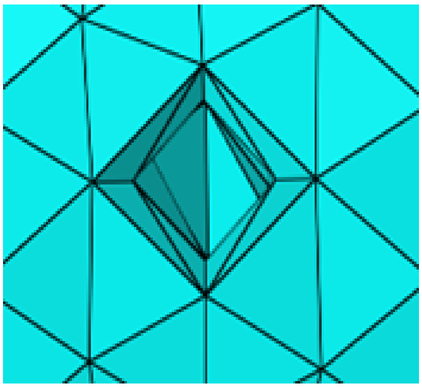

Figure 4.8: Before remeshing

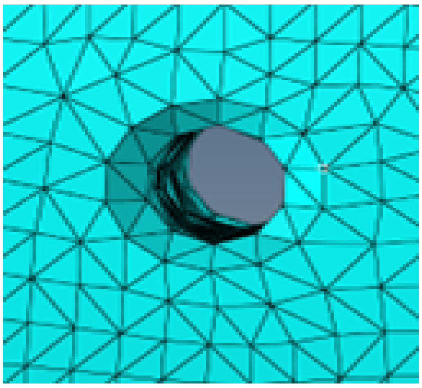

Figure 4.9: After remeshing

It is worth to mention that, increasing the mesh definition, also the journal's mesh definition needed to be increased due to mesh continuity.
Before building the 3D mesh a quality control on the 2D mesh was performed. The focus was correcting certain mesh elements that weren't satisfying the shape requirements. In specific, the smallest angle of each triangle was investigated using the 'quality index' function. The threshold value was set at 5° and every triangle with a smaller angle was manually corrected editing some node's position. It could have been possible to increase even more the mesh quality setting as threshold value 10° for the smallest triangle angle but from the company experience it was discovered that the set one is still sufficient.
The 3D mesh was after created based on tetrahedra elements. They were automatically built by the software provided the surface 2D mesh both form the external and the internal part of the crankshaft just discussed. Before running the simulation, the 2D mesh was again modified because of the incurring of some errors from non-suitable geometries. Therefore, since the 3D mesh only depends on the quality of the 2D one, the number of nodes in certain parts was increased to properly fit the real shape of the component.
The last step to get the final 3D mesh is by moving from first order to second order elements. By doing so, the considered tetrahedra made of 4 nodes move to 10 nodes placed in the mid of each edge. In figure 4.10 the 6 nodes just added are

shown with blue dots.

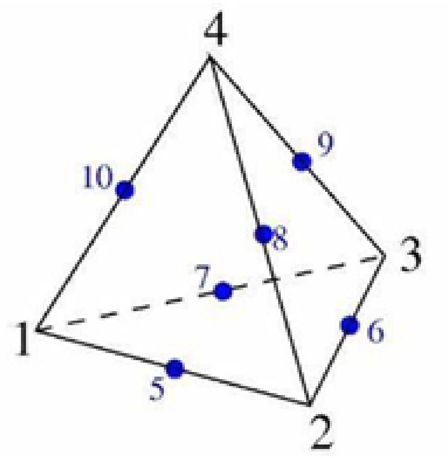

Figure 4.10: Example of a second order tetrahedric element [16]

This is not implying a change of shape of each element because the solid was already fixed but a higher number of nodes allows finer computation with an increasing computational cost.

4.5 Linear static analysis for torsional stiffnesses computation

The first computation to be performed on the FEM model is the evaluation of all the torsional stiffnesses of the shaft. This is a key aim of this model, in fact the correct evaluation of the single stiffnesses is necessary for the computation of torsional natural frequencies, the mode shapes and the frequency response function using the lumped parameter method.

4.5.1 Model for stiffness computation

The torsional stiffness of each component was evaluated starting from the plot of displacements in the x direction when the component is under a certain torsional load.
The torsional stiffness is the ability of the component not to rotate on its axis when subject to an external torsional moment. The model indeed considers the bottom

and top displacements, t and b, to evaluate the position of the center of rotation that might be inside the element's diameter (figure 4.11) or outside (figure 4.12) if this other displacement configuration occurs:

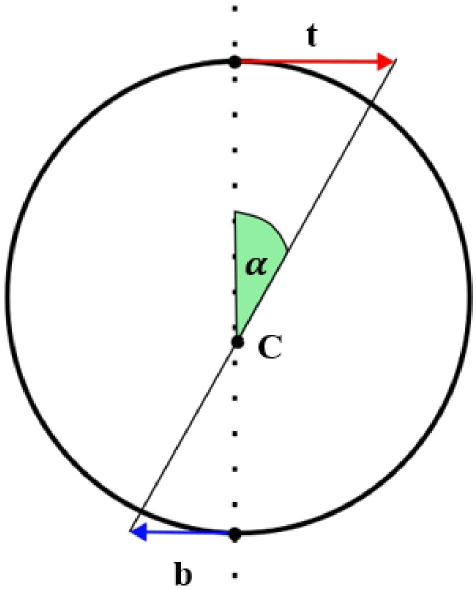

Figure 4.11: First configuration of rotation of the cross section

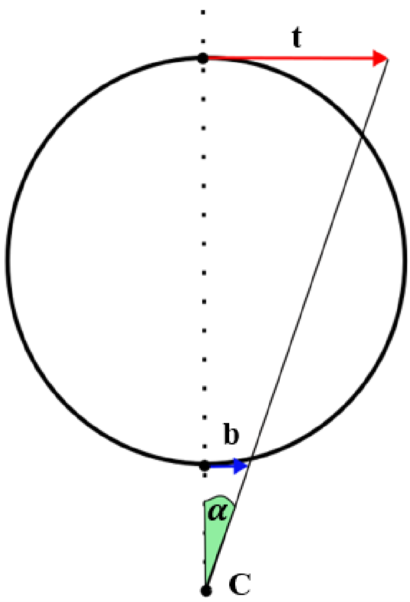

Figure 4.12: Second configuration of rotation of the cross section

The center of rotation is computed considering a line having the two heights at the top and the bottom of the frontal section of the component, respectively at point A and B. The distance AC is computed as follows:

$$l = \overline{CA} = -\frac{t}{\frac{b-t}{d}} \tag{4.2}$$

The rotation angle for the face in analysis can be computed:

$$\alpha = \tan^{-1}\left(\frac{t}{l}\right) \tag{4.3}$$

The difference in the rotation of the two faces at the front and the end of the element in analysis can be computed.

$$\theta = \alpha_r - \alpha_f \tag{4.4}$$

In this way, knowing the applied external moment, it is possible to compute the torsional stiffness even for more than one component in series since only the rotation of the front and rear faces are needed. Therefore, the torsional stiffness is:

$$K_t = \frac{M_t}{\theta} \tag{4.5}$$

The displacements in x direction are computed for two nodes for each surface, opposite with respect to the rotation axis.
It is worth to the discuss the resolution needed in the computations. In fact, to avoid high deformation in the shaft that could have implied wrong evaluations because of a change of shape of the circular section, a low value of external moment was applied. This led to very small deformations that needed to be managed with an high number of decimals to be really accurate.

4.5.2 Loads and constraints

The model is applied by constraining and loading properly the component. The component which stiffness is to be evaluated is constrained at the two sides by means of a 6 DOF constraint and a 5 DOF one, allowing only the rotation around the z axis. These boundary conditions allow to make the element twist rigidly blocking the rotation on one side and allowing the torsional one on the other. As mentioned before, the constraints are applied using a rigid RBE2 connection to link the whole surface to the node on the axis where the check is applied, as reported in figure 4.13.

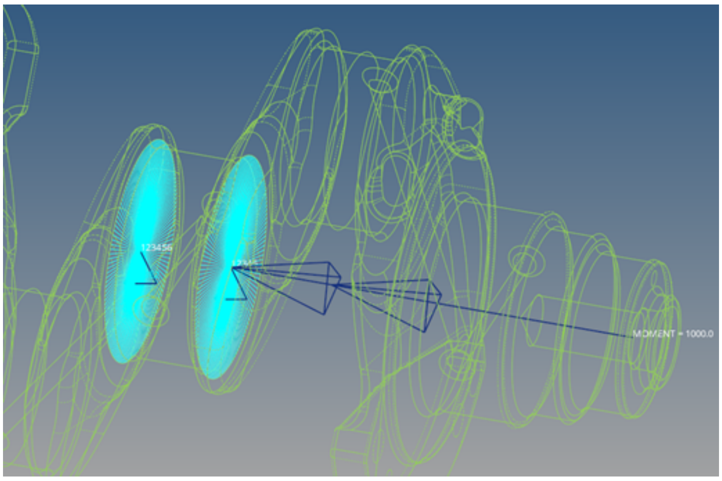

Figure 4.13: Application of the external moment for torsional stiffness computation

4.5.3 Comparison with formulas from literature

The computed results were compared to the ones got with formulas in literature. Starting from the simplest element of the crankshaft, such as the intermediate journal that can be modeled as a cylinder element which geometry is reported in figure 4.14.

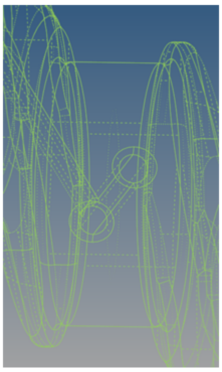

Figure 4.14: Detail on the geometry of an intermediate journal

Assuming a geometry of a full cylinder, the torsional stiffness can be computed as [10]:

$$K = \frac{GI_p}{l} \tag{4.6}$$

where I_p is the polar moment of inertia that in this case is:

$$I_p = \frac{\pi d^4}{32} \tag{4.7}$$

In this simple case, the results got from the HyperMesh model, are lower than the ones from the formula just introduced. This is reasonably due to the presence of the oil passages that imply void volumes (as reported in the picture) that of course bring to the decrease of stiffness of the component.
Another comparison was performed between the Tuplin's formula, a semi empirical formulation valid for fast large diesel engines to compute an equivalent length of a beam with the same cross section of principal axis of the crankshaft. l_eq allows the computation of the torsional stiffness of the whole crankshaft bank. The detail on Tuplin's formula is reported in figure 4.15 and equation 4.8.

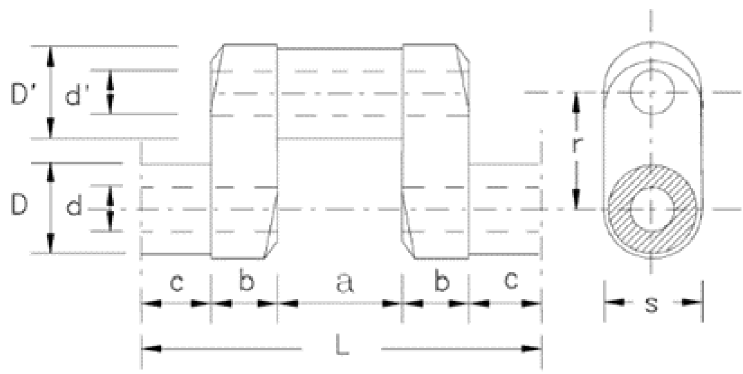

Figure 4.15: Description of the parameters used in Tuplin's formula [10]

$$\begin{aligned} l_{eq} = {} & \frac{2c + 0.15D}{1 - \left(\frac{d}{D}\right)^4} + (a + 0.15D)\frac{D^4 - d^4}{1 - \left(\frac{d'}{D'}\right)^4}(D'^4 - d'^4) + \\ & + [2b - 0.15(D + D')]\left(\frac{D^4 - d^4}{s^4 - d^4}\right) + r\left(0.065\frac{D}{b} + 0.58\right)\frac{D^4 - d^4}{bs^3} + 0.016\frac{D^4 - d^4}{b^2 s} \end{aligned} \tag{4.8}$$

The equivalent stiffness is found computing a polar moment of inertia of a hollow cylinder but for the crankshaft in analysis d=0 and d'=0 since the journals and crankpins are represented as full cylinders as shown in equations 4.9 and 4.10.

$$I_p = \frac{\pi(D^4 - d^4)}{32} \tag{4.9}$$

$$k_{eq} = \frac{GI_p}{l_{eq}} \tag{4.10}$$

This model provides not very accurate results with respect to the ones computed on with the HyperMesh model. In this case, the comparison was performed with respect to the sum of all the stiffnesses of the bank in analysis in series as:

$$\frac{1}{k_{eq}} = \frac{2}{k_{Journal}} + \frac{2}{k_{crankweb}} + \frac{1}{k_{crankpin}} \tag{4.11}$$

Considering the stiffness computed with FE as a referring one, this model introduced an overestimation of the stiffness of around 40%, so it can be concluded that is just able to make a first estimation of the bank stiffness. In this case the geometry is the driving factor since the model assumes the crank webs as parallelepipeds thus introducing strong simplification of the geometry.
Furthermore, also in this case, the formulation is not considering the internal geometry of the elements composing the bank such as the oil passages. Furthermore, starting from the Tuplin's formula, it was interesting to discuss the ability of this formulation to estimate the crank web stiffness that is generally difficult to compute. For this evaluation, the parameters a and c were put to 0 so that the equivalent length was only related to the two crank webs of the bank.
The results shown even poorer accuracy than to the estimation of the full bank with an underestimation of over 200%. This could be easily justified because this is a semi-empirical formula that is based on experimental evidence, derived for the full bank where the crank webs represent the less stiff element of the system.

4.6 Modal Analysis

Modal analysis is a valuable evaluation technique for vibrating systems. It employs a modal approach, where the vibration of a body is decomposed into an infinite sum of contributions from specific vibration shapes, known as modes, with varying weights. Each mode is characterized by a natural frequency, which induces vibration resonance, and a shape.
The mode shape is a crucial parameter for understanding the dynamics of the system. For complex systems comprising multiple masses, computing even a few of the most significant modes can provide insight into the system's behavior during vibration.
The modes of a system are strongly influenced by its mass distribution, shape, and constraints connecting it to the ground [9].
In this study, modal analysis was performed for two purposes: to verify the first two torsional modes computed by the GT-Ise model and to determine whether the mode shapes conformed to those typical of crankshafts.

4.6.1 Constraints

In the Hypermesh model some constraints were to be set to perform the modal analysis. In this study, since only the torsional modes were investigated, it was necessary to fix all the other degrees of freedom along the shaft.
This approach was applied after some preliminary simulations. In fact, starting the modal analysis without constraining the bending modes, the software provided non-pure torsional modes thus leading to incorrect results for a pure torsional modal analysis.
Furthermore, the FEM modal analysis was performed as a reference for the simulations to be performed on GT-Ise that performs a pure torsional analysis. For this reason, it wouldn't be correct to compare the full modal analysis to the one computed in the other simulation environment.
For what concerns the constraints' placements, they were applied in correspondence of the bearings' positions on the shaft thus representing the real working conditions, as shown in figure 4.16.

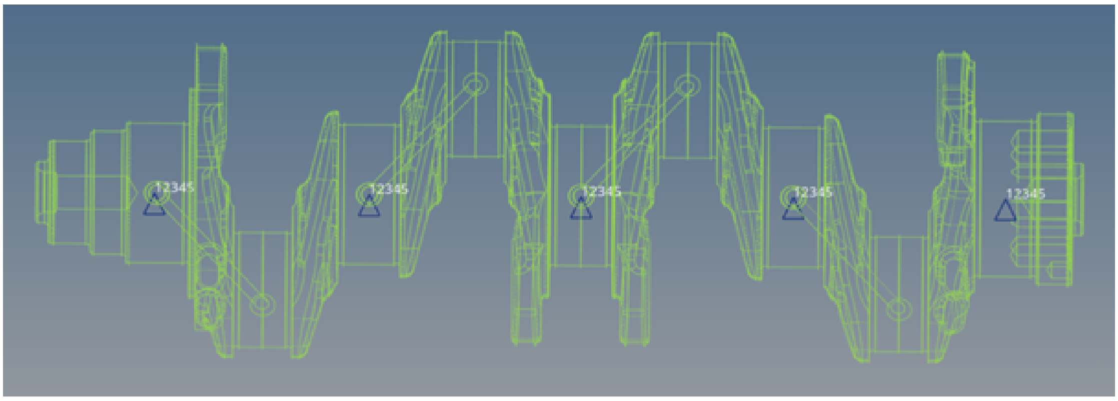

Figure 4.16: Detail on the constraints' placement for modal analysis

4.6.2 Results

The investigation of mode shapes focused on the first two modes, as they are the most significant from a design perspective. In fact, they are responsible for the most critical resonances that occur in the shaft, so both must be monitored during analysis. The first torsional mode occurs at a frequency of 441 Hz with the following mode shape (figure 4.17), where red tones indicate higher displacement while blue tones indicate areas with minimal movement.

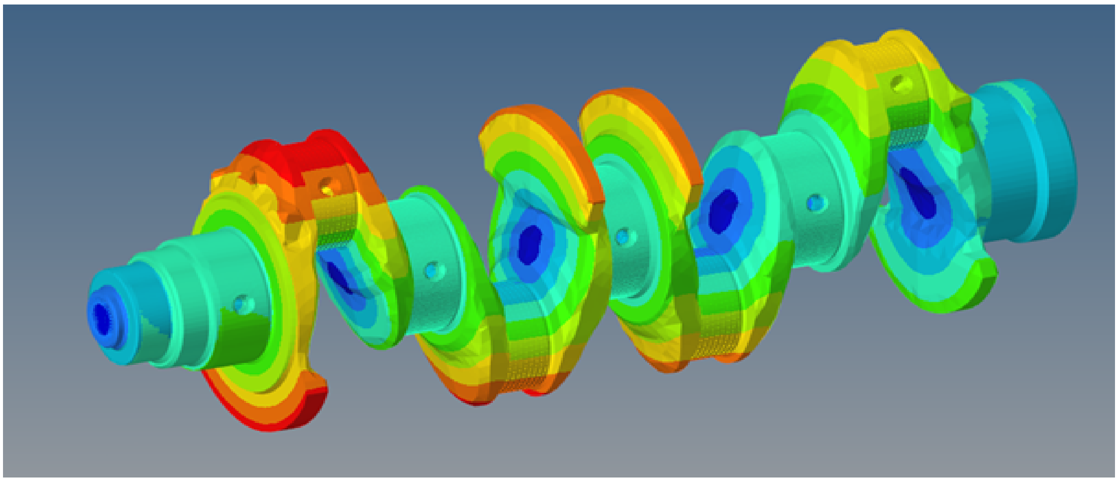

Figure 4.17: First torsional mode at 441 Hz

The second torsional vibration mode occurs at 1174 Hz and it is reported in figure 4.18.

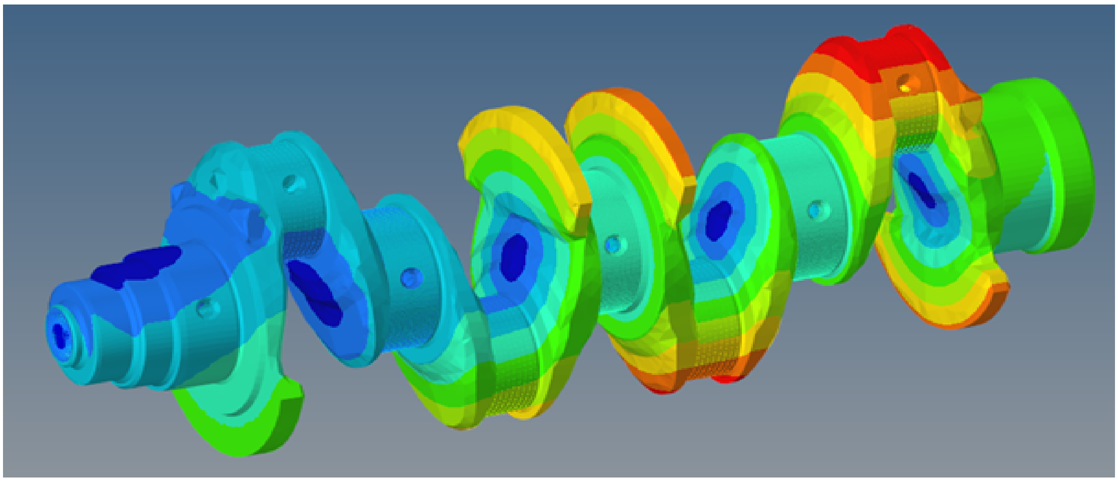

Figure 4.18: Second torsional mode at 1174 Hz

As shown in the plot, the second mode is characterized by the presence of a structural node, which is a point where displacement is null. When dealing with mode shapes, all constraints on the modes are structural nodes. However, starting from the second mode, additional nodes appear in a number equal to the mode minus one. This is clearly illustrated in figure 4.19, which shows the first four bending modes of a shaft fixed at both ends.

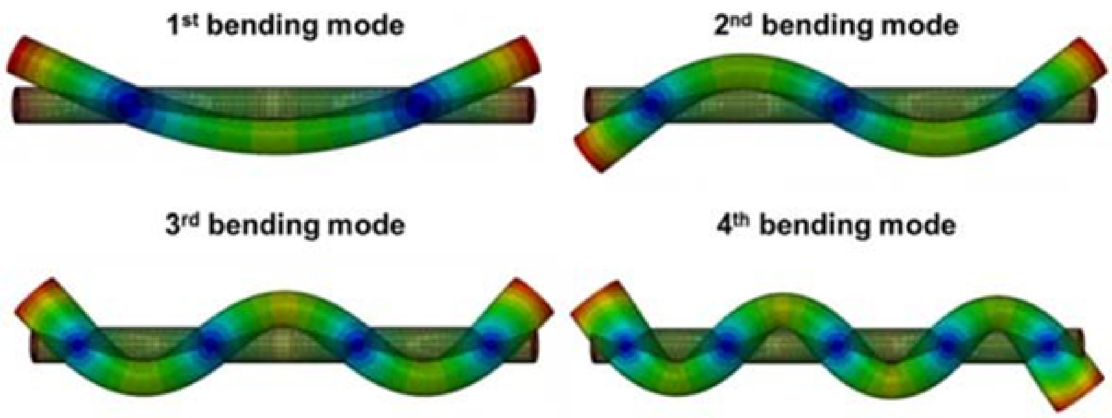

Figure 4.19: Example of first four bending modes of a fixed-fixed shaft

Chapter 5

Input data for lumped parameters model

The two models for the crank mechanism system that will be shown in the following chapters are based on lumped parameters. The most important parameters for a torsional analysis are the inertias and the torsional stiffnesses. However, GT-Ise requires futher data that will be shown in the relative chapter.
To have a comparison between the performance of an expensive software and a MATLAB code, it was necessary to provide the same inputs to both the simulation environments.

5.1 Inertias

The inertias of all components of the shaft were automatically calculated by the software using their CAD drawings. No computation was required for this section as each part had an interface similar to the one shown in figure 5.1. Between all these informations, only the mass and inertia with respect to the axis of rotation were considered. This choice is in accordance with a only torsional analysis of a lumped parameters system.

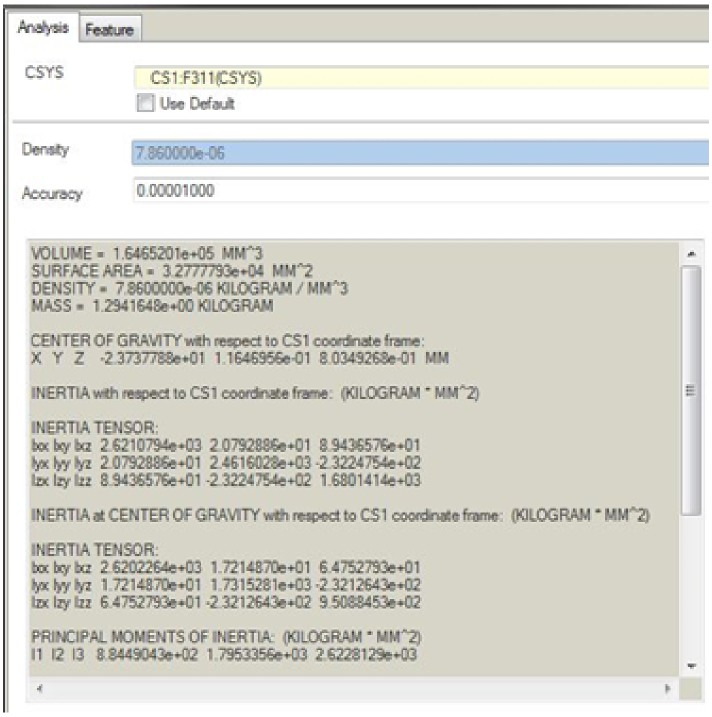

Figure 5.1: Interface of inertia properties

As previously stated, some components of the crankshaft were repeated (e.g., the intermediate journals), while others exhibited variations, such as the crank webs, which also had a counterweight configuration. Naturally, different components corresponded to different inertia values, necessitating an investigation of each component type.

5.2 Torsional stiffnesses

The torsional stiffenesses computed in the Hypermesh model were added as lumped parameters. These values are the most reliable lumped parameter because they are based on a FEM analysis even if a full 3D CAD model would be even more detailed.

5.3 Pressure cycle and motor moment modelling

Given that the ultimate objective of this phase of the project is to simulate the forced frequency response of the crankshaft during bench testing, it is imperative to accurately define the pressure cycle as a critical parameter for the proper representation of the loading conditions encountered during bench testing. The bench testing is performed at 100% load for each engine speed so, the full run of the accelerator, without any power partialization.
The following picture (figure 5.2) shows the pressure cycle used as reference while performing the bench testing as a function of the crank angle and engine speed.

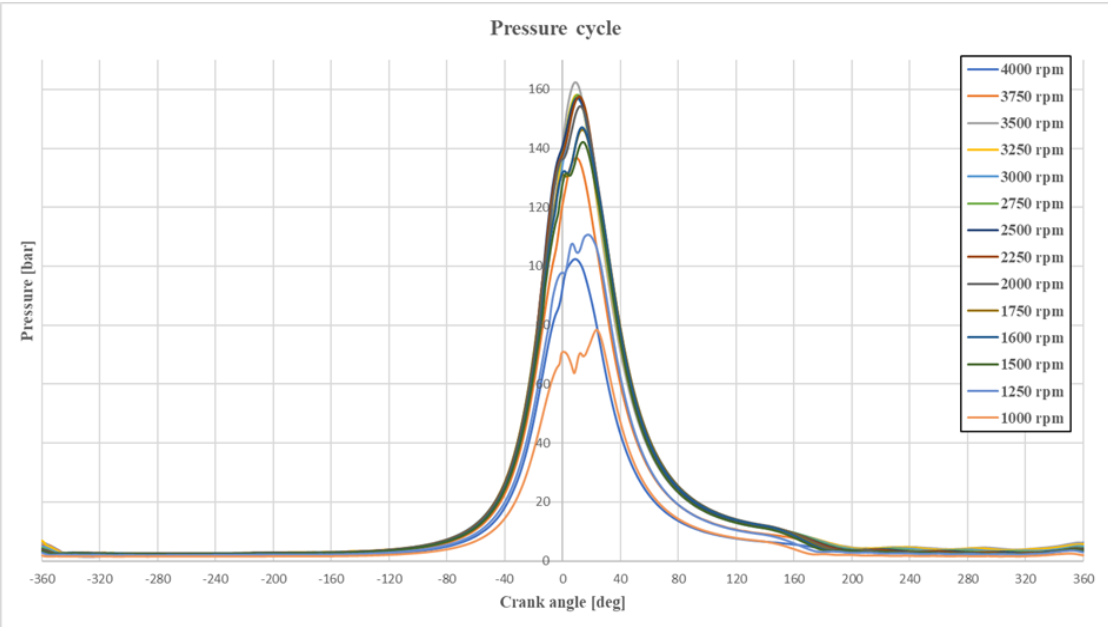

Figure 5.2: Graphical representation of the pressure cycle

As the pressure in the cylinder depends on two independent variables, a 2D look up table must be introduced, both in GT-Ise and MATLAB, to make the software choose the right working condition during the forced frequency analysis.

Z Data	Y Data #	1	2	3	4	5	6	7
X Data ⇒		1000.0	1250.0	1500.0	1600.0	1750.0	2000.0	2250.0
1	-360.0	1.838	2.8	3.29	3.32	3.38	3.55	3.7
2	-359.0	1.717	2.63	3.15	3.21	3.24	3.44	3.6
3	-358.0	1.619	2.44	2.97	3.03	3.08	3.29	3.46
4	-357.0	1.54	2.29	2.78	2.88	2.94	3.14	3.3
5	-356.0	1.505	2.16	2.63	2.74	2.81	2.99	3.19
6	-355.0	1.505	2.06	2.53	2.62	2.67	2.85	3.09
7	-354.0	1.515	2.01	2.46	2.55	2.58	2.73	2.96
8	-353.0	1.536	2.01	2.41	2.51	2.53	2.64	2.82
9	-352.0	1.549	2.03	2.42	2.51	2.49	2.57	2.68
10	-351.0	1.565	2.06	2.44	2.52	2.48	2.54	2.57
11	-350.0	1.566	2.09	2.46	2.53	2.48	2.53	2.5
12	-349.0	1.557	2.12	2.48	2.55	2.49	2.52	2.5
13	-348.0	1.546	2.13	2.51	2.59	2.5	2.53	2.51
14	-347.0	1.537	2.14	2.53	2.62	2.51	2.54	2.55
15	-346.0	1.532	2.13	2.55	2.65	2.54	2.57	2.57
16	-345.0	1.527	2.13	2.56	2.68	2.58	2.59	2.56
17	-344.0	1.517	2.13	2.56	2.69	2.61	2.61	2.58
18	-343.0	1.515	2.12	2.55	2.7	2.62	2.65	2.58
19	-342.0	1.515	2.1	2.56	2.71	2.65	2.68	2.6
20	-341.0	1.517	2.1	2.56	2.72	2.67	2.69	2.62
21	-340.0	1.517	2.08	2.56	2.72	2.68	2.7	2.67
22	-339.0	1.518	2.07	2.56	2.72	2.68	2.71	2.73
23	-338.0	1.511	2.08	2.54	2.72	2.68	2.71	2.76
24	-337.0	1.517	2.08	2.52	2.7	2.67	2.72	2.77
25	-336.0	1.52	2.07	2.52	2.69	2.67	2.71	2.76
26	-335.0	1.531	2.07	2.52	2.69	2.68	2.71	2.74
27	-334.0	1.543	2.05	2.52	2.68	2.68	2.73	2.75
28	-333.0	1.537	2.04	2.51	2.67	2.68	2.73	2.75

Figure 5.3: 2D look-up table for pressure cycle definition

This table facilitates the automatic computation of pressure via linear interpolation across the entire frequency spectrum under examination, ranging from 1000 to 4000 rpm. Consequently, the software is capable of calculating the engine moment, which, as previously mentioned in the theoretical section, is directly proportional to the pressure.

An analysis of the pressure values reveals that the maximum pressure of 162 bar is attained at 3500 rpm, indicating that the highest external moment will occur within this speed range. Additionally, since the pressure cycle is specified for each cylinder and the firing order is determined in the crankshaft definition, the phases of each thermodynamic cycle are automatically computed.

All these data are essential for the complete definition of the Fourier transform of the total external moment $M_{tot}(t)$.

5.4 Material properties and internal damping

Another input requirement pertains to the material properties.

The F1A crankshaft is composed of heat-treated spheroidal cast iron. Given that the physical properties of this material are strongly dependent on its composition, it was necessary to define the material in the software using specifications provided by the company [17].

Specifically, the following parameters were to be set for a proper material definition:

- Density ρ: it is needed even if punctual mass values were defined because further computation may be automatically performed to increase the accuracy of the simulation;
- Young Modulus E: directly proportional to the shear modulus G by the Poisson's ratio. The G parameter is required to compute the torsional stiffness;
- Poisson's ratio ν;
- Damping ratio ζ that is now discussed in more in depth.

Internal damping is determined by the material's damping ratio (ζ), a dimensionless measure that describes how oscillations decay following the application of a disturbance to the system. The most robust method for computing this ratio involves evaluating the logarithmic decrement of the material's response peaks once an external excitation has been applied. The logarithmic decrement is defined as follows, where u is the amplitude of the *i-th* peak [9].

$$\zeta = \ln\left(\frac{u_{t_i}}{u_{t_{i+1}}}\right) \tag{5.1}$$

According to this value, the system can be defined as:

- *underdamped*, ζ<1;
- *critically damped*, ζ=1;
- *overdamped*, ζ>1;

Even though from the theoretical point of view, a null value of ζ would imply an undamped system, it is not possible to have no internal damping in real applications. Each of these mentioned systems has a different dynamic response in time. Figure 5.4 summarizes all the four possible responses.

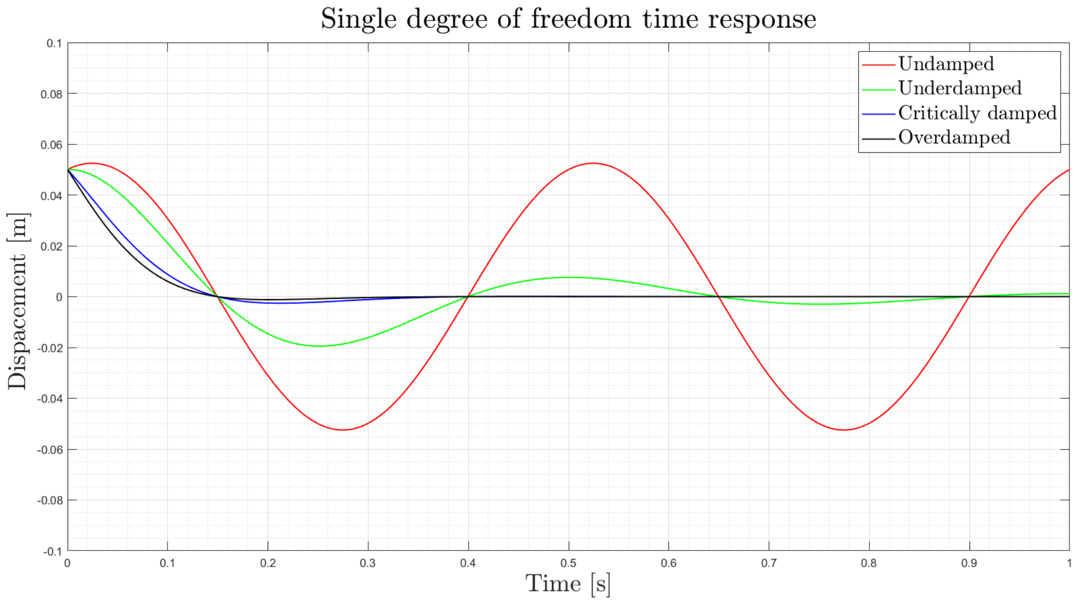

Figure 5.4: SDOF time response with different damping conditions

From the company's experience the ζ was set to 2% that is a value compliant with the scientific knowledge [17].
Although damping in simple dynamic systems arises solely from the material, it is not realistic to account only for the material's damping contribution when dealing with a crankshaft system. The largest contribution to damping comes from lubricated parts (viscous damping) that dissipate energy during the rotational movement of the shaft [10].
Specifically, the links of the connecting rod to the piston and pin play an important role, as does the friction force acting on the piston itself during its vertical motion. The schematic in figure 5.5 provides a front view of the crankshaft, highlighting these contributions.

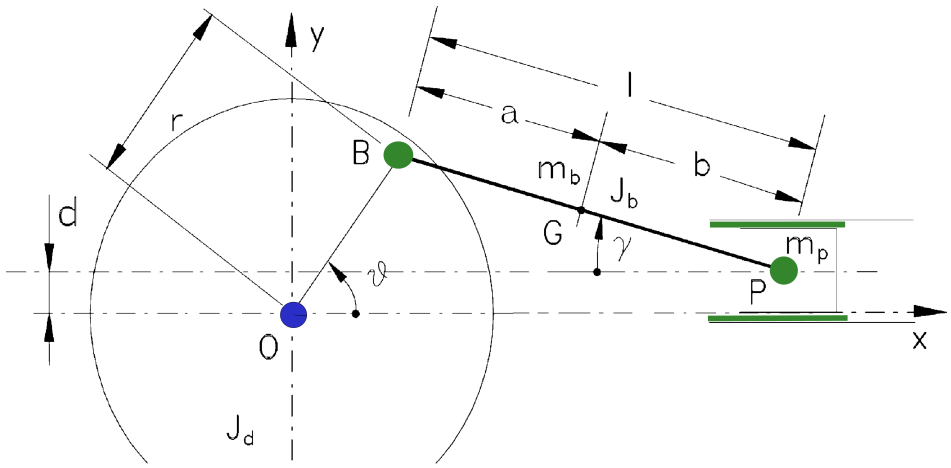

Figure 5.5: Crank mechanism internal damping contributions [10]

From a theoretical perspective, these additional damping contributions can be accounted for by means of an external moment, with the damping coefficient C identified through experimental tests.
In GT-Ise, a ζ value can be defined for each component to account for these further contributions. Since this provides a much stronger damping effect than that of the material and is not linked to the material (as it is a viscous damping), it was set to 30% according to the company's experience.
Differently, in the MATLAB model, since a precise value of the damping was needed to be put inside the C matrix, two contributions were considered as well. However, it wasn't possibile to convert the ζ values of the GT-Ise model because of the complexity of the system ad a tuning based on the bench testing results was performed to better define the damping contribution.

Chapter 6

MATLAB model for crank mechanism

Even if GT-Ise will be used to assess the targets by linking the FEAD model to the crankshaft one, a MATLAB model was implemented to apply the equations presented in chapter 3 to the equations of motion of a crank mechanism system. The following procedure is the most diffused approach from literature that enables to convert a periodic torsional equation of motion to an harmonic one, allowing to solve it in closed form as done for simple systems subject to harmonic excitations. Despite being a good fitting model, this alternative doesn't represent the most accurate way to solve such systems. The best approach would be a multi-body simulation on a FEM software that would enable to consider both the axial, flexural and torsional dynamics of the crankshaft.
However, considering that the torsional behavior is dominant in such system it still brings a quite accurate evaluation.

6.1 Lumped parameters setting

This analysis of torsional vibrations involves the construction of an equivalent lumped parameter torsional system, comprising a number of flywheels equal to the number of crank mechanisms, interconnected by straight shafts, figure 3.1. Considering the shaft in analysis, with the TVD applied to the front-end side

the equivalent model can be represented as shown in figure 6.1, where the blocks represent inertias and springs and dashpots stay for torsional stiffnesses and torsional damping.
The model shows 9 DOFs where four of them represent the cylinders banks, two are used to describe the TVD and other two are used to represent the flywheel and the front-end hub. The flywheel flange was treated as a lumped inertia linked to the flywheel with a stiffness equal to the one provided by the flange itself.

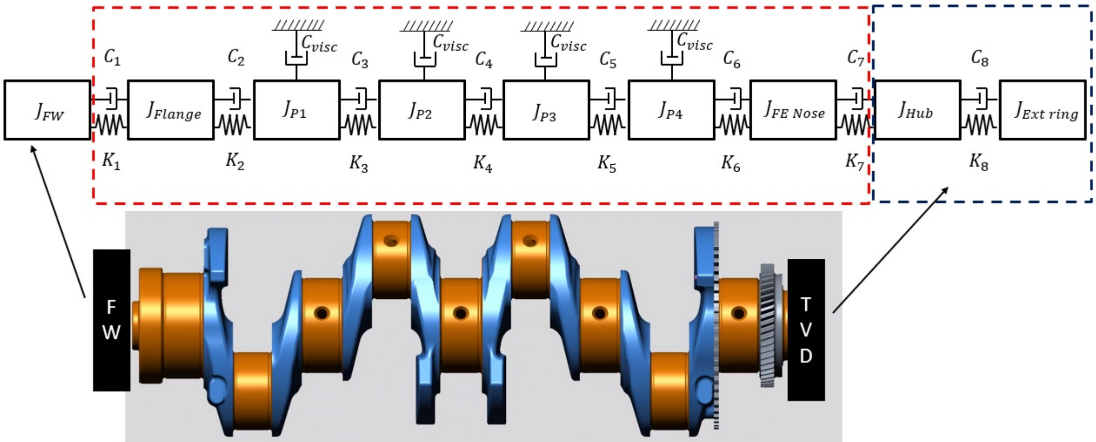

Figure 6.1: Lumped parameters representation of crankshaft

The inertia contributions were accounted in two different ways. The elements outside the cylinder banks were considered as lumped parameters from the beginning. For what concerns the inertia from the cylinder banks the equivalent inertia was computed following the procedure shown in chapter 3. Therefore, for each of bank a J_{eq} function was computed and its Fourier series was considered. This step was accomplished using the 'fft' function in MATLAB that provides the spectrum of the signal thus displaying the amplitude and the phase of each order that constitutes the signal. The J_{eq} signal spectrum from cylinder 1 is reported in figure 6.2.

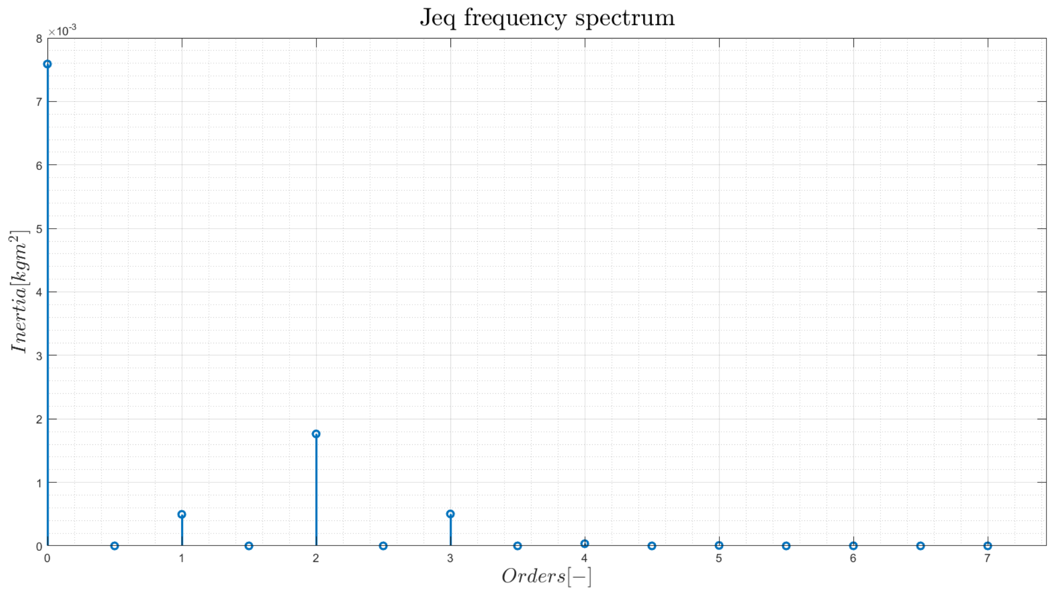

Figure 6.2: J_{eq} signal spectrum

The equivalent inertia for this approach is represented by the order 0 term while the other contributions are accounted in the inertial moment considered as an excitation, as already shown in equation 3.22.
Starting from the 'fft' output complex vector, the signal can be rebuilt applying the summation in equation 6.1:

$$\text{signal} = A_0 + \sum A\cos(i\theta + \phi) \tag{6.1}$$

Where A_0 is the mean value (for $J_eq(\theta)$ is $\overline{J_{eq}}$), A is the absolute value of the i-th component of the vector, ϕ is its phase and i is the number of the order considered. This passage is important because it allows to understand that, even with a lower number of harmonics it is possible to build almost the same starting signal but using fewer data. An example of a rebuilt $J_eq(\theta)$ signal is shown in figure 6.3, where only the first 10 harmonics were considered.

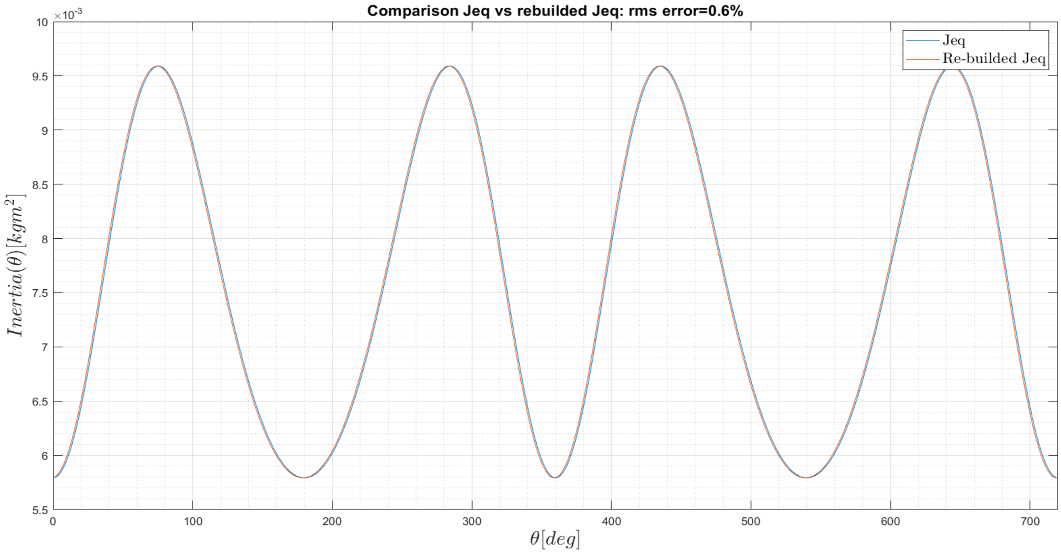

Figure 6.3: Comparison between J_{eq} and re-builded J_{eq}

The result show that even a lower number of harmonics could be sufficient to represent such signal since the 'rms' of the error is just 0.6%. The 'rms' in a powerful tool to evaluate the error with respect to a reference signal based on the energy of the two signals. It represents fine estimation of the error alongside all the signal.
For what concerns the torsional stiffnesses, starting from the values computed in chapter 4, it was necessary to make a series summation of the ones regarding the cylider banks as reported in equation 6.2.

$$k_{\text{eq}} = \left(\frac{1}{k_{\text{journal}}} + \frac{1}{k_{\text{crankweb}}} + \frac{1}{k_{\text{crank pin}}} + \frac{1}{k_{\text{crankweb}}} \right)^{-1} \tag{6.2}$$

In this way, a stiffness equivalent to the whole cylinder bank stiffness is computed. For the components outside of the cylinder banks, the stiffness computed in chapter 4 was used.
Talking of damping contributions, a coupling damping contribution due to the material was considered along all the crankshaft. Furthermore, a localized damping at the cylinder banks was introduced to account for the viscous contributions (C_{visc}) shown in figure 5.5.

These data were provided as input to the MATLAB model by means of the mass, damping and stiffness matrices reported hereafter.

$$M = \begin{bmatrix} J_{FW} & 0 & 0 & 0 & 0 & 0 & 0 & 0 & 0 \\ 0 & J_{Flange} & 0 & 0 & 0 & 0 & 0 & 0 & 0 \\ 0 & 0 & J_{P1} & 0 & 0 & 0 & 0 & 0 & 0 \\ 0 & 0 & 0 & J_{P2} & 0 & 0 & 0 & 0 & 0 \\ 0 & 0 & 0 & 0 & J_{P3} & 0 & 0 & 0 & 0 \\ 0 & 0 & 0 & 0 & 0 & J_{P4} & 0 & 0 & 0 \\ 0 & 0 & 0 & 0 & 0 & 0 & J_{FENose} & 0 & 0 \\ 0 & 0 & 0 & 0 & 0 & 0 & 0 & J_{Hub} & 0 \\ 0 & 0 & 0 & 0 & 0 & 0 & 0 & 0 & J_{Extring} \end{bmatrix}$$

$$C = \begin{bmatrix} C_1 & -C_1 & 0 & 0 & 0 & 0 & 0 & 0 & 0 \\ -C_1 & C_1+C_2 & -C_2 & 0 & 0 & 0 & 0 & 0 & 0 \\ 0 & -C_2 & C_2+C_3+C_{visc} & -C_3 & 0 & 0 & 0 & 0 & 0 \\ 0 & 0 & -C_3 & C_3+C_4+C_{visc} & -C_4 & 0 & 0 & 0 & 0 \\ 0 & 0 & 0 & -C_4 & C_4+C_5+C_{visc} & -C_5 & 0 & 0 & 0 \\ 0 & 0 & 0 & 0 & -C_5 & C_5+C_6+C_{visc} & -C_6 & 0 & 0 \\ 0 & 0 & 0 & 0 & 0 & -C_6 & C_6+C_7 & -C_7 & 0 \\ 0 & 0 & 0 & 0 & 0 & 0 & -C_7 & C_7+C_8 & -C_8 \\ 0 & 0 & 0 & 0 & 0 & 0 & 0 & -C_8 & C_8 \end{bmatrix}$$

$$\mathrm{K} = \begin{bmatrix} K_1 & -K_1 & 0 & 0 & 0 & 0 & 0 & 0 & 0 \\ -K_1 & K_1+K_2 & -K_2 & 0 & 0 & 0 & 0 & 0 & 0 \\ 0 & -K_2 & K_2+K_3 & -K_3 & 0 & 0 & 0 & 0 & 0 \\ 0 & 0 & -K_3 & K_3+K_4 & -K_4 & 0 & 0 & 0 & 0 \\ 0 & 0 & 0 & -K_4 & K_4+K_5 & -K_5 & 0 & 0 & 0 \\ 0 & 0 & 0 & 0 & -K_5 & K_5+K_6 & -K_6 & 0 & 0 \\ 0 & 0 & 0 & 0 & 0 & -K_6 & K_6+K_7 & -K_7 & 0 \\ 0 & 0 & 0 & 0 & 0 & 0 & -K_7 & K_7+K_8 & -K_8 \\ 0 & 0 & 0 & 0 & 0 & 0 & 0 & -K_8 & K_8 \end{bmatrix}$$

6.2 Natural frequencies and mode shapes

The model is still missing the forcing function coming from the engine but it is ready to compute the natural frequencies and mode shapes of the undamped crank mechanism system.
For the sake of comparing results from different simulations, the same model just shown was repeated and applied to the crankshaft without TVD such that the natural frequencies and the mode shapes computed in MATLAB could be compared with the ones from GT-Ise and HyperMesh.
Once again, the HyperMesh model is the referring one where the multi-body analysis was performed. The natural frequencies from the three computations are compared in the following table.

Natural frequencies from No - TVD models			
Mode [Hz]	HyperMesh	GT-Ise	MATLAB
1	0	0	0
2	441	470	416
3	1174	1284	1071
4	2217	2025	1533
5	3562	2571	2005

As reported in the table, considering the HyperMesh model as referring one, both GT-Ise and MATLAB show a little deviation from the correct natural frequencies values. This result highlights the different accuracy between the real model and lumped parameters models. An even higher difference is found moving towards higher frequencies due to the presence of coupling between the axial, flexural and torsional modes in the HyperMesh simulation.
Figure 6.4 shows the nine torsional mode shapes computed by the MATLAB model.

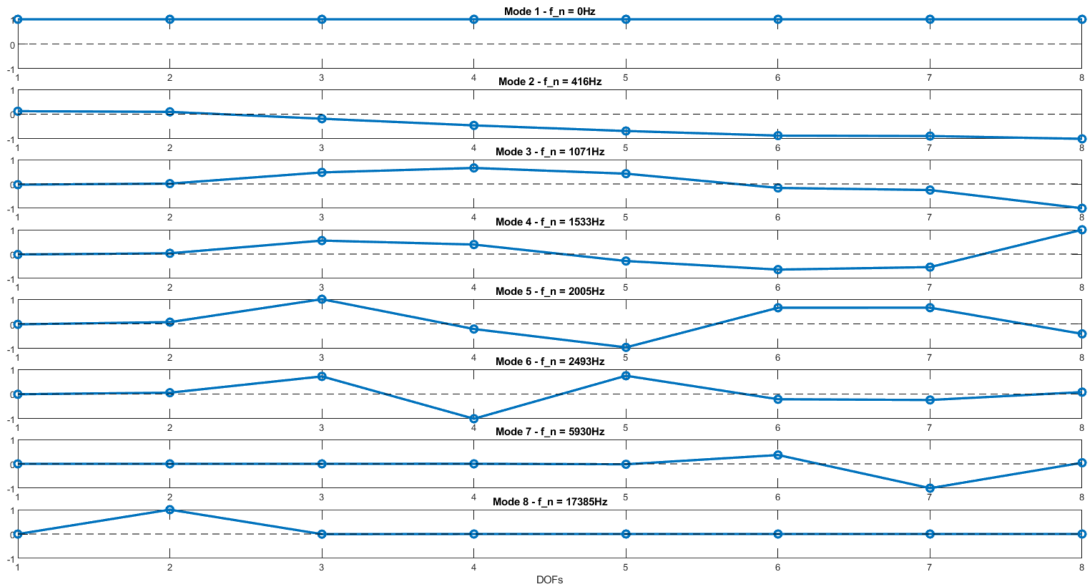

Figure 6.4: Mode shapes from MATLAB model without TVD

Another interesting point can be looking at the natural frequencies when the TVD is added. Therefore, in the following table the natural frequencies computed in MATLAB are compared to the ones from GT-Ise showing good alignment.

Natural frequencies from TVD models		
Mode [Hz]	GT-Ise	MATLAB
1	0	0
2	247	217
3	483	445
4	1256	1087
5	1701	1544

It is also possible to plot the mode shapes form the MATLAB model when the TVD is added.

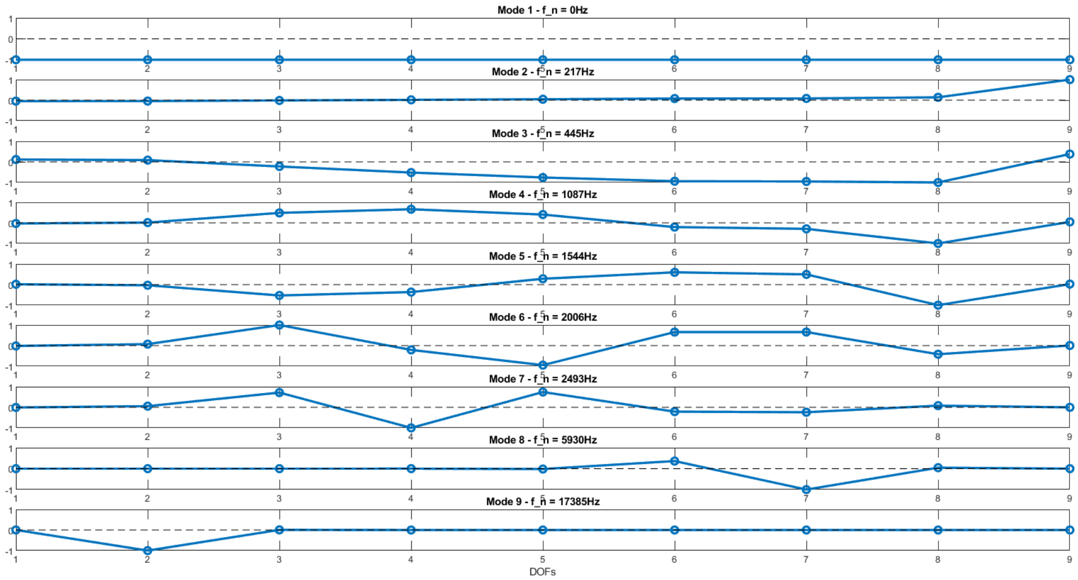

Figure 6.5: Mode shapes from MATLAB model with TVD

It is very interesting to notice in mode 2 the ninth degree of freedom is absorbing the mechanical energy keeping the crankshaft almost rigid by rotating with high amplitude. This behaviour is peculiar of the TVD just added.
As anticipated, the addition of TVD implies a lower first natural frequency but a better performance in terms of amplitudes. For this reason a comparison between the crankshaft Campbell diagram before and after the TVD addition can be reported, as shown in figures 6.6 and 6.7.

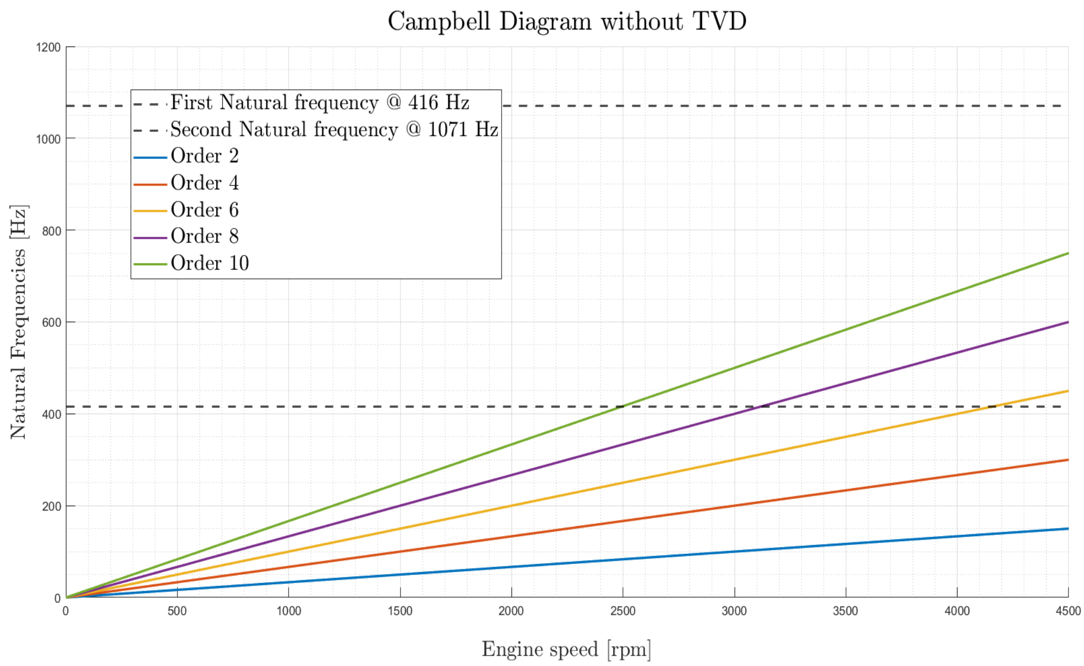

Figure 6.6: Campbell diagram without TVD

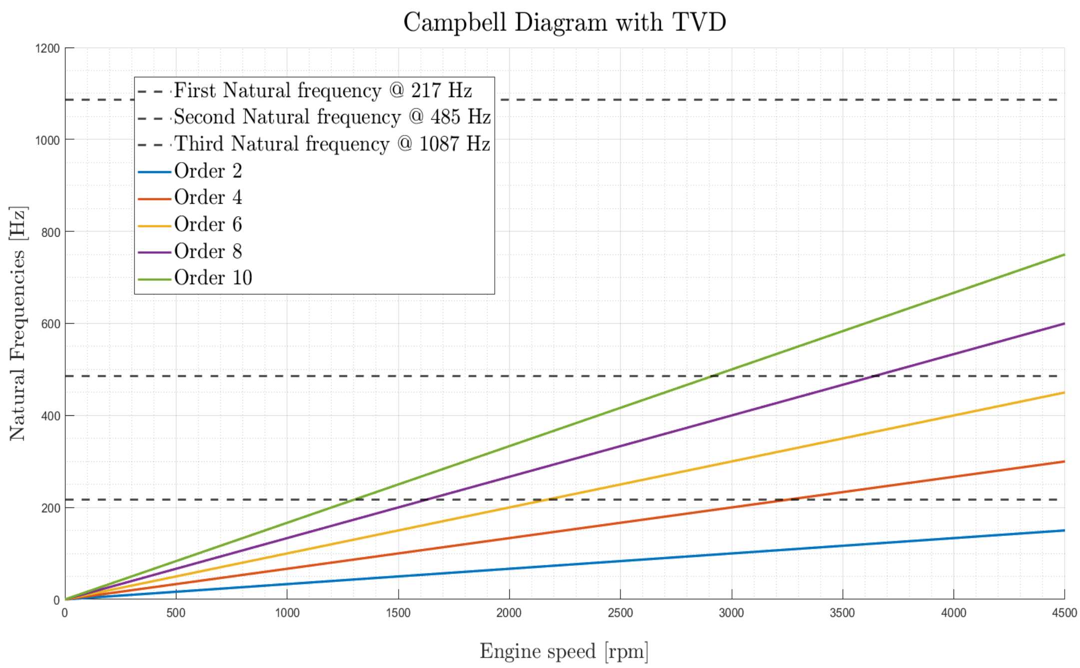

Figure 6.7: Campbell diagram with TVD

6.3 Generalized forces

The free vibrations model, can be now enriched with the addition of the external moments. As anticipated in equation 3.39, the right side of the EOM is to be filled with the summation of the inertial moment due to the non constant inertia of the crank mechanism and the gas moment.
Both the contributions are computed as shown in chapter 3 for each cylinder and applied to their relative DOF, therefore the external moment vector would be:

$$M_e = \begin{bmatrix} 0 \\ 0 \\ M_{i1} + M_{m1} \\ M_{i2} + M_{m2} \\ M_{i3} + M_{m3} \\ M_{i4} + M_{m4} \\ 0 \\ 0 \\ 0 \end{bmatrix}$$

The M_e vector is made of complex terms that are from the summation of the contribution of the first eight orders of vibration. These contributions were computed using the 'fft' function in MATLAB leading to the following frequency spectrum for inertial and gas moment of one cylinder @ 1000 rpm, considered as an example.

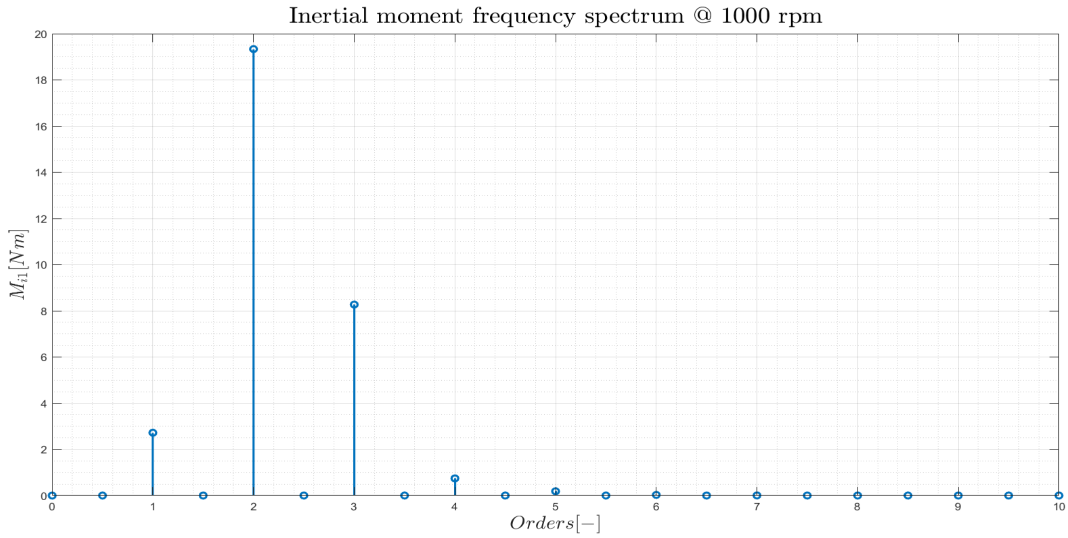

Figure 6.8: Singe cylinder inertial moment frequency spectrum @ 1000 rpm

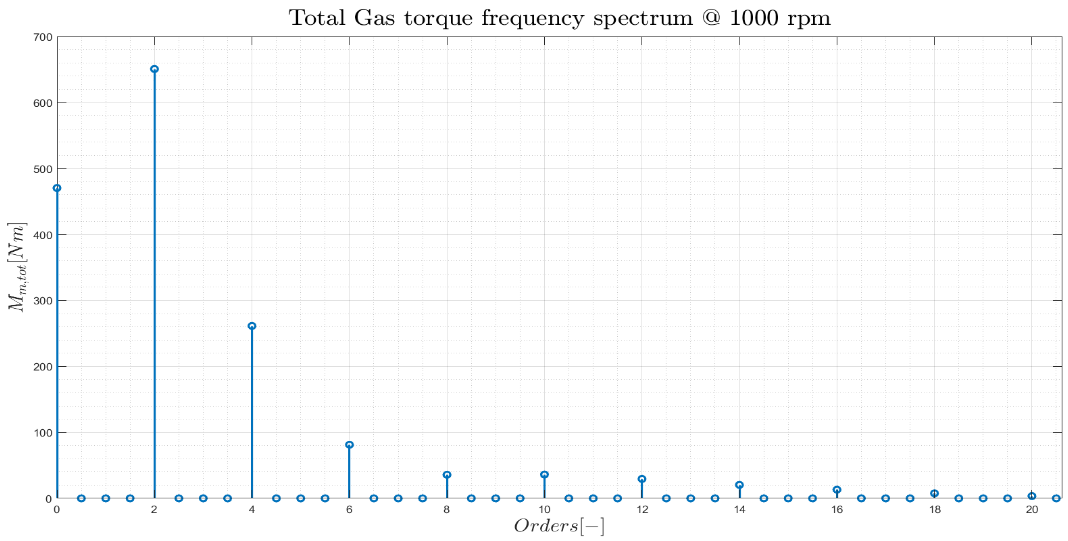

Figure 6.9: Singe cylinder gas moment frequency spectrum @ 1000 rpm

As shown in figures 6.8 and 6.9, order 2 is providing the biggest contribution to both the signals. This particular can be further highlighted in the following plot that compares the amplitude of each order at all the engine speeds used for evaluating the pressure cycle.

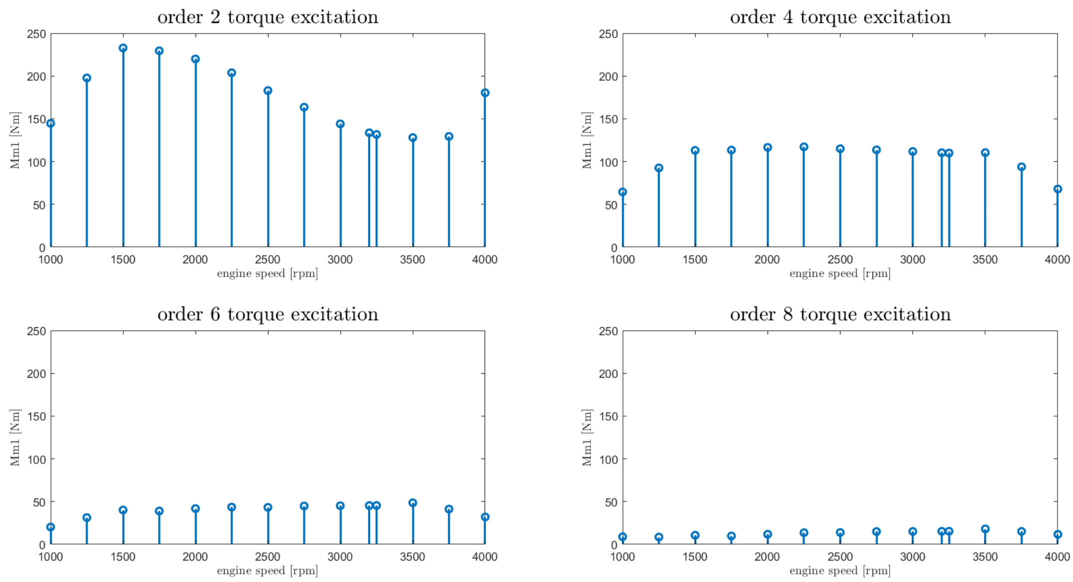

Figure 6.10: Orders amplitude comparison at different engine speeds

Also for these signals it is possible to apply the formula 6.1 to build the original inertial and engine moment signals as a function of theta in the interval 0-720 deg.

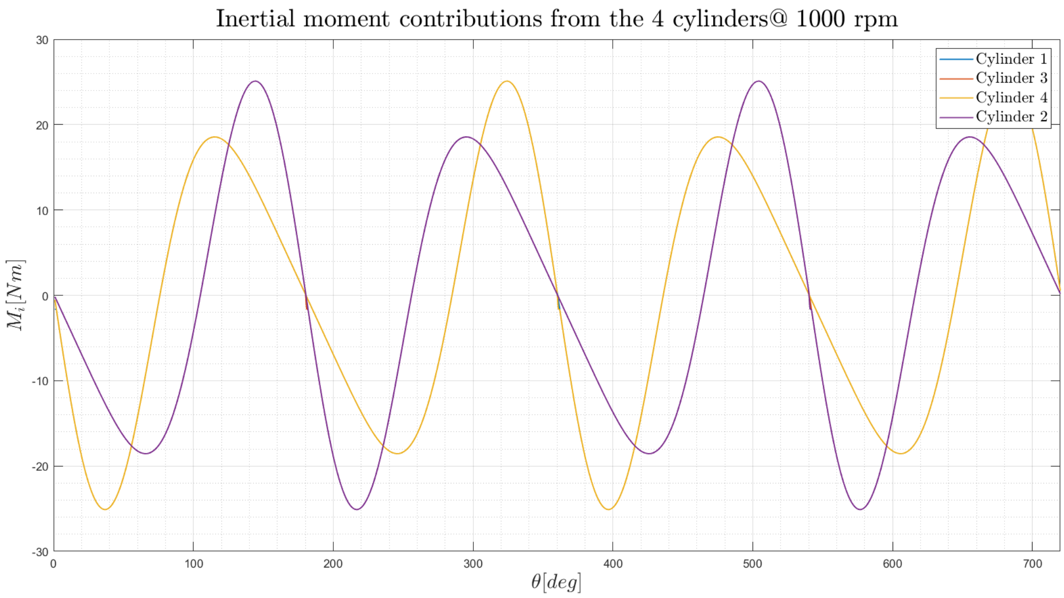

Figure 6.11: Re-builded inertial moment signal with all four cylinders contribution

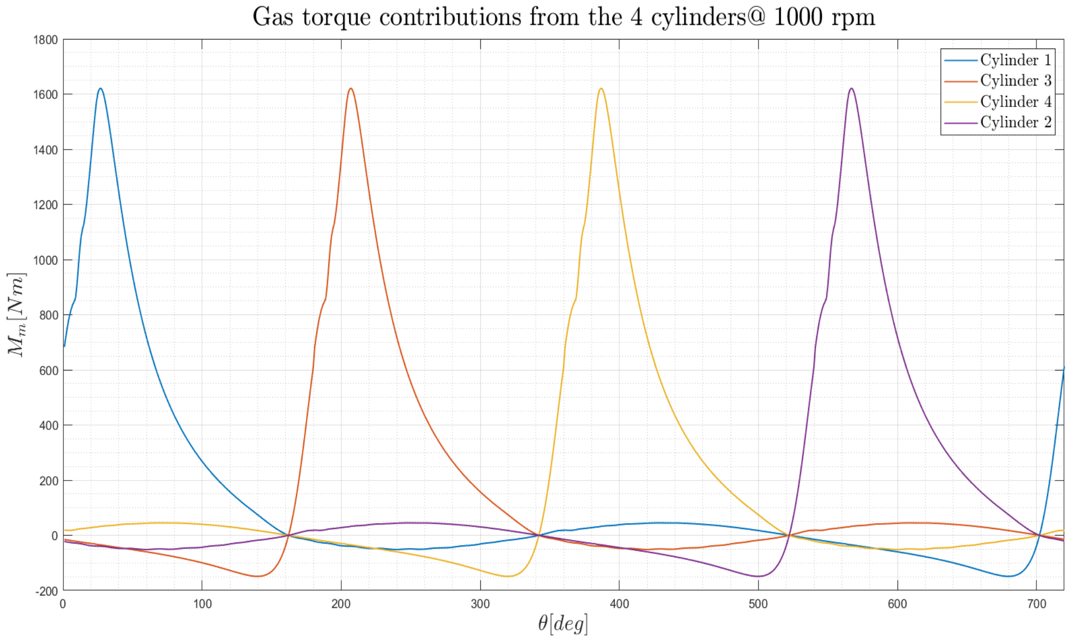

Figure 6.12: Re-builded engine moment signal with all four cylinders contribution

It is interesting to highlight the phasing between the four cylinders, already mentioned in chapter 3. The phasing keeps constant at 180° but, since the engine moment has a period of 4π, four peaks can be distinguished as in figure 6.12. This plot allows also to appreciate the firing order 1-3-4-2.Differently, the inertial moment has a period of 2π, so the contributions from 2 cylinders overlap (figure 6.11).
Comparing the re-builded engine moment signal to the original one and performing the rms calculation of the error it is possible to understand that going over 20 harmonics is not worth since it is reducing the error of only the 0.1%. Therefore, as anticipated in chapter 3, 20 harmonics are sufficient to accurately represent the engine moment with an error of around 3%. For what concerns the inertial moment, considering 20 harmonics, even an error lower than 1% is achieved.

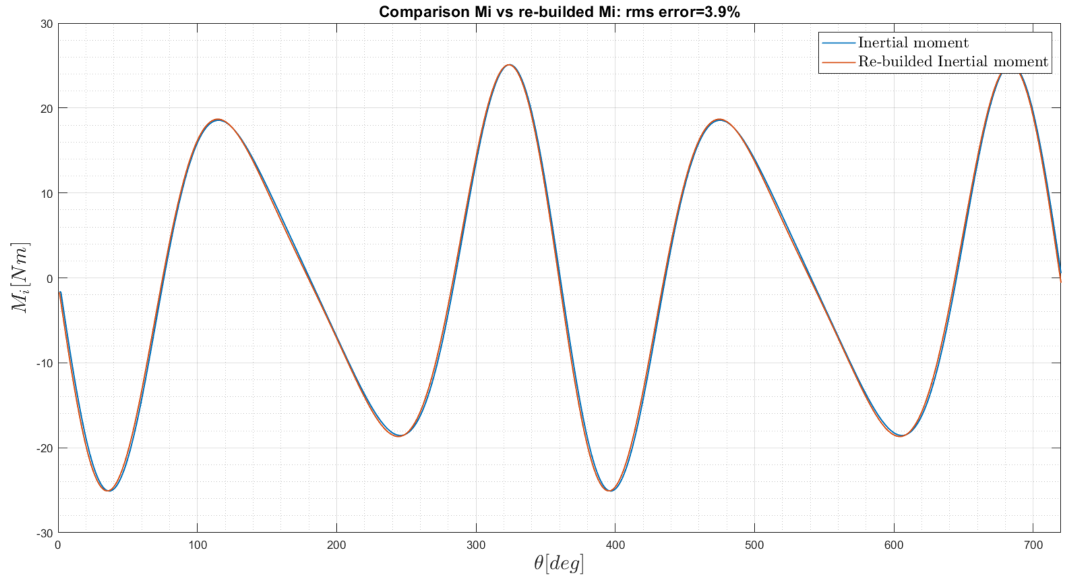

Figure 6.13: Comparison between inertial moment signal vs re-builded one

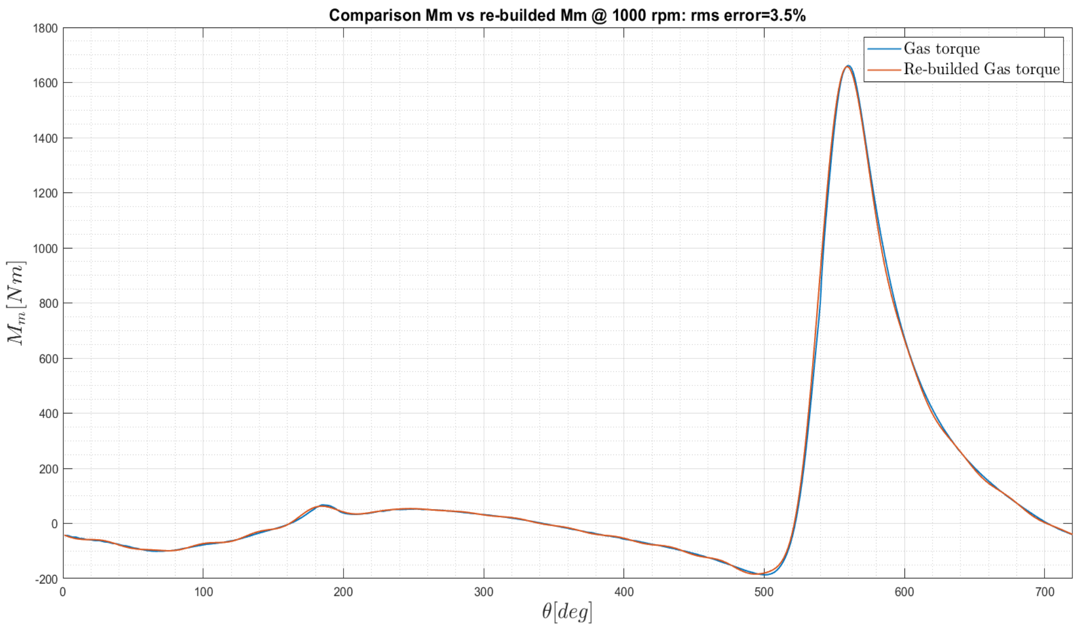

Figure 6.14: Comparison between engine moment signal vs re-builded one

6.4 Results

The equations of motions are solved using the receptance method therefore computing the dynamic stiffness matrix and then computing the response for each order for all the 14 engine speeds used in the definition of the pressure cycle.

$$[K_{\text{dyn}}] = [K] + i\omega[C] - [M]\omega^2 \tag{6.3}$$

$$\{x\} = \frac{\{M_{\text{tot}}\}}{[K_{\text{dyn}}]} \tag{6.4}$$

Considering the undamped model it is possible to verify the Campbell diagram for the system with TVD shown in figure 6.7. When adding an high amount of damping the Campbell diagram becomes less precise.
The plot in figure 6.15 shows the presence of peaks of order 4, 6 and 8 that can be checked on the Campbell diagram.

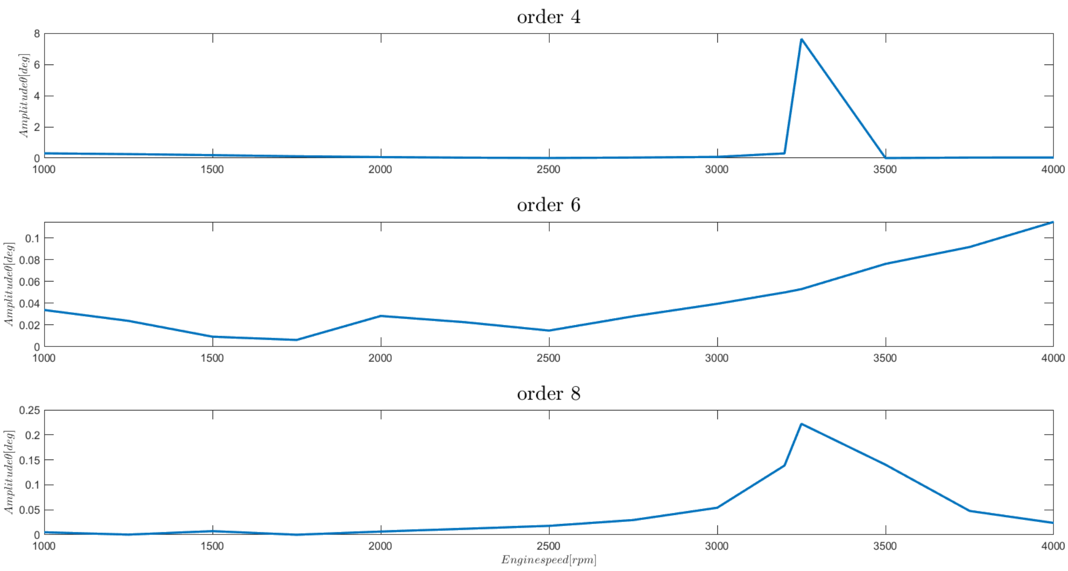

Figure 6.15: Hub amplitude plots from undamped system with TVD

In the following figure, the MATLAB model is used to compare the amplitude of response at the front-end hub to the one at the external ring.

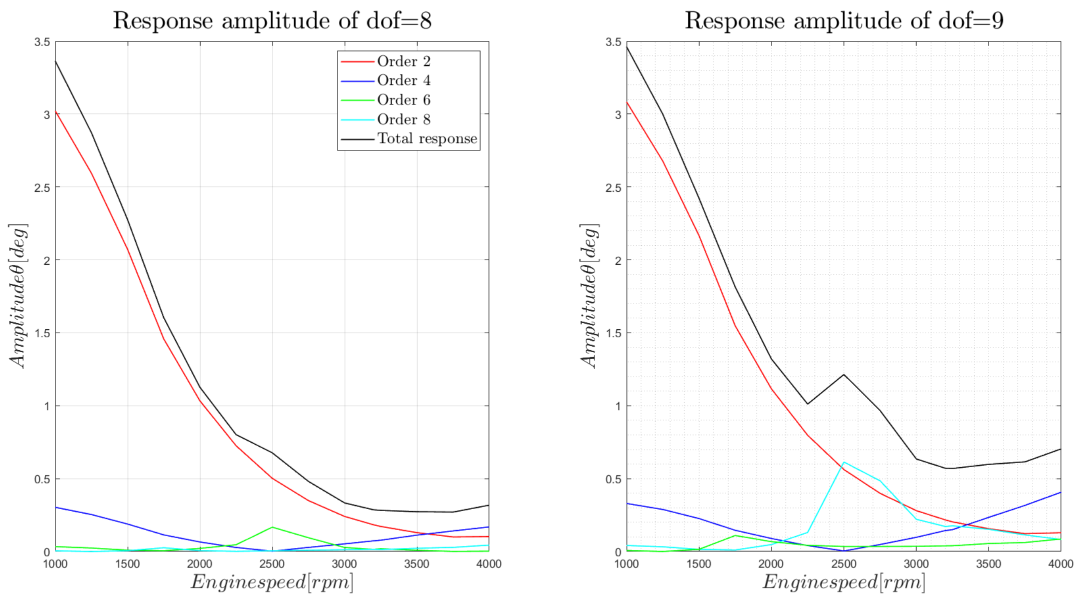

Figure 6.16: Comparison between hub and external ring amplitude

Figure 6.16 confirms that the external ring is absorbing mechanical energy on the hub side, transmitting it to the external ring.

6.4.1 TVD tuning discussion

In chapter 2, two possible approaches of tuning the TVD were introduced. The tuning frequency could be set looking at the response without TVD and setting the dynamic damper on the resonance frequency to be elminated. Even if this approach seems to be the most logical, for rotating machines the TVD tuning is based on the Campbell diagram, as already mentioned in chapter 2.
However, the tuning frequencies coming from these two approaches were compared using the MATLAB model together with another one in between. Furthermore, also the seismic mass and the TVD stiffness effect were discussed in figure 6.17 and 6.18.

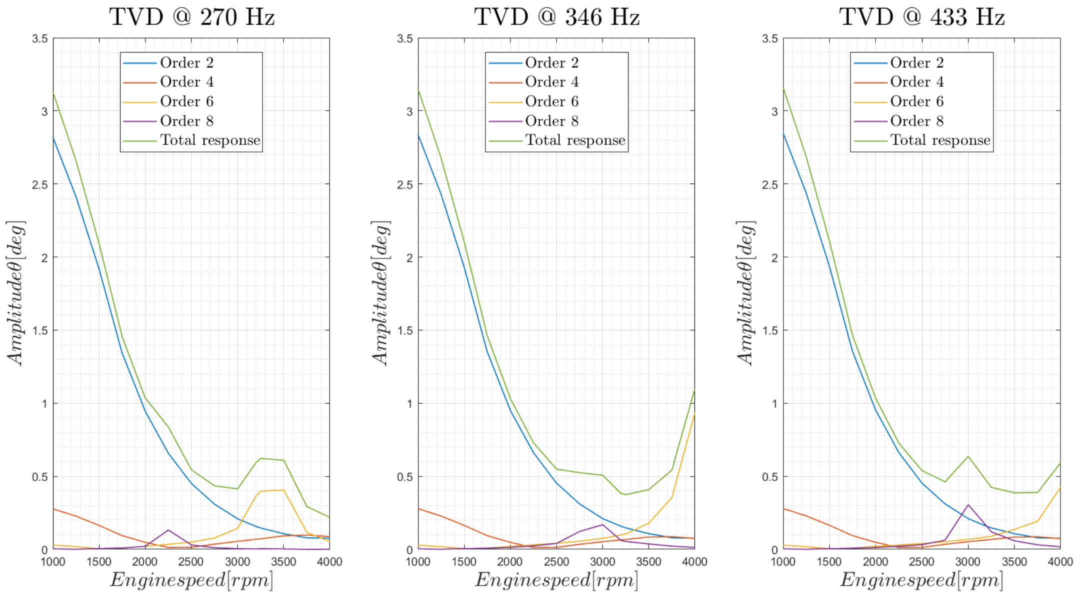

Figure 6.17: Tuning frequencies comparison acting on seismic mass

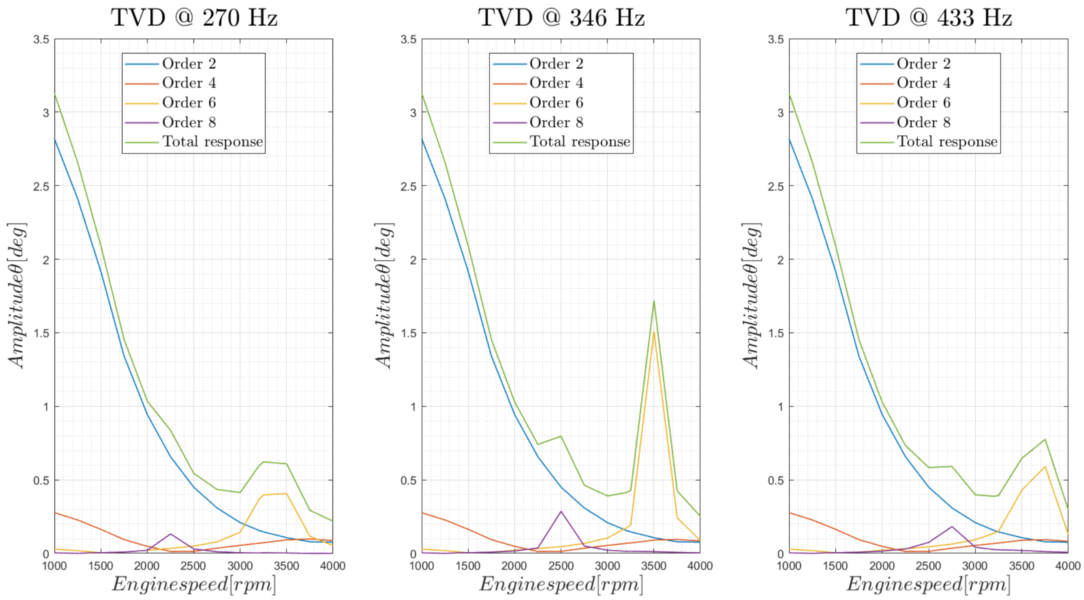

Figure 6.18: Tuning frequencies comparison acting on TVD stiffness

Figure 6.17 was computed keeping constant the TVD stiffness as it was tuned at 270 Hz and changing the external ring inertia to tune on the different frequencies. Figure 6.18 instead was obtained keeping the external ring inertia constant and changing the TVD stiffness according to the tuning frequency.
Based on the results just shown, the best tuning frequency appears to be 270 Hz as the Campbell diagram suggested, also compliant with the company's choice. This conclusion is not only based on the response that shows lower number of peaks but also on the behavior at high engine speeds. As a matter of fact, the tuning at 433 Hz in figure 6.17 seems to be almost as good as the one at 270 Hz but highlights an increasing hub amplitude going towards higher engine speeds. Therefore, the tuning suggested by the hub response without TVD is not suitable for the application.
In conclusion, a comparison between the TVD and no-TVD configuration of the crank mechanism is shown in the semi logarithmic plot in figure 6.19.

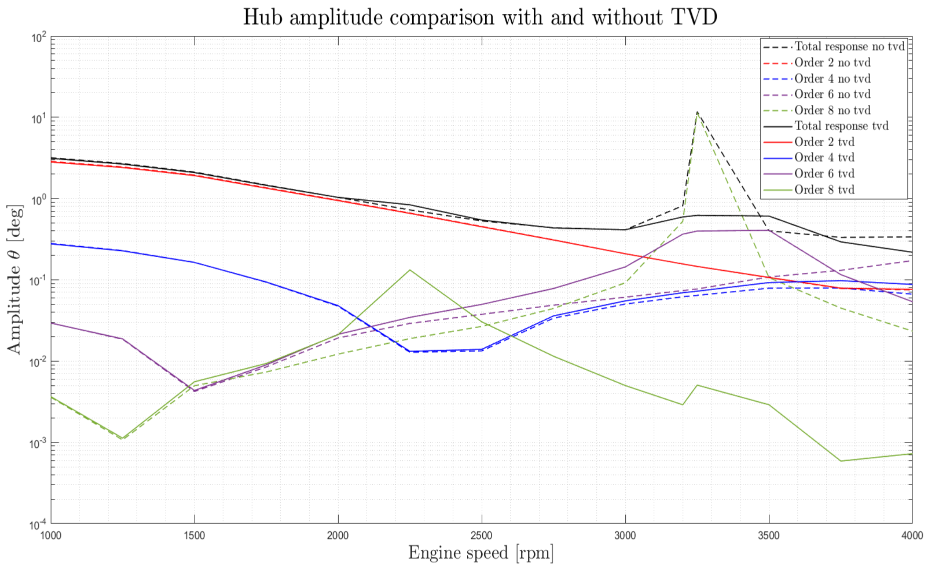

Figure 6.19: Hub amplitude comparison with and without TVD

6.4.2 Effect of damping contributions

Even if the damping contributions were known from the company, it was not possibile to use that data in the MATLAB model since they were expressed as percentage, suitable for using them in Gt-Ise. Therefore, the damping was tuned according to the bench test results with a lower resolution with respect to the more reliable data from the company.

However, this process was useful to understand the effect of the two different dampings acting on the crank mechanism.

As shown in figure 6.20, increasing the material damping leads to an almost unchanged amplitude of the total response but implies a modal coupling such that a non expected resonance peak is highlighted.

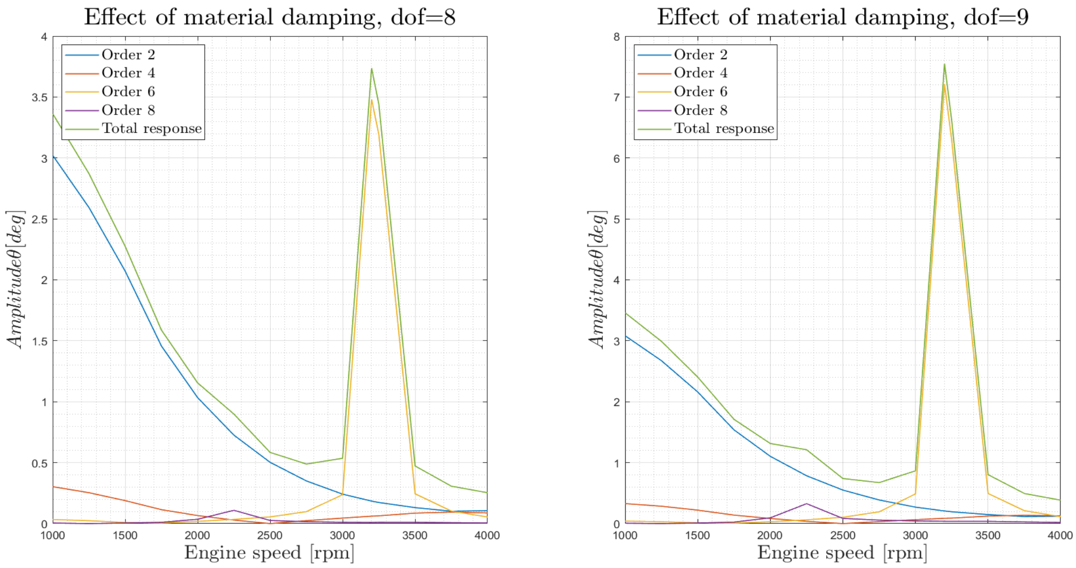

Figure 6.20: Effect of material damping on hub response

For what concerns the viscous damping, concentrated on the cylinders banks, it implies an amplification of the order 2 response while reducing the contribution from the other orders.

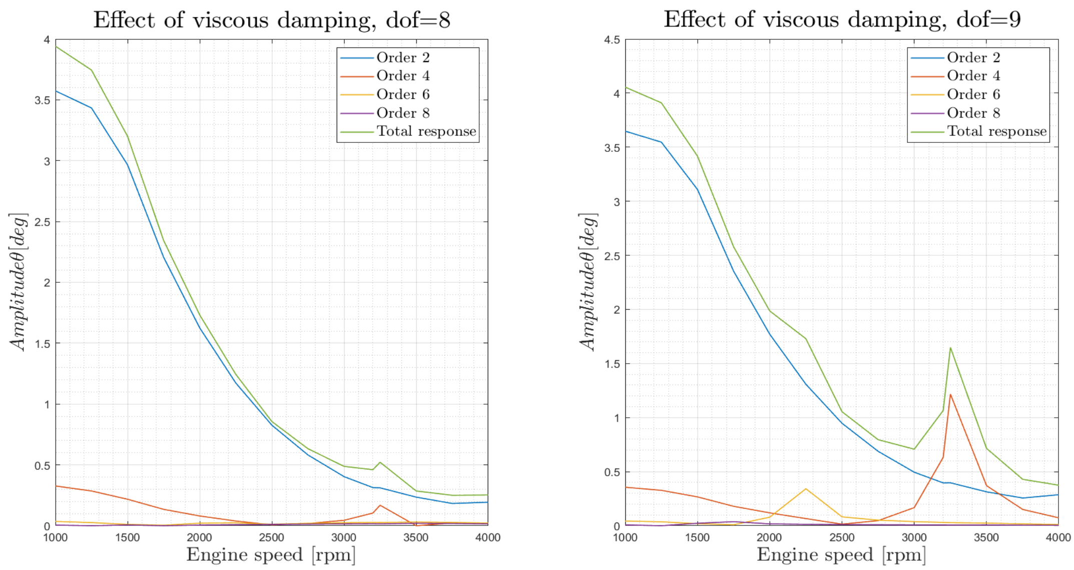

Figure 6.21: Effect of concentrated viscous damping on hub response

Chapter 7

GT-Ise model for crank mechanism

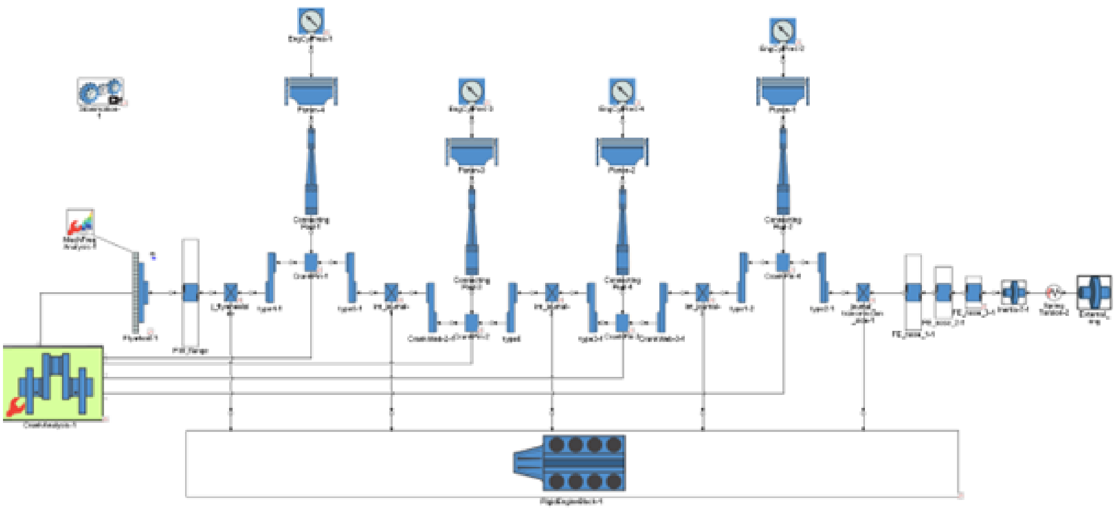

Figure 7.1: Overview of the GT-Ise model for crank mechanism

Following the execution of the torsional analysis utilizing a lumped parameters model in MATLAB, identical calculations will be conducted in GT-Ise. This is done to evaluate the validity of the aforementioned model and to serve as a foundation for the more comprehensive model of the crank mechanism in conjunction with the FEAD systems. GT-Ise enables the description of the crankshaft element by

element and serves as the environment for performing dynamic analysis of the crankshaft and FEAD system.
In this initial stage, GT-Ise will be employed to model the crankshaft and its components, as well as the FEAD system. The model will subsequently be refined based on bench tests of the dynamic response at the front-end level, and additional analysis will be introduced in relation to the FEM results.
Given the system's high sensitivity to vibration amplitude, a TVD and a vibration decoupler have been incorporated. Both components must be added to the model and accurately represented using the software's available components.
Once again, the objective of this simulation is to replicate the type of excitation introduced during bench testing, enabling a comparison of results with those obtained in the laboratory.

7.1 Input data

Differently from the MATLAB model, GT-Ise provides a user interface showing different blocks representing specific mechanical components such as crankpin, crankweb, connecting rod, journal, and flywheel.Their definition differs depending on the element itself, but all the physical data were to be provided.
Furthermore, the software provides simple components such as inertia, torsional spring and torsional damper to model more complex features that can be introduced in the model. These modules will be used to replicate the dynamic actions of TVD and decoupler.
In this phase, the same data used in the MATLAB model were set as input but GT-Ise needed also some details more that will be explained in this section.

7.1.1 Dimensions

The geometrical dimensions of the shaft's components were needed by the software to account for dynamic inertia contributions. The most important for an accurate computation was the connecting rod length. It is strictly linked to the above mentioned concept of rotating mass from the piston so highly influencing system's inertia.

This data was mainly found on the technical drawing of the shaft. As an assumption for journal and crankpin's lengths, they were considered at their joint to their elements at the sides. This is justified by the fact that the software uses single elements joint together.

7.1.2 Crank analysis

A crucial setting for the torsional analysis of the crank mechanism, is the definition of the crank analysis block. In this section everything related to the engine configuration is set. As anticipated in the MATLAB model, for a 4-cylinders in-line engine the phase delay of the cylinders is of 180°. The firing order was defined as well, set as 1-3-4-2.

7.1.3 Engine load torque

As known, the model that is being defined is excited by a load coming from the pressure input on the pistons.
For this reason the software needs to introduce a brake torque that represents the resistant torque coming from the transmission of the engine. Without introducing such a brake torque the crankshaft would have spinned towards very high speeds. In the model a torque element is introduced linked with an outwards arrow to the crankshaft representing the absorbed torque as shown in figure 7.2.

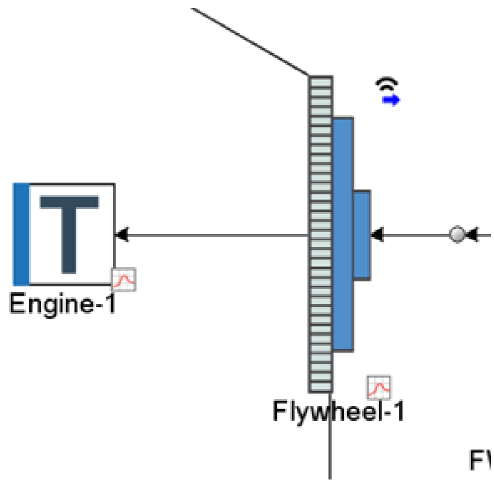

Figure 7.2: Detail on the braking torque linked to the flywheel side

The value of the braking torque was computed for each engine speed since a diffrent pressure cycle is being introduced. The value is obtained using the equation 3.30.

7.2 Comparison with another no-TVD model by supplier

The hub amplitude response results obtained from the GT model (figure 7.4) were initially compared to those obtained from another simulation from a company supplier (figure 7.3), already shown in chapter 2. This comparison served as the sole means of determining the adequacy of the results during this phase of the analysis. Notably, experimental tests were conducted on the entire crankshaft system, inclusive of both the torsional vibration damper and vibration decoupler modules.
The results from the two simulations are reported herein.

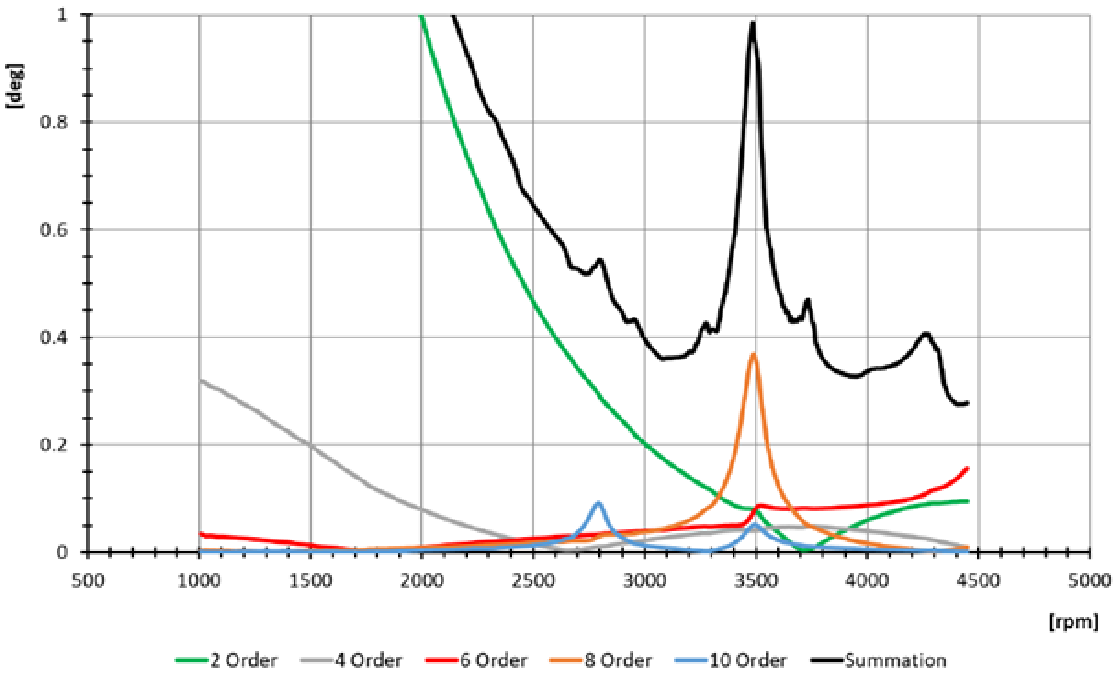

Figure 7.3: Hub amplitude response from supplier without TVD

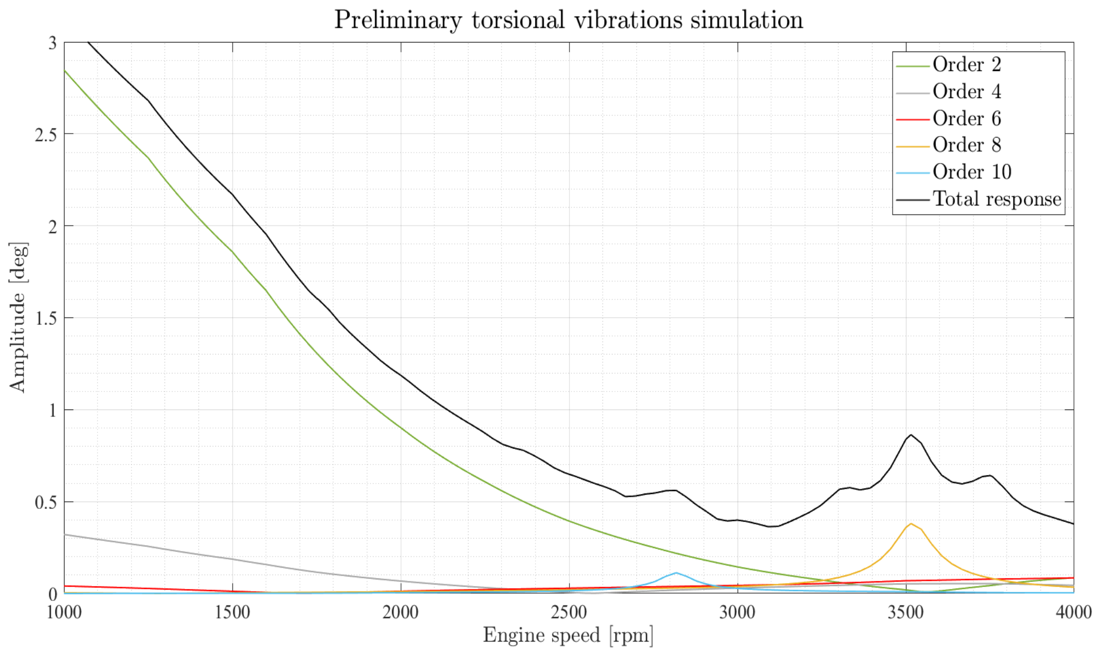

Figure 7.4: Hub amplitude response from GT-Ise model without TVD

As depicted, both simulations exhibit convergence towards the same trend for the orders, while also providing nearly identical amplitudes for each computed order. The estimated error is less than 5%, representing a satisfactory fit given the disparate approaches utilized. It is important to notice that the reference simulation employed a lumped parameter approach, in contrast to the element-wise evaluation applied in GT-Ise. Given its greater complexity, even when treated as a 1D system, it is probable that the new model provides better results.
This can also be attributed to the software's optimization for conducting crankshaft torsional analyses, with specific functions and solving algorithms designed for this purpose.
In conclusion, the current model is expected to describe the system with greater accuracy relative to the reference model, which was utilized solely for initial reference.

7.3 TVD and decoupler modelling

7.3.1 TVD

As far as the model is concerned, an equivalent torsional system to the one shown in figure 7.5 is needed. That schematic for a torsional system could be represented on GT-Ise as shown in figure 7.5.

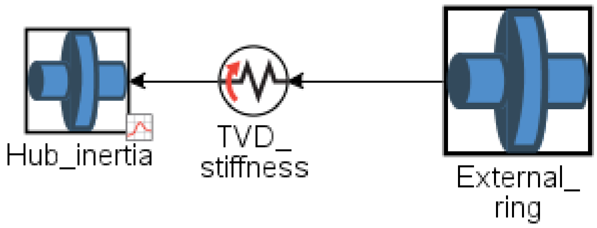

Figure 7.5: TVD model in GT-Ise

The tuning of the TVD stiffness is based on a fixed value of external ring inertia from the technical drawing of the company and the stiffness is computed as shown in equation 2.3.

7.3.2 Decoupler

A model similar to the one of the TVD is introduced for the decoupler. A sketch of its modelling is reported in figure 7.6.

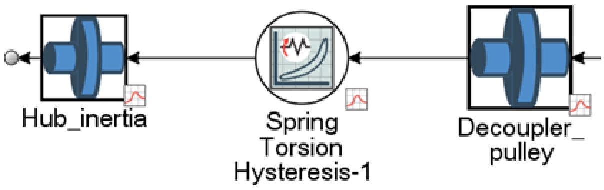

Figure 7.6: Decoupler model in GT-Ise

As it can be noticed, TVD and decoupler are linked with different rubber stiffnesses to the crankshaft hub. This implies that the models of the two components

will be sharing the hub inertia element with a different external ring.
However, the focus of this model is not on the computation of the correct stiffness as done for the TVD. This time, it is necessary to reproduce the decoupler stiffness characteristic which is represented in figure 7.7.

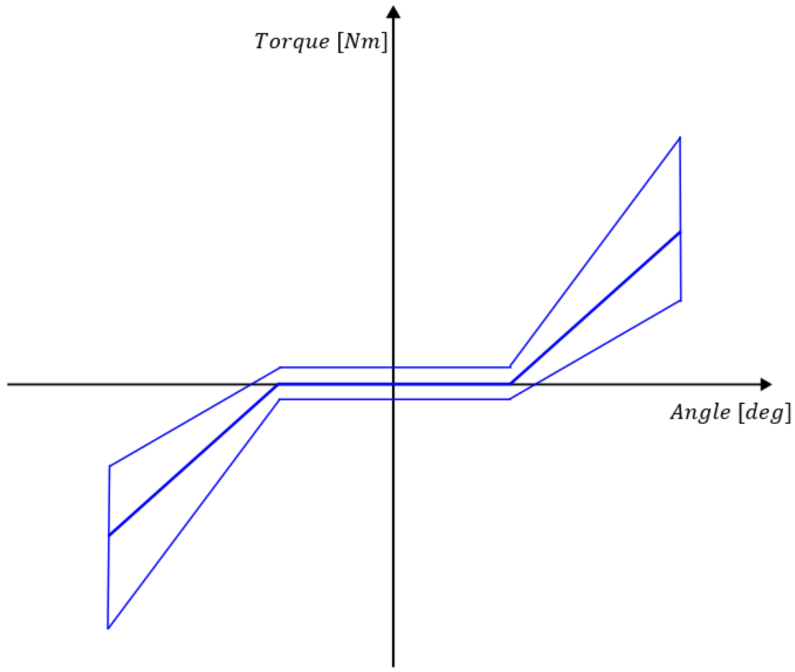

Figure 7.7: Decoupler stiffness characteristic

This characteristic is more complex than a fixed stiffness that was introduced in the TVD model. It is a stiffness with hysteresis with a 20° free angle that introduces a filter effect on the torsional motion between crankshaft and FEAD system.
This type of stiffness is not only variable as a function of the angle of torsion between the hub and the external ring but it is also introducing a certain amount of damping based on the hysteresis cycle just reported.
In general, the value of damping depends on the speed of the torsional movement. If a high speed movement occurs, the the resistance torque applied by this stiffness increases moving towards the maximum value for that angle of rotation. Therefore, the limits of the characteristic reported in figure 7.7, are representing the maximum counteracting torques that can be exibit by the stiffness but, applying a slower

torsion the stiffness provides a lower torque, because internal curves are to be considered. This can be clearly seen in figure 7.8.

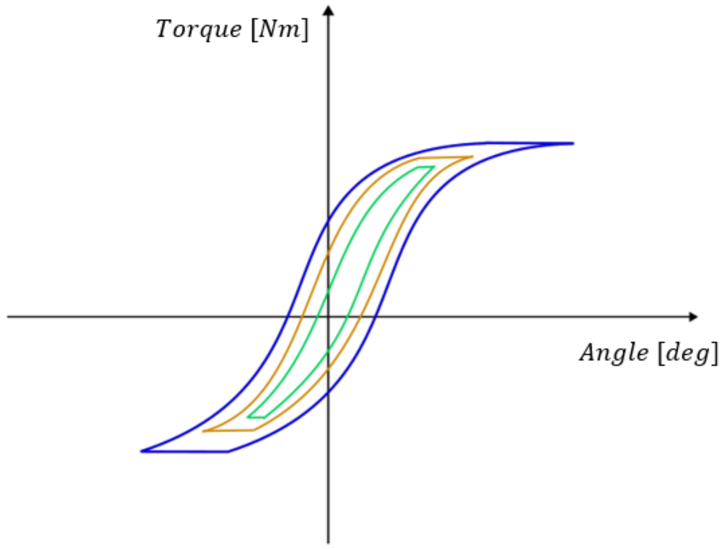

Figure 7.8: Example of hysteresis cycle for a stiffness

As anticipated, in the model the decoupler is again made of an external ring linked by means of a spring with hysteresis to the hub inertia in parallel with the TVD, as shown in figure 7.9.

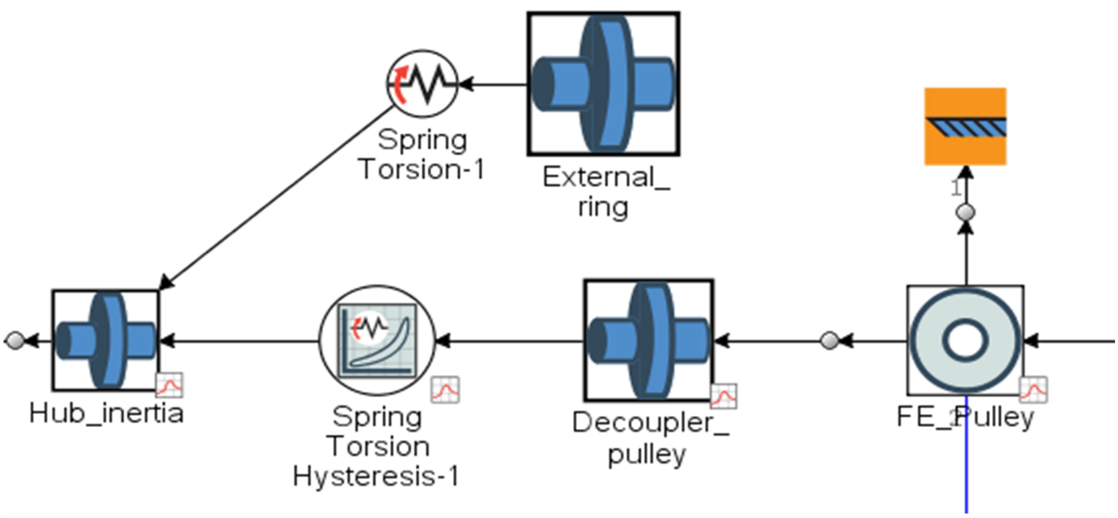

Figure 7.9: GT-Ise model for TVD and decoupler

The decoupler is then linked to the first rank of the FEAD system that is the main focus of the second part of the model because connected to the BSG pulley. As done for the TVD the external ring inertia is known from the company's drawing. Therefore, the main concern is modelling the spring torsion hysteresis block to represent the characteristic just shown above.
In GT-Ise it is necessary to define three functions to represent the limits of the curve and the nominal characteristic. The nominal function is a torque vs compression angle line that defines the main shape of the hysteresis cycle, as shown in figure 7.10.

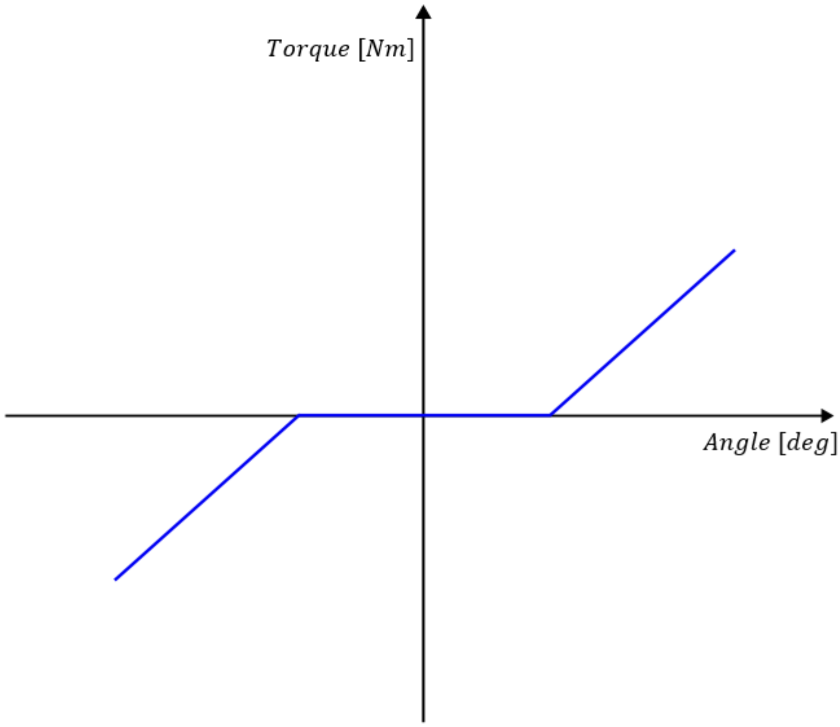

Figure 7.10: Mean decoupler characteristic

The upper and lower limit of the cycle are then introduced as offsets. Therefore, it is necessary to define two functions that represent the difference between from the upper/lower limit as function of compression angle. The upper and lower limit functions are diverging functions as shown in figure 7.7, therefore the following two offset functions were defined (figure 7.11 and figure 7.12).

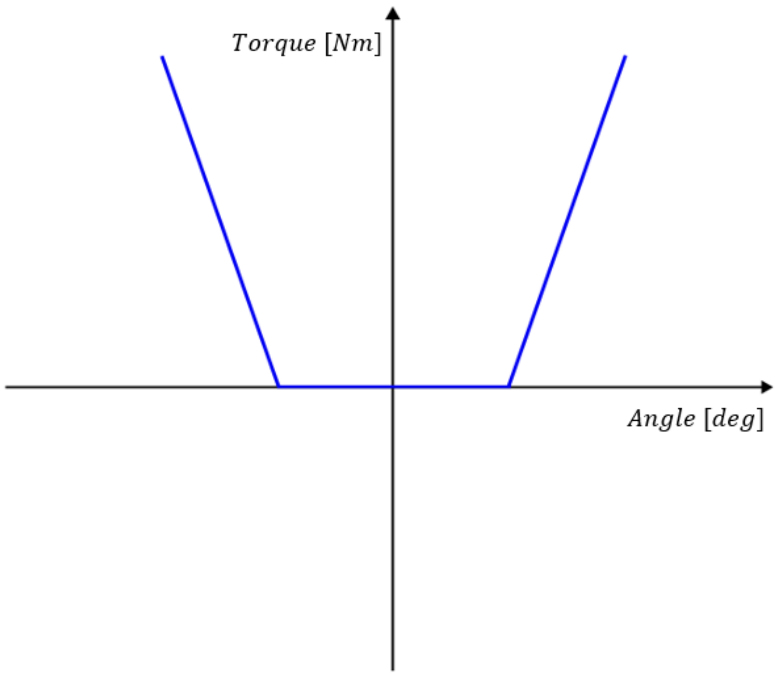

Figure 7.11: Upper offset function characteristic

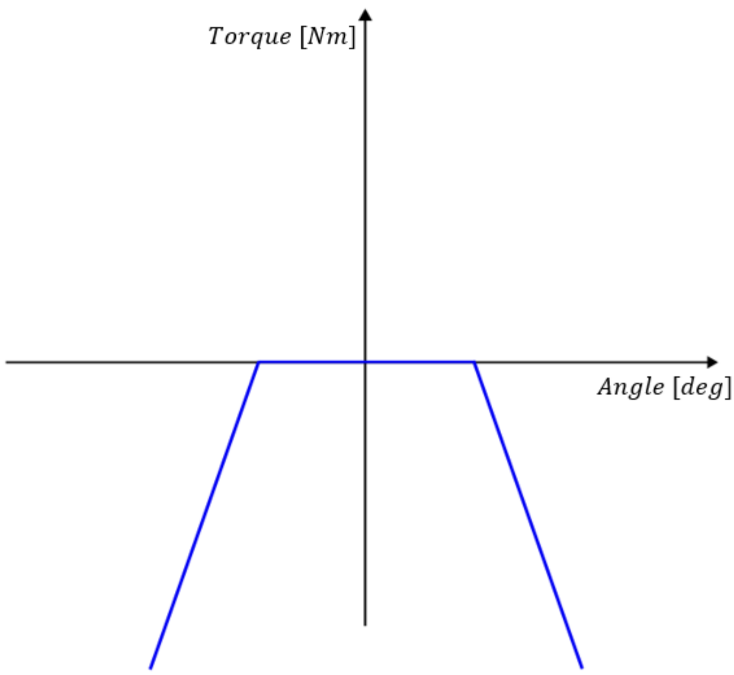

Figure 7.12: Lower offset function characteristic

Chapter 8

Bench testing comparison for model improvement

After constructing a model, it is essential to calibrate it to accurately represent real-world operating conditions. The calibration process typically involves referencing bench test results, such that after thorough calibration, the model can replicate the bench testing and become a powerful tool.
Unfortunately, the design in analysis wasn't yet tested by the company so there aren't any bench test results to tune the model with. However, since the crankshaft remained unchanged from the EURO 6 version of this engine, it was possible to compare its results with bench tests conducted in previous years by introducing minor modifications to the model.
As a result, even if the entire model could not be calibrated, at least the crank mechanism system could be further refined through this process, as the bench test focused on torsional vibrations at the crankshaft hub.
The EURO 6 model mainly differs for the lack of the electric machine. This implies two major changes:

1. the system has different natural frequencies, therefore the TVD has to be tuned to a different frequency;
2. no decoupler was needed.

For these two reasons, the TVD was modified introducing a stiffness tuned at 300

Hz and the simulation involved only the crankshaft focusing the frequency analysis on the crankshaft hub.
In order to accurately replicate the bench test to which the simulation will be compared, it was imperative to take into account the components connected to the crankshaft on the transmission side. The clutch and the electric engine were assumed to be rigidly attached to the flywheel, and thus, only their inertia was taken into account by incorporating it into the flywheel's inertia. This methodology introduces certain approximations, primarily due to the disregard of joint stiffness, which is substituted with an infinitely stiff contact. Despite this, this modeling approach is frequently employed by the company when dealing with these components. Moreover, it is plausible to assume that, owing to the high stiffness of the joint, this would not impact the frequency range under analysis but would affect higher frequencies.
The crankshaft model used for this purpose is reported in figure 8.1

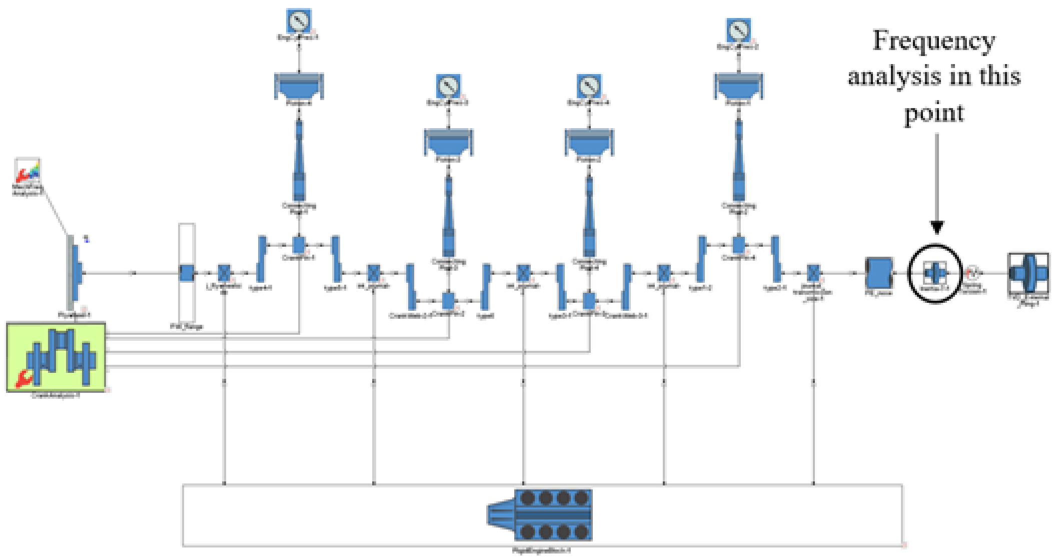

Figure 8.1: GT-Ise model for EURO 6 simulation

8.1 Bench test characterization

The bench test consisted of fixing the engine block to a ground reference frame and connecting it to the measuring instrumentation.

As the figure 8.2 shows, the engine must be connected to the fuel and air inlet (1) as well as the gas exhaust by means of pipes.

Figure 8.2: Engine bench test configuration

The measuring instrumentation is connected both to the transmission and front-end side of the crankshaft. On the transmission side, the crankshaft is connected to the clutch (2) and then rigidly linked to an electric motor (3) that provides a resistant torque equal to the one provided by the engine. This engine is controlled by a closed loop system to achieve the highest precision.
On the front-end side, the hub torsional vibrations are acquired by means of an optical encoder (4) as shown in figure 8.3

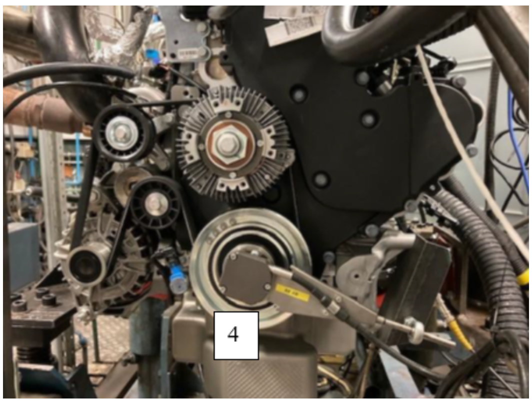

Figure 8.3: Detail on the front-end side of the engine

An optical encoder is an electromechanical device that consists of a rotating and stationary electronic circuit. The rotor is typically a disk with an optical pattern, specifically composed of opaque and transparent segments arranged in a gray-code pattern, that can be electronically decoded to generate position information. The stator has corresponding pairs of LEDs and phototransistors arranged such that the LED light shines through the transparent sections of the rotor disc and is received by phototransistors on the other side. Displacement is determined by counting the number of transitions that occur between logical values “0” and “1”. This enables the transformation of physical quantities by converting angular displacement variations into an electrical signal output that is translated into logical values by suitable electronics. The resolution of the instrument depends on the number of transparent/opaque sectors. Figure 8.4 shows an optical encoder highlighting its main components [18].

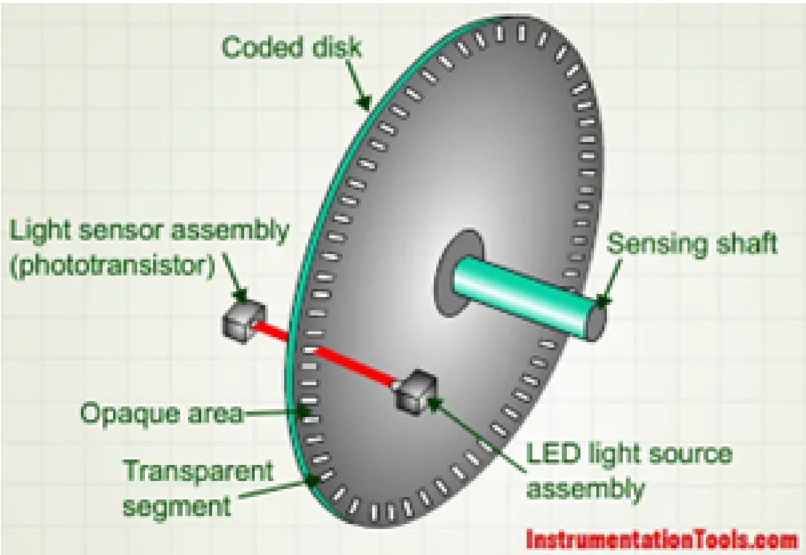

Figure 8.4: Example of an optical encoder [18]

The signal coming from the encoder is after amplified and converted such the position can be evaluated. This process is achieved by a signal multiplier and a Scadas recorder that are shown in figures 8.5 and 8.6.

Figure 8.5: Signal multiplier used for bench testing

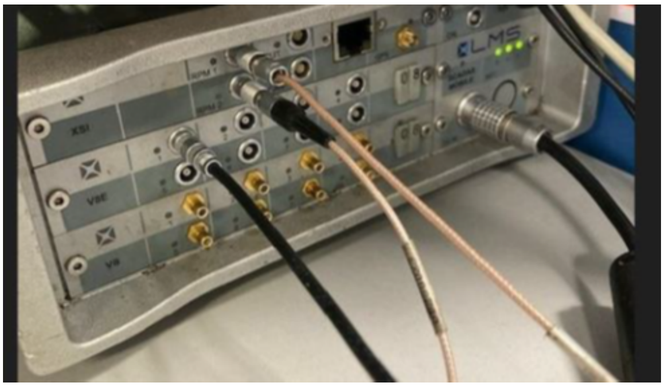

Figure 8.6: Scadas recorder used for bench testing

8.2 Results

The amplitudes of the bench tests are computed performing a mean average on multiple measurements where the engine is run slowly increasing the speed covering all the 1000-4000 rpm range. Each engine speed of interest is kept fixed for few seconds before accelerating to the next one such that this type of measurement returns almost the steady state value of the amplitude for each engine speed.
As demonstrated in figure 8.7, the model exhibits a high degree of accuracy when compared to the results obtained from bench testing. This is likely attributable to the high reliability of the input data, including the stiffnesses and inertia values computed from the CAD model. Additionally, the damping coefficients, which were suggested by the company's experience, also appear to be highly accurate.

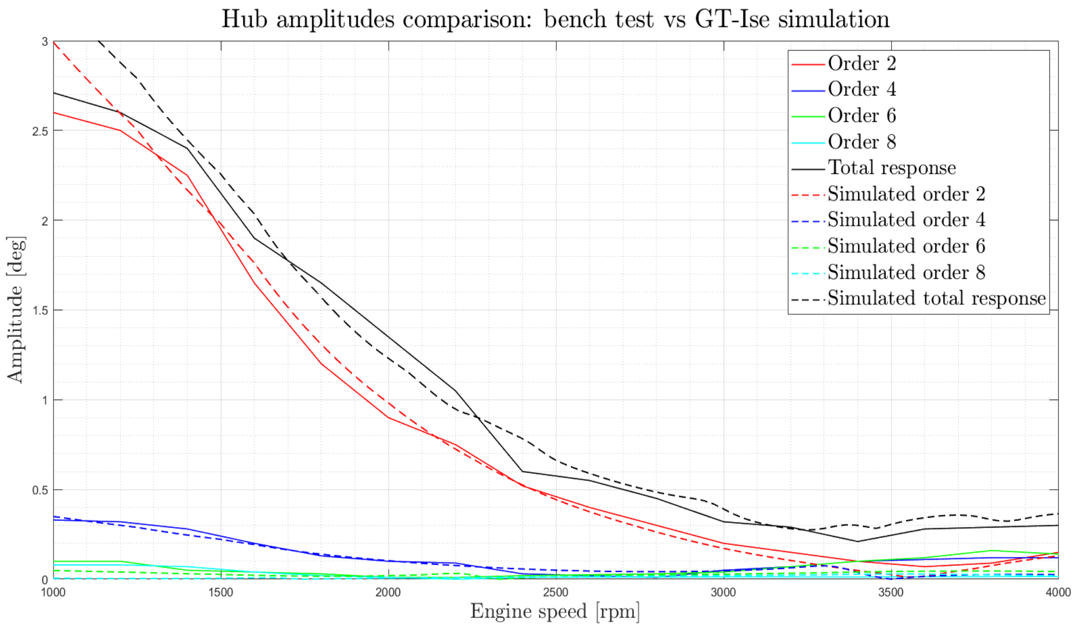

Figure 8.7: Comparison between bench test results and GT-Ise simulation

In figure 8.8 a detail on orders 4, 6 and 8 is shown.

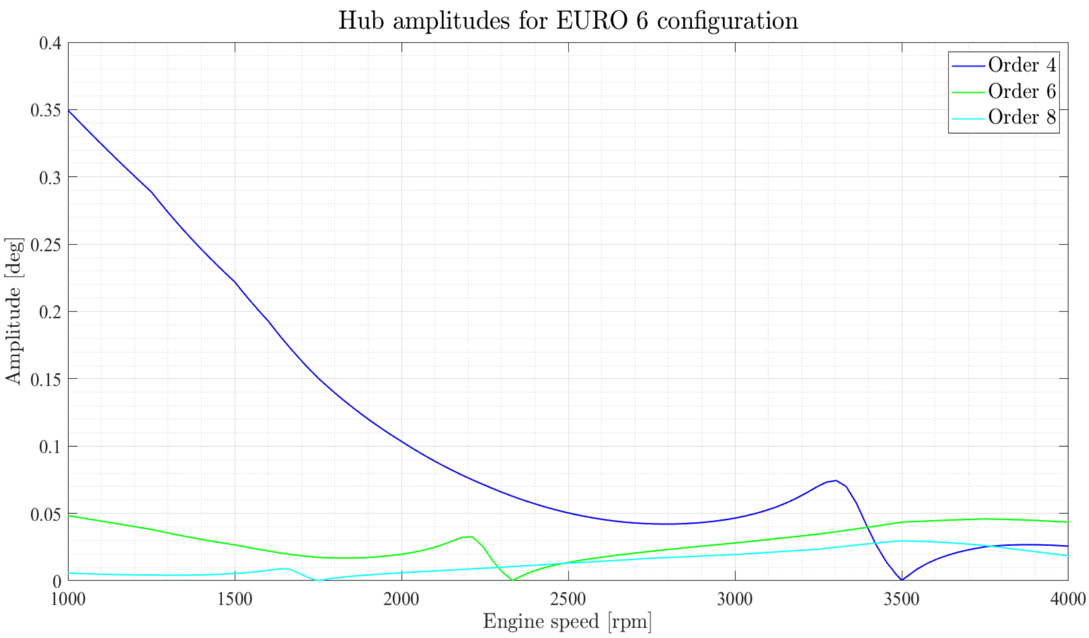

Figure 8.8: Detail on least important orders from GT-Ise simulation

The same hub amplitude plot was computed with the MATLAB model in chapter 6, therefore a comparison between that simulation and the bench test could be introduced.

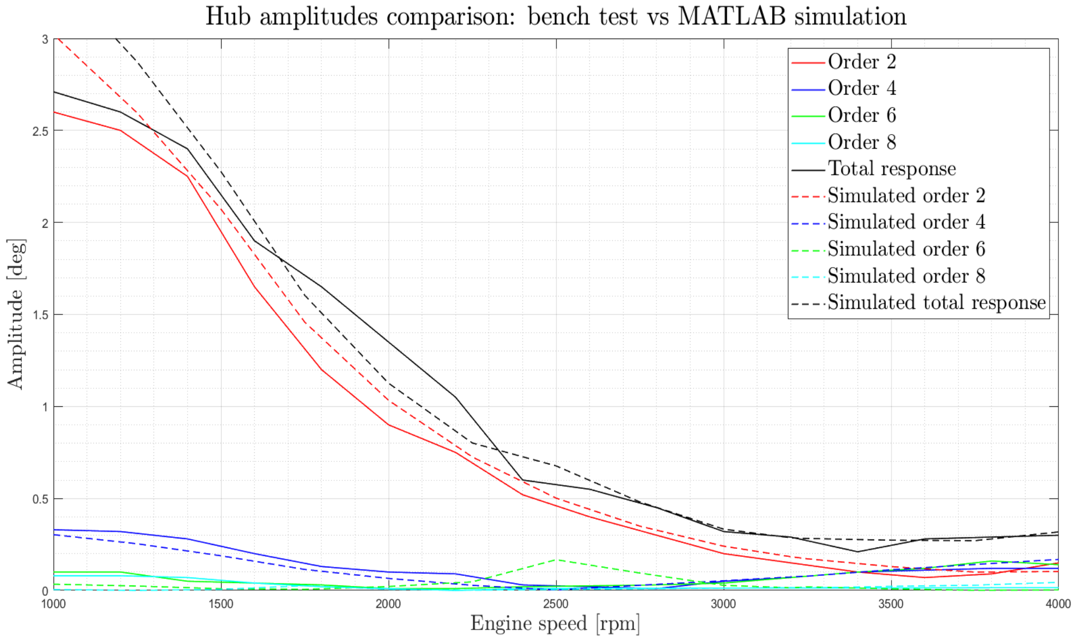

Figure 8.9: Comparison between bench test results and MATLAB simulation

Also the simulation from MATLAB, even with a simpler model than GT shows a good fit on the bench test results. The only noticeable difference is on the order 6 response where a peak is expected also according to the Campbell diagram. However, considering that the damping contribution in MATLAB cannot be as accurate as the one in GT-Ise, that is based on the company data, this phenomenon can be justified.

Chapter 9

GT-Ise model for FEAD

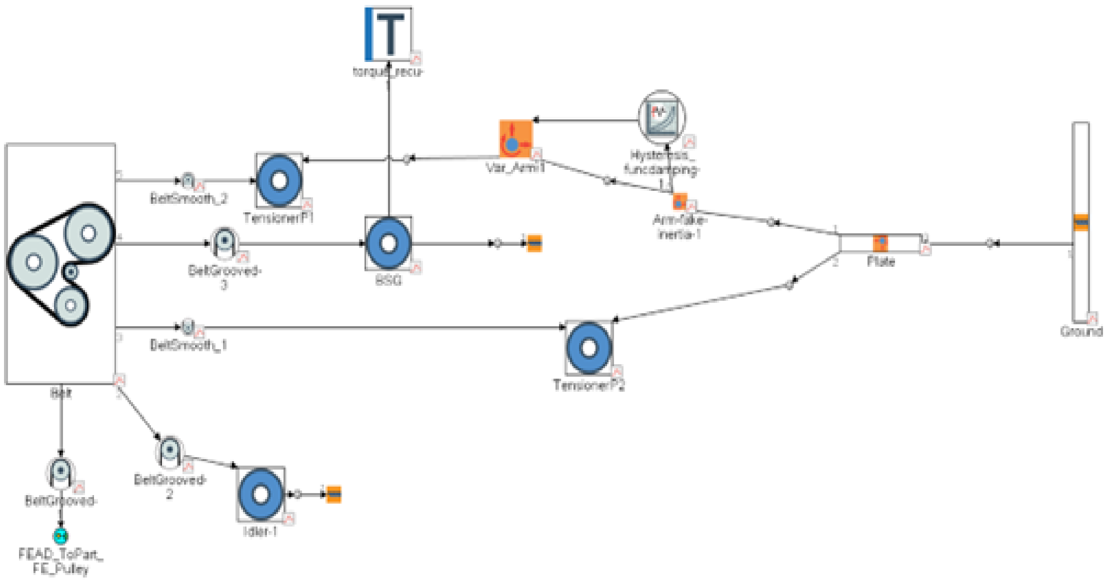

Figure 9.1: FEAD system GT-Ise model overview

9.1 Pulleys

The main component of a FEAD system are the pulleys that allow to introduce the correct transmission ratio between the crankshaft rotation and the accessories ensuring the tightening of the belt. Therefore, it was necessary to define the position of each pulley such that the right configuration was achieved.

This represented a crucial point for the model building because it hardly affects the results on the targets that are being discussed. As a matter of fact, the distance between each pulley is correlated to the belt tension that is the main parameter to be considered.
The position of each pulley was provided by the technical drawings from the company, in figure 9.2 a sketch is reported.

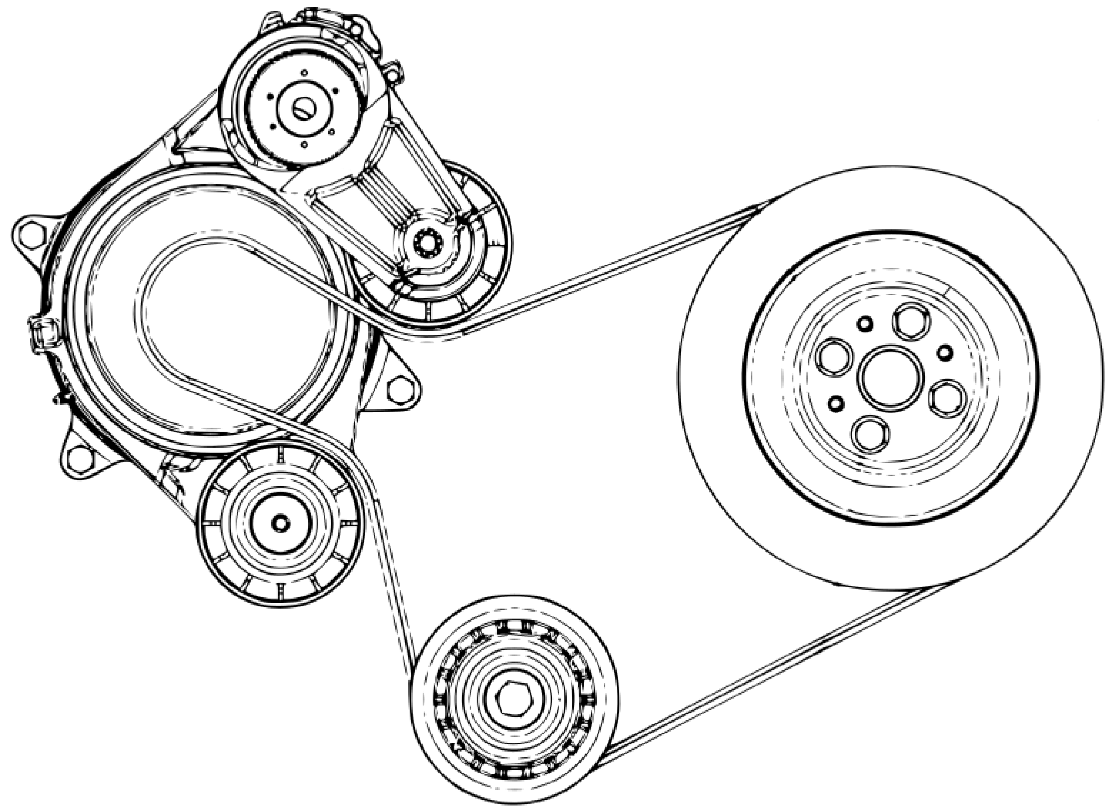

Figure 9.2: FEAD system sketch from company's technical drawings

As the picture 9.1 shows, the fixed pulleys were linked to a ground element that blocked their movement.
Another crucial point was defining the direction of rotation of each pulley such that the BSG could be fed with the right torque while both boost and recuperation phases. Starting from the crankshaft pulley that rotates clockwise as the other two fixed pulleys, BSG and idler while the two mobile tensioners rotate counterclockwise. For what concerns the torques, the BSG pulley switches from an absorbed to a

motor torque during the recuperation or boost phase since the automatic tensioner has two rotational degrees of freedom as shown in figure 9.3.

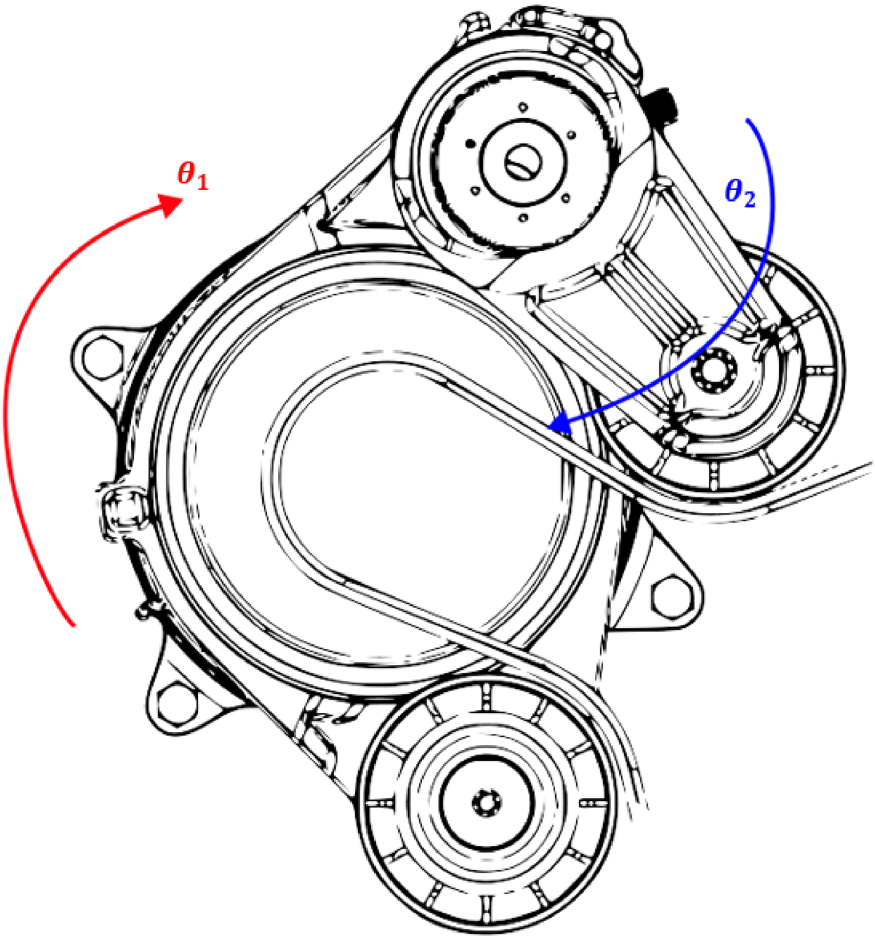

Figure 9.3: Detail on automatic tensioner's rotational degrees of freedom

However, the directions of rotation of the pulleys keep the same while the mobile tensioners change their position according to the working phase, as shown in the two following figures (9.4 and 9.5) from the simulations.

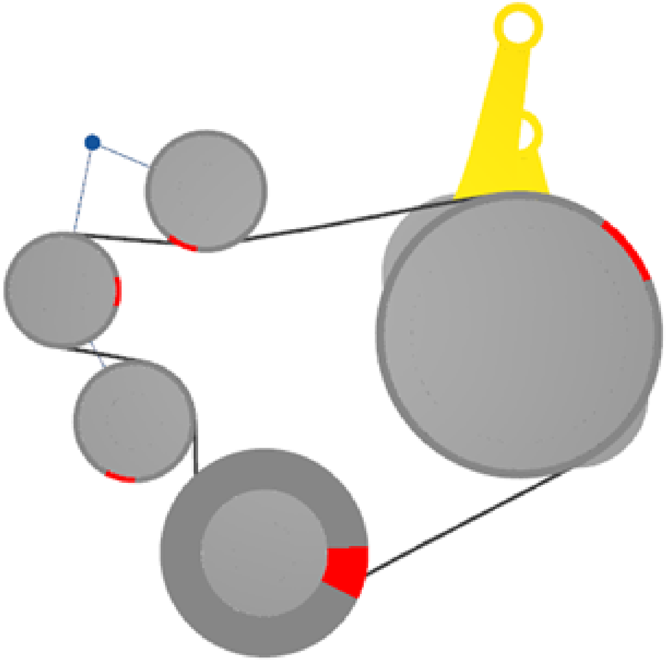

Figure 9.4: FEAD configuration during boost phase

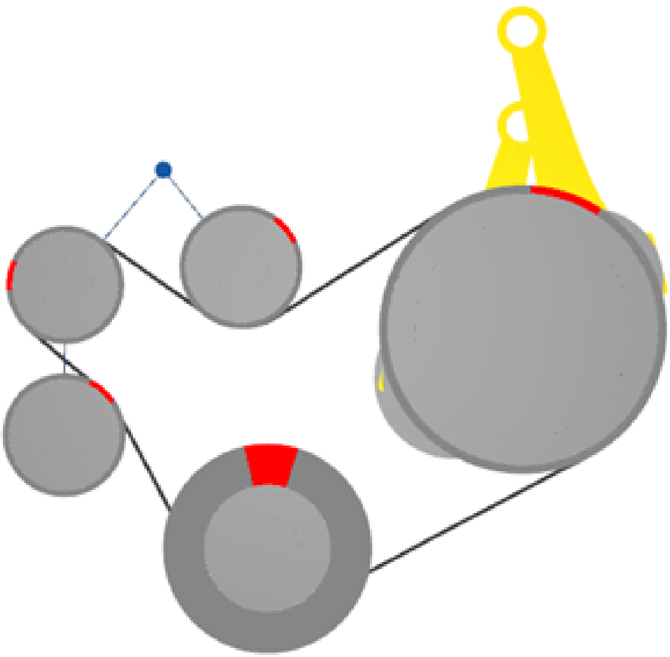

Figure 9.5: FEAD configuration during recuperation phase

9.2 Belt properties

The belt characterization is a crucial point to ensure the highest accuracy of the model. Furthermore, in this type of FEAD system, the belt plays an important role in the repositioning of the mobile pulleys while switching between the two working conditions. Indeed, the belt represents a further stiffness to the movement of the mobile tensioners.
In GT-Ise, all the needed properties for the belt and the features of its contact on the pulleys are introduced in the blocks belt and belt-to-pulley connection.
The belt in analysis is a poly-v rubber belt, which type finds large application in FEAD systems due to the high friction that can be reached. The V shape increases the surface of contact leading to equivalent static and dynamic friction coefficients above 1 [19]. An example of poly-v belt is reported in figure 9.6.

Figure 9.6: Example of a poly-v belt

In the belt block the axial stiffness and the sectional mass were introduced as provided by the belt producer.
Another crucial input is the belt pretension that is used by the softwer to compute the belt length, starting from the axial stiffness and the initial position of the pulleys.
In the belt-to-pulley connection block the contact was precisely defined introducing the static and the dynamic friction coefficient provided by the belt producer. It is

worth to mention that, as shown in picture 9.2, the belt touches the pulleys both with the grooved and with the smooth side, a detail on the grooved and smooth contact is here reported in figure 9.7.

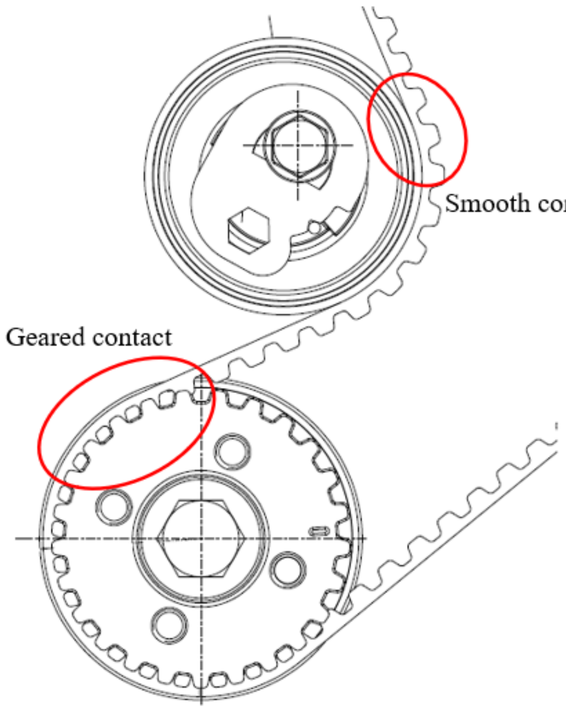

Figure 9.7: Detail on geared and smooth belt contact

For this reason in correspondance of the mobile pulleys, where the belt works on the smooth side, a different contact was defined with strongly reduced friction cefficients.

9.3 Main plate

The main plate is one of the two components that rotates on its own, introducing a degree of freedom to the standard fixed FEAD system.
The main plate was modeled on GT-Ise using a 2D-rigid body block where different nodes could be defined as shown in figure 9.8.

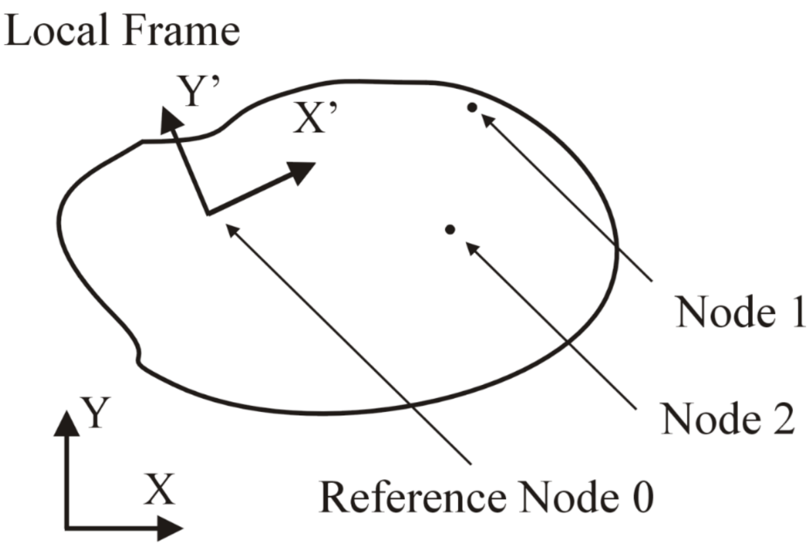

Figure 9.8: 2D rigid body nodes definition

This allowed to define as reference node the center of the BSG pulley that is the pivot of the rotation of the plate. For the mobile tensioners other two nodes were defined.
The mobile idler is just fixed on the main plate so one node of the main plate was defined starting from the initial position of the mobile idler. The second node was defined to fix the pivot joint of the side arm on the main plate thus allowing the rotation of the side arm on the rotating main plate, modelling the two degrees of freedom of this specific FEAD system. The main plate model can be schematized in figure 9.9.

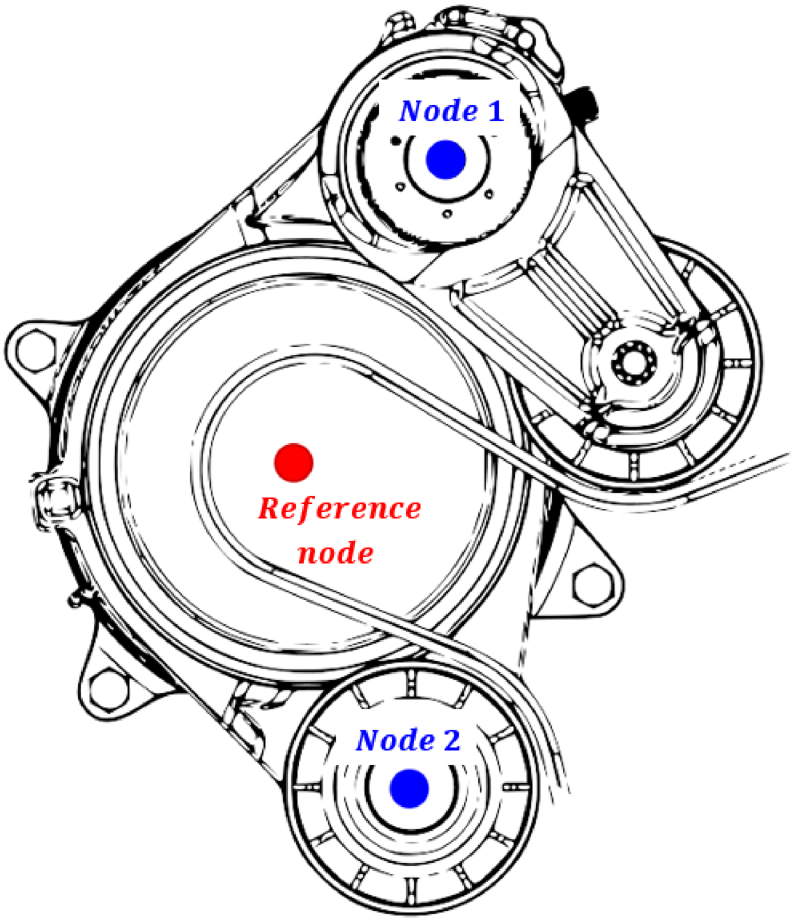

Figure 9.9: Detail on main plate's nodes

The main plate is at the end linked to the ground to its reference node position by means of a revolute joint that blocks all the degree of freedom apart from the rotation.

9.4 Side arm

The side arm is the most characteristic component of this FEAD system. As previously stated, it was designed to provide a further rotational degree of freedom so to allow the double working configuration in boost and recuperation.
The side arm is jointed on the main plate, connected to the node 1 by means of a revolute joint so that the main arm is not able to move but only to rotate.

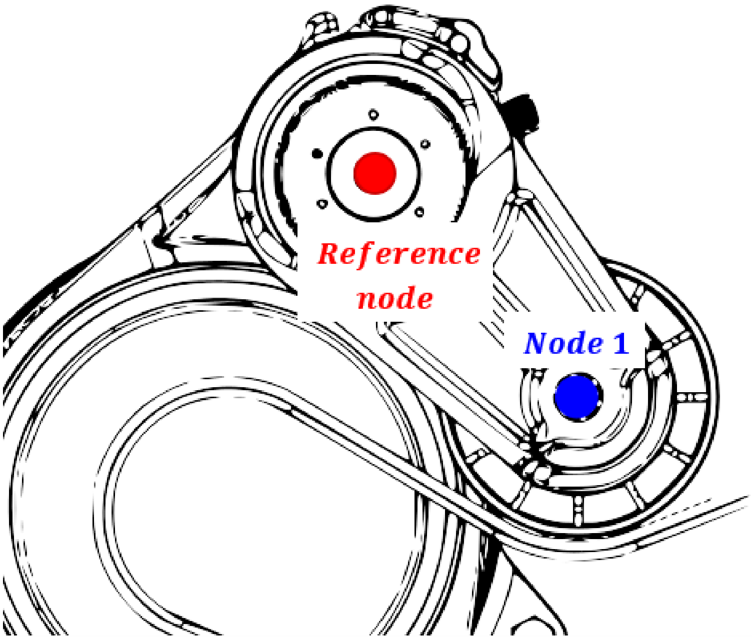

Figure 9.10: Detail on side arm's nodes

To limit the possible rotation of the arm, a spring with hysteresis was introduced. It is the same type of mechanical component used in the decoupler that brings both a stiffness and a damping action to the system.
The hysteresis characteristic of the spring consists of a linear torque with a nominal value at the starting angular position while the damping torque is introduced by means of a constant positive and negative offset.
In GT-Ise a straight line was used to represent the nominal torque that acts as a stiffness because it introduces a counteracting action on the arm. It is worth to mention that a total travel was introduced to the rotation of the arm so that the system can't exceed certain amplitudes. For this reason, the line is limited to a range of 55° and the software applies a constant torque when this maximum amplitude is reached. A qualitative example of the characteristic is shown in figure 9.11.

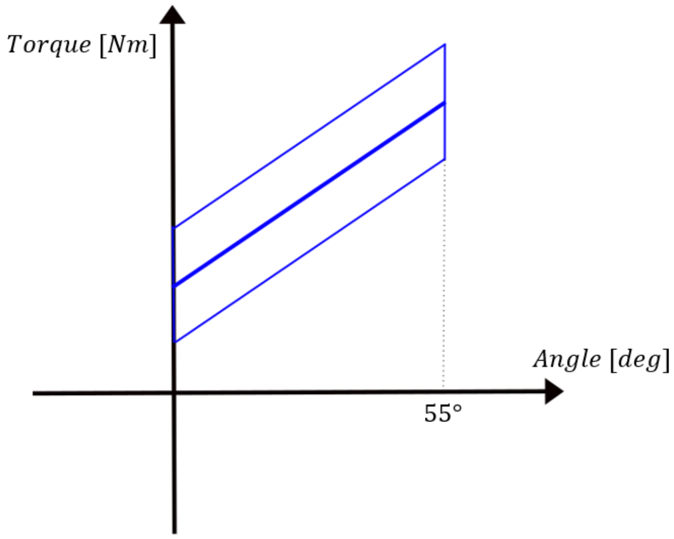

Figure 9.11: Side arm's hysteresis characteristic

The spring with hysteresis was placed between two 2D inertias elements for modelling reasons.
Therefore, a negligible inertia was needed, reported as fake inertia.As the figure 9.12 shows, the fake inertia was rigidly connected to the first node of the main plate and linked to the other inertia element by means of a revolute joint in parallel with the spring-hysteresis element.

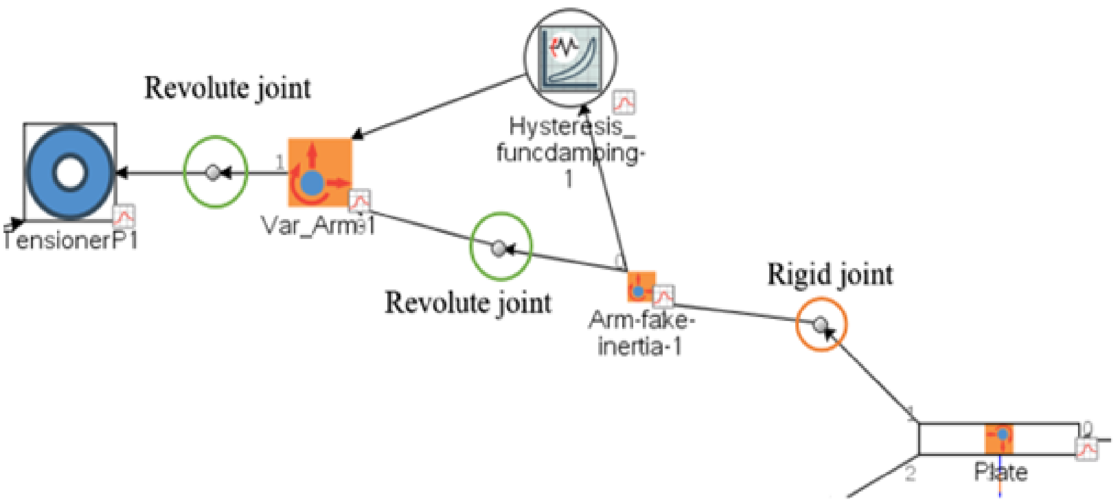

Figure 9.12: Detail on side arm model

The second inertia was again modeled with two nodes. The reference node corresponds to the one of the fake inertias so the node 1 of the main plate. The node 1 of the arm is then linked to the tensioner pulley by means of a revolute joint.
The fake inertia allowed to introduce the spring-hysteresis element thus reproducing the right behaviour of the arm.
In the animation section, GT-Ise reproduces a schematic structure of the main plate and side arm by means of small rods joint together, as shown in figure 9.13.

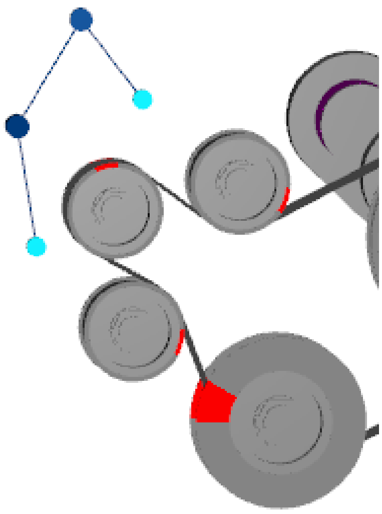

Figure 9.13: Main plate and side arm schematic structure

9.5 BSG brake and boost torques

The last step of the model is defining the external torque linked to the FEAD system. It is in fact necessary to define the recuperation and boost torque such that the BSG pulley absorbs or provides the correct torque.
These values are strictly linked to the characteristic of the electrical machine that takes part to the P0 hybrid engine. Starting from the maximum torque absorbed during recuperation and the one provided during the boost phase, the torques are computed based on the duty cycle of the engine.
The characteristics of the electrical machines are reported in figures 9.14 and 9.15.

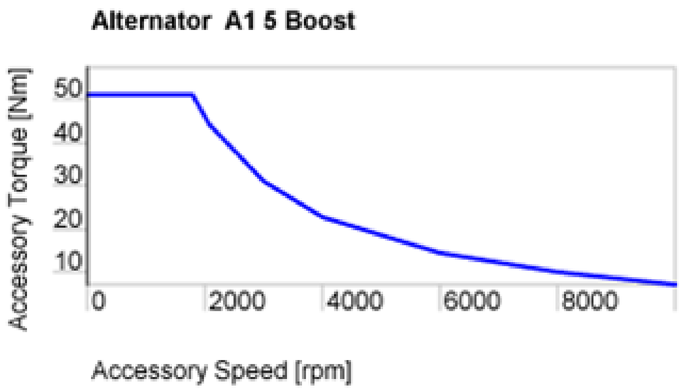

Figure 9.14: Electric machine boost characteristic

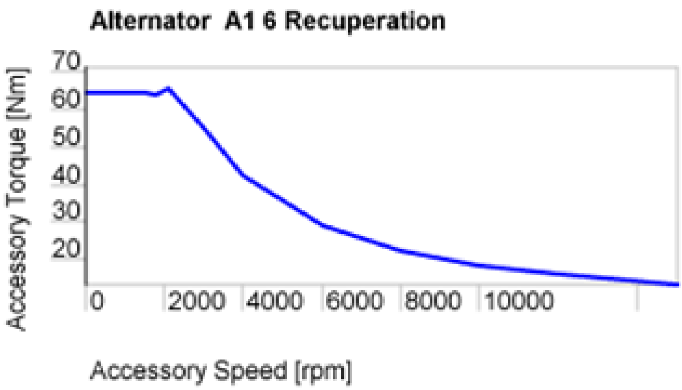

Figure 9.15: Electric machine recuperation characteristic

From these data, the input torques are computed for each accessory speed then reported to the engine speed by means of the transmission ratio, equal to 2.5 between the crankshaft pulley and the BSG pulley.
Following the company's guidelines for the validation of the targets in analysis the input torques considered for the boost and the recuperation phase were reduced with respect to the maximum ones shown in figures 9.16 and 9.17. The electric machines are never pushed to their maximum powers because of overheating incurrence. Furthermore, the company virtual validation is strongly correlated to the duty cycle of the engine validation where only lower torques are introduced to the BSG pulley. The following tables summarize the input torque values used for the simulations.

	CONTINOUS MOTOR			
	Mechanical power [W] at 120/85°C, 48V			
Engine speed [rpm]	BSG Speed [rpm]	mech. Power [W]	elec. Power [W]	Torque [Nm]
600	1500	2490	3070	15,9
800	2000	3590	4290	17,1
1200	3000	5010	5950	15,9
1600	4000	5800	7130	13,8
2400	6000	5700	7330	9,1
3200	8000	5990	7490	7,2
4000	10000	5770	7500	5,5
4800	12000	4920	7340	3,9

Figure 9.16: Input torques for boost phase

	CONTINOUS RECU			
Engine speed [rpm]	Speed [rpm]	elec. Power [W]	mech. Power [W]	Torque [Nm]
600	1500	-2310	-3050	-19,4
640	1600	-2490	-3230	-19,3
720	1800	-2930	-3710	-19,7
800	2000	-3350	-4160	-19,9
1000	2500	-4230	-5120	-19,6
1200	3000	-5500	-6440	-20,5
1600	4000	-6050	-7020	-16,8
2400	6000	-6770	-7970	-12,7
3200	8000	-6920	-8300	-9,9
4000	10000	-6690	-8030	-7,7
6000	15000	-6490	-8400	-5,3

Figure 9.17: Input torques for recuperation phase

These values are set as input to the BSG pulley and modeled in GT-Ise as shown in figures 9.18 and 9.19 by changing the direction of the arrow for input or output torque.

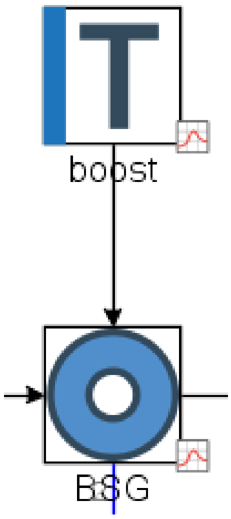

Figure 9.18: Boost torque

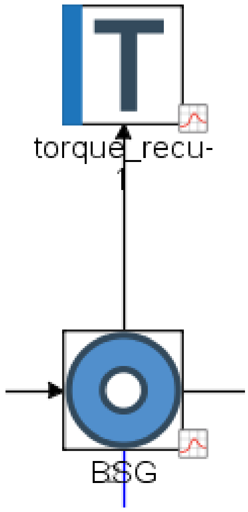

Figure 9.19: Recuperation torque

It is worth to mention that the model just completed is not able to perfectly replicate what happens during the boost phase. This is because everything depends on the power split management of the hybrid engine therefore, it is not possible to introduce the real pressure cycle at a certain speed when the boost phase is acting. For this reason, the boost model is only considered for a qualitative analysis of the system while working in different conditions.
On the other hand, the recuperation model appears to satisfy the requirements since the pressure cycle of the ICE keeps the same, but a certain torque is absorbed by the BSG pulley.

9.6 Crank mechanism and FEAD systems model

The model for the FEAD has now been finalized, thus enabling its integration with the pre-existing and calibrated model of the crank mechanism. This amalgamation facilitates comprehensive discussions pertaining to the objectives and the influence of the TVD and decoupler. The full model is shown in figure 9.20 in the next page.

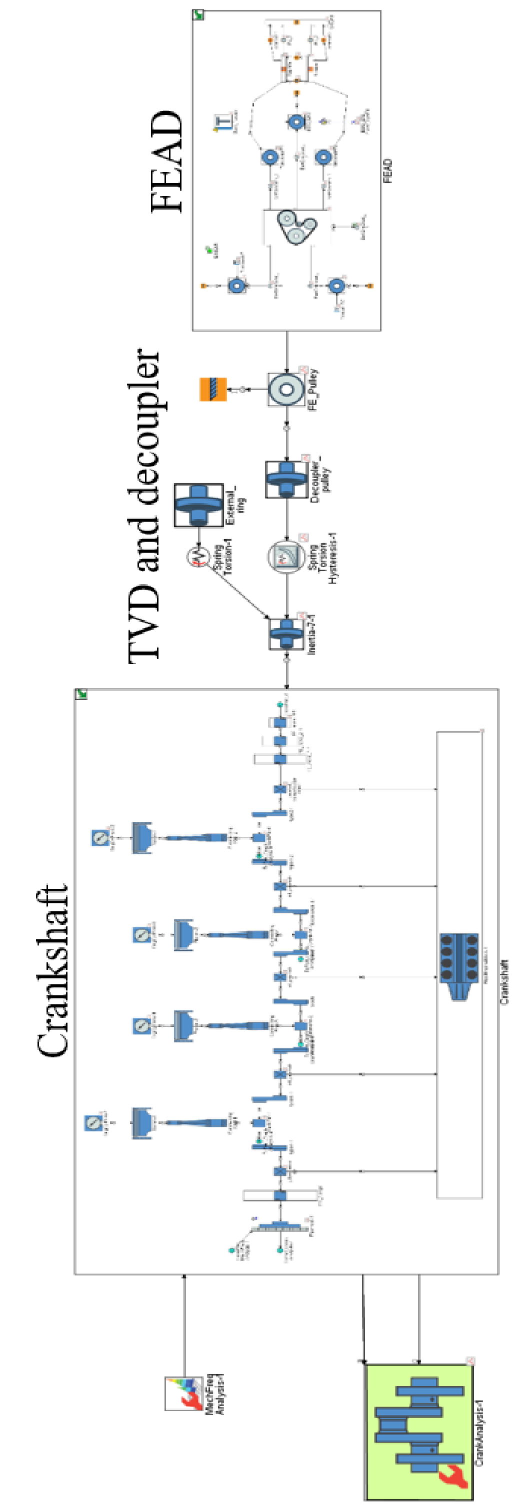

Figure 9.20: GT-Ise full model for target evaluation

Chapter 10

Possible designs results

As anticipated in the first chapter, the systems in analysis are often provided of a TVD and a decoupler to increase their torsional vibrational preformances therefore, their effects will be discussed in this chapter. Furthermore, based on simulation results, the company's targets will be computed thus discussing whether these two components were needed or not.

10.1 TVD effect on crank mechanism's dynamics

The torsional vibrations damper was added to the hub of the crankshaft to fulfill the requirements of amplitudes, internal torques and tightening torque on the front-end. As anticipated in figure xx (quella del campbell diagram), the Campbell diagram highlighted that the best tuning frequency was of 270 Hz but, due to the production process of the rubber stiffness, an operative working range should be considered rather than a precise frequency. The TVD producer guarantees a precision of ± 20 Hz. In this section the effect of the TVD will be discussed, at first looking at the benefits of its addition, and then evaluating in detail the different performances inside the working range.

10.1.1 Amplitude

Based on its experience, the company set $0.5°$ of amplitude for the total frequency response without considering the order 2. The second order is introducing the

highest peaks at low frequencies, but it mainly affects the FEAD dynamics, therefore it is treated by means of the decoupler.
The figure 10.1 shows the amplitude frequency response without TVD. Since the total response is exceeding the target value, the vibrations damper is strictly needed.

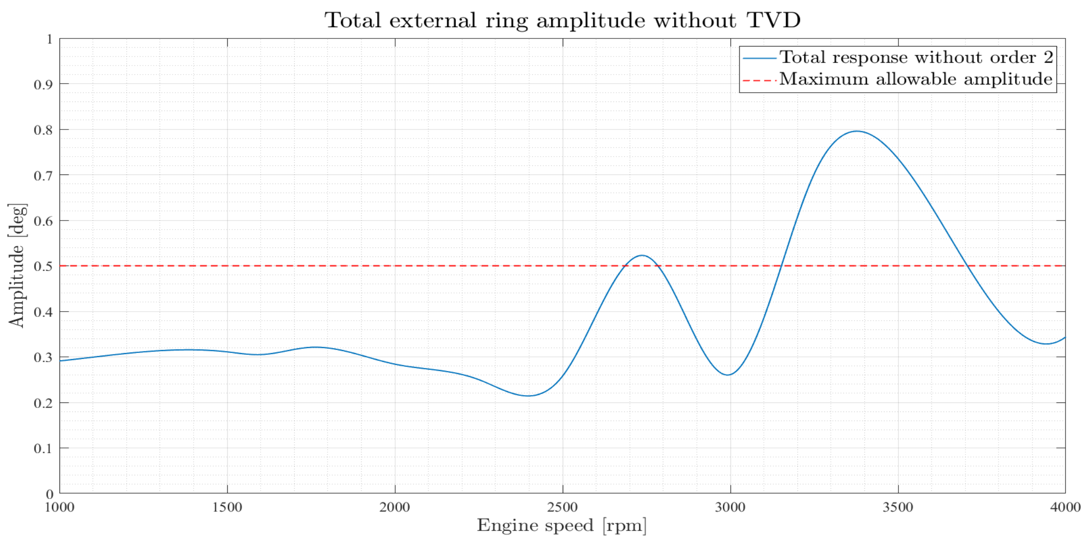

Figure 10.1: Hub external ring amplitude without TVD

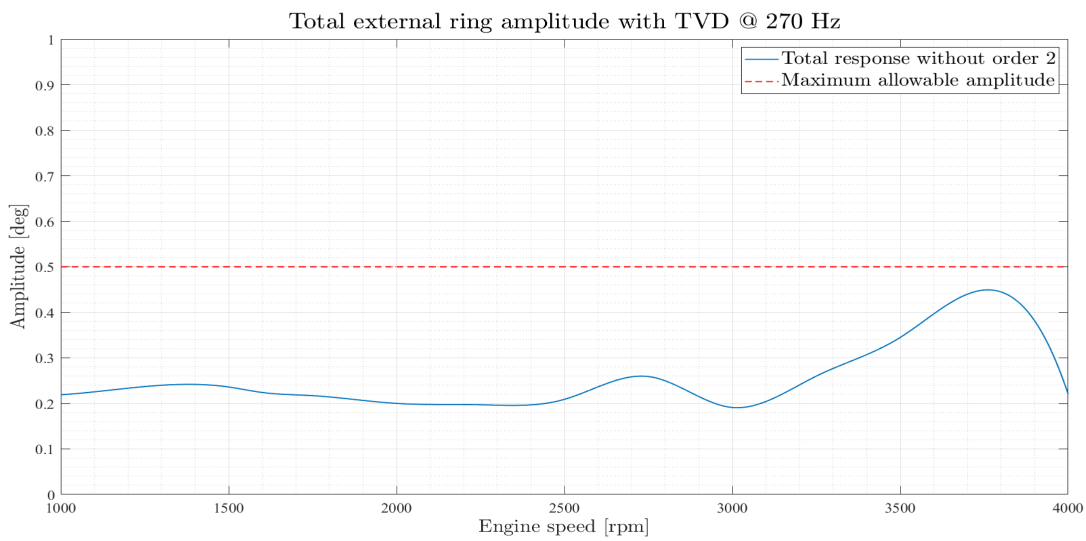

Figure 10.2: Hub external ring amplitude with TVD tuned at 270 Hz

By adding the TVD the tuned at the nominal frequency of 270 Hz the amplitude decreases to acceptable values as shown in figure 10.2.
The result is a decreased overall value of amplitude with a strong damping effect on the two peaks that were exceeding the target value. In figure 10.3, the external ring amplitudes are shown discussing the TVD effect inside the 270 ±20 Hz production range with a resolution of 10 Hz.

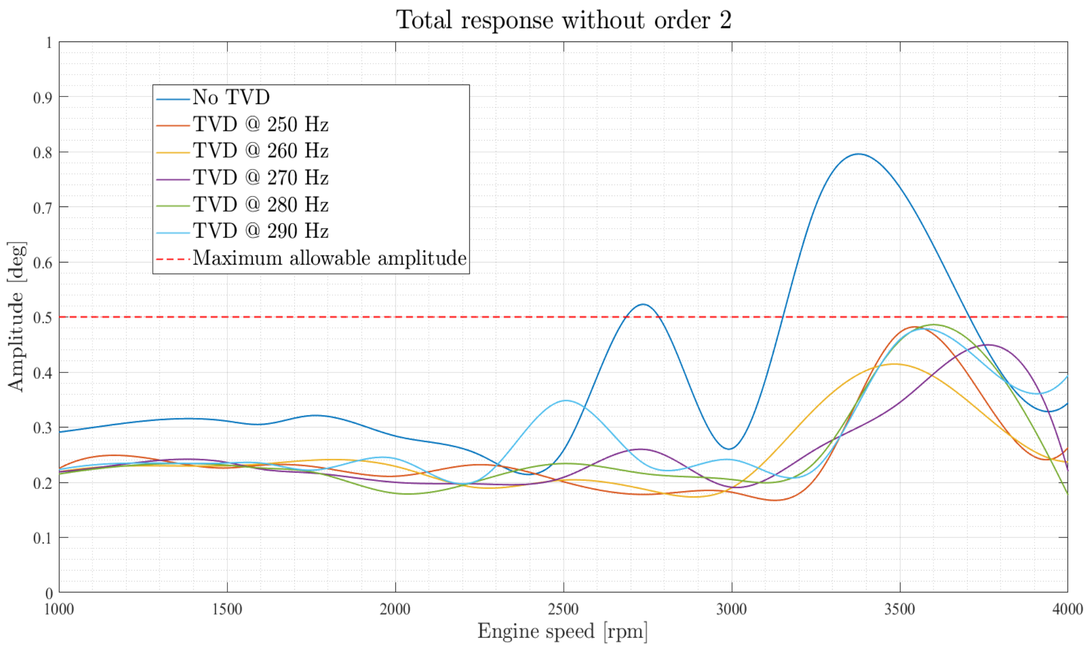

Figure 10.3: Hub external ring amplitude with different TVD tuning frequencies

As the figure shows, all the five discussed tuning possibilities are providing almost the same amplitudes. This is because there isn't a perfect tuning as the theory would suggest. When adding a TVD, the dynamic characteristics of the systems are changing since new stiffness and inertia elements are added.
Therefore, once a suitable range is found for the application it is only necessary to verify the compliance inside the whole production range. A clearer representation of the peak amplitudes for each tuning frequency is reported in figure 10.4.

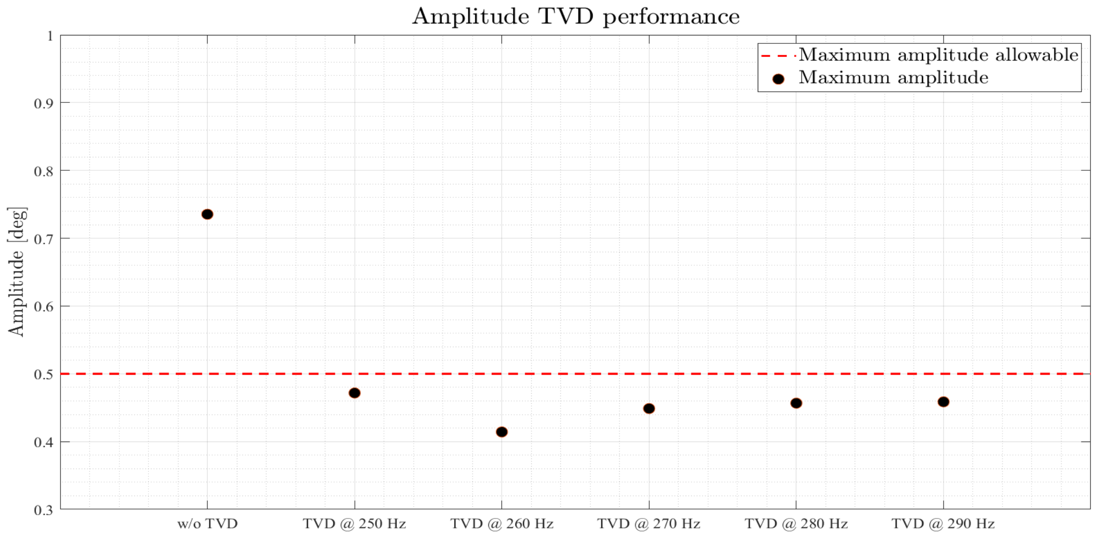

Figure 10.4: TVD performance on hub external ring amplitude

10.1.2 Internal torques

Another target involved in the TVD discussion is about the internal torques. As anticipated, a trend similar to the one of amplitudes is to be expected since the internal torque is proportional to the acceleration as equation 10.1 shows:

$$T_{\text{int}} = J \cdot \alpha = J \cdot \omega^2 \cdot \theta \tag{10.1}$$

Consequently, there exists a significant correlation between the internal torque and the amplitude. As such, an enhancement in the system performance due to the addition of a Torsional Vibration Damper (TVD) is anticipated.
The computational software employed in this study is designed to calculate the internal torque for each component of the crankshaft. To evaluate whether the desired objectives have been met, the maximum internal torque value for each rotational speed was taken into consideration.
From company's design guidelines, the limits on the internal torques are set based on the staircase test on shaft's crankpins with a maximum limit of 2640 Nm but possibily aiming to the safety coefficient of 1.5, so at 1760 Nm.
In figure 10.5 it is shown the crankpins internal torque trend as a function of the

engine speed without TVD with values clearly exceeding the maximum limit and often above the 1.5 safety coefficient.

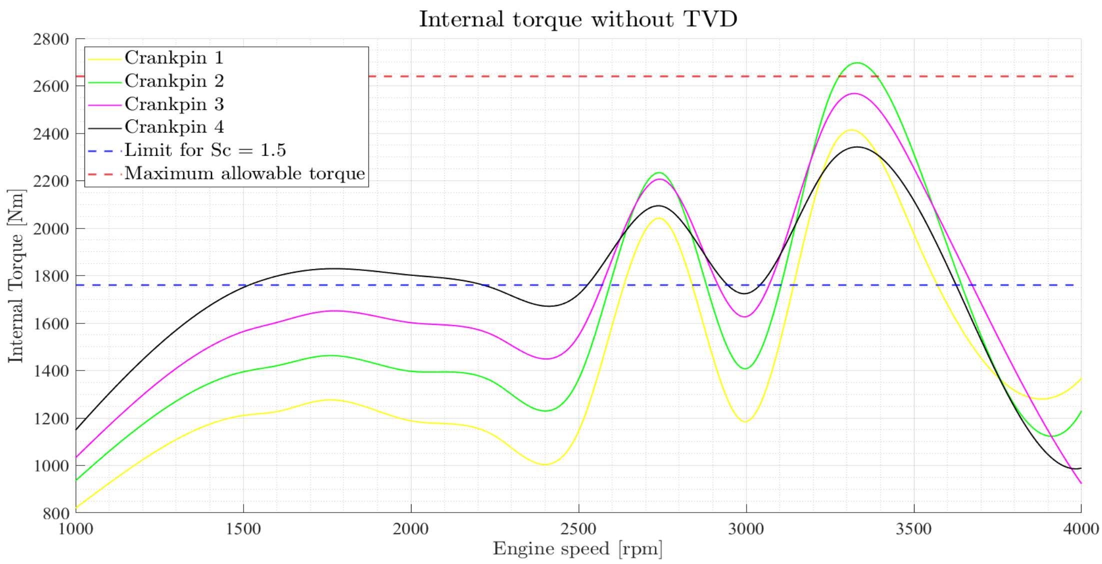

Figure 10.5: Internal torques distribution without TVD

The figure 10.6 shows the same trend with the addiction of the TVD tuned at 270 Hz.

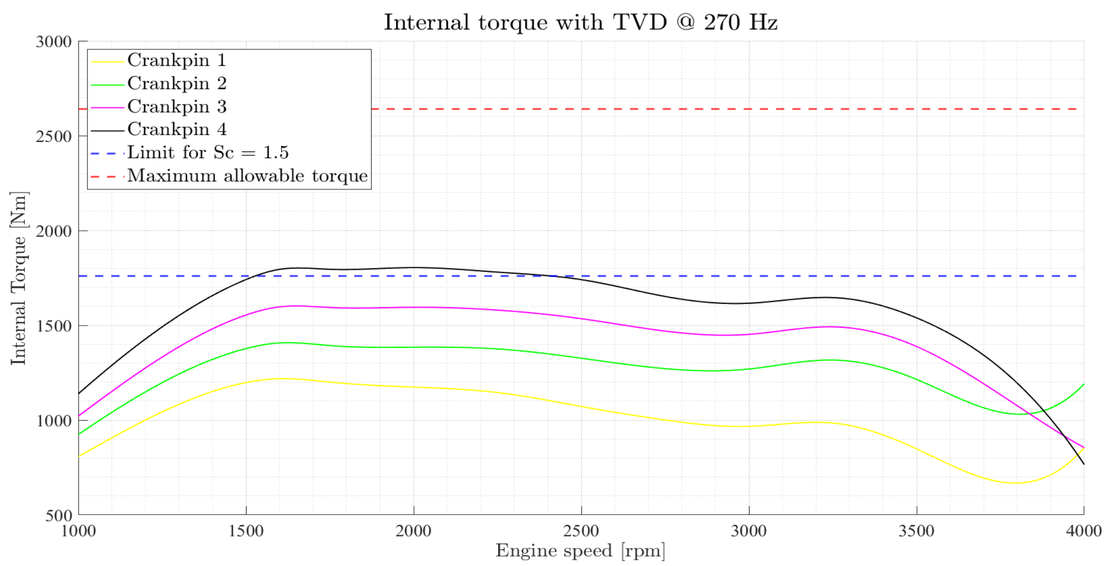

Figure 10.6: Internal torques distribution with TVD tuned at 270 Hz

As previously stated, the image clearly shows the effect of the TVD, with all the torques attenuated even below the safety coefficient limit of 1.5 with only the fourth crankpin slightly exceeding the limit.
Discussing the performance around the production frequency range, the picture 10.7 shows the maximum internal torque for each tuning frequency.

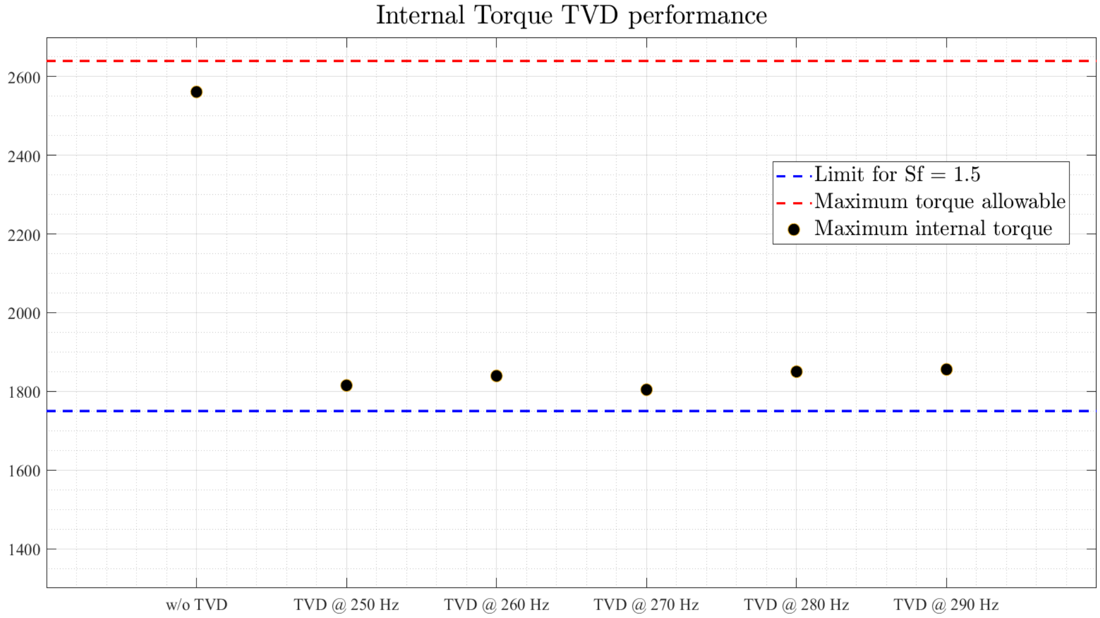

Figure 10.7: TVD performance on internal torques

As already discussed for the vibration's amplitude, there isn't a best tuning option between the possibile tuning range and all of them are providing acceptable results with maximum peaks that are just above the target value of 1.5 safety coefficient. Still, this condition is acceptable since almost all the crankpins are being subject to torques way lower than the target one. It can be concluded that this TVD tuning is satisfying the company's targets.

10.1.3 Slip torque

The last target that involves the TVD is the front-end slip torque. It is a very important target because it is necessary to guarantee the right jointing of the FEAD system on the crankshaft. This became even more important with the addition of the P0 hybrid since stronger torques are introduced.
For this reason, the company improved the tightening strength by using a four bolt connection with increased surface friction. This allowed to raise the maximum slip torque to 760 Nm and to 507 Nm with a safety coefficient of 2.
The figure 10.8 shows a recap of the TVD performance on the front-end slip torque considering the different tuning possibilities.

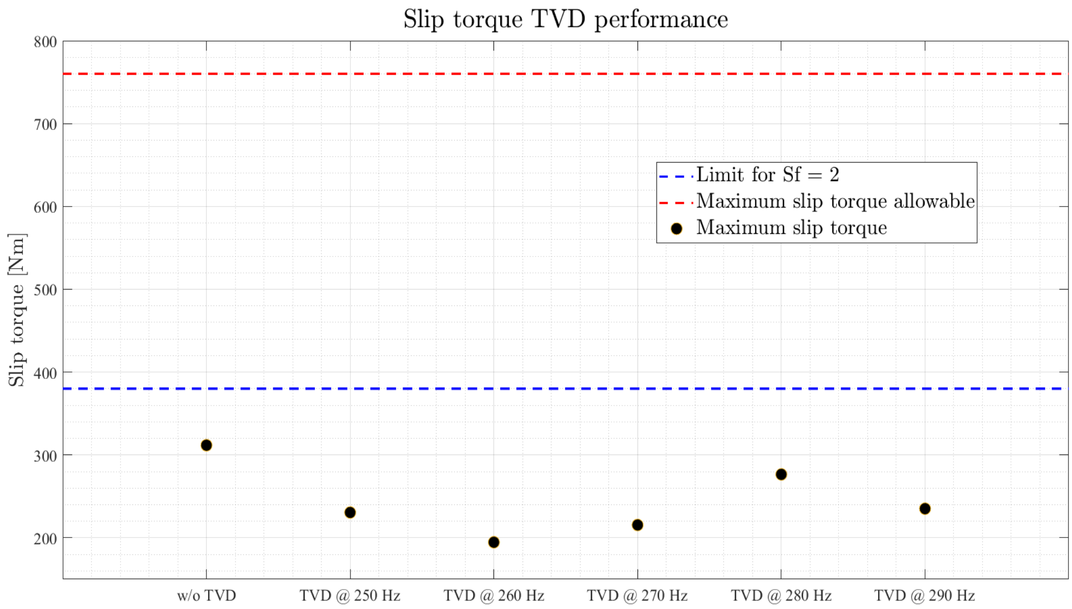

Figure 10.8: TVD performance on slip torque

Even if the TVD is decreasing the measured slip torque it can be said that it wouldn't be necessary once the new bolt connection is introduced. However, it still provides better results that can be translated into a higher safety.
It is worth to mention that the bolt connection improvement would be still needed even if it seems that the target is easily reached, hence no overdesign is beign introduced.

10.2 Decoupler effect on FEAD dynamics

As done for the TVD, the effect of adding the decoupler before the front-end pulley will be discussed with respect to the company's targets for the FEAD system that were introduced in As anticipated, these analyses were perfomed on the recuperation mode of the hybrid engine. The computations without decoupler were made rigidly linking the decoupler external ring to the crankshaft hub. In this way the inertia properties of the whole system were kept unchanged yet neglecting the decoupler effect.

10.2.1 Belt tension

The belt tension is the first focus when dealing with pulley systems because it is strictly needed for the right transmission of the torque. The company requirements for this target considered the minimum, maximum and average value of belt tension as anticipated in chapter 2.
The belt tension was computed in GT-Ise by means of a finite element discretization of the belt so that the highest accuracy could be achieved. The frequency distribution of the belt tension without decoupler is shown in figure 10.9.

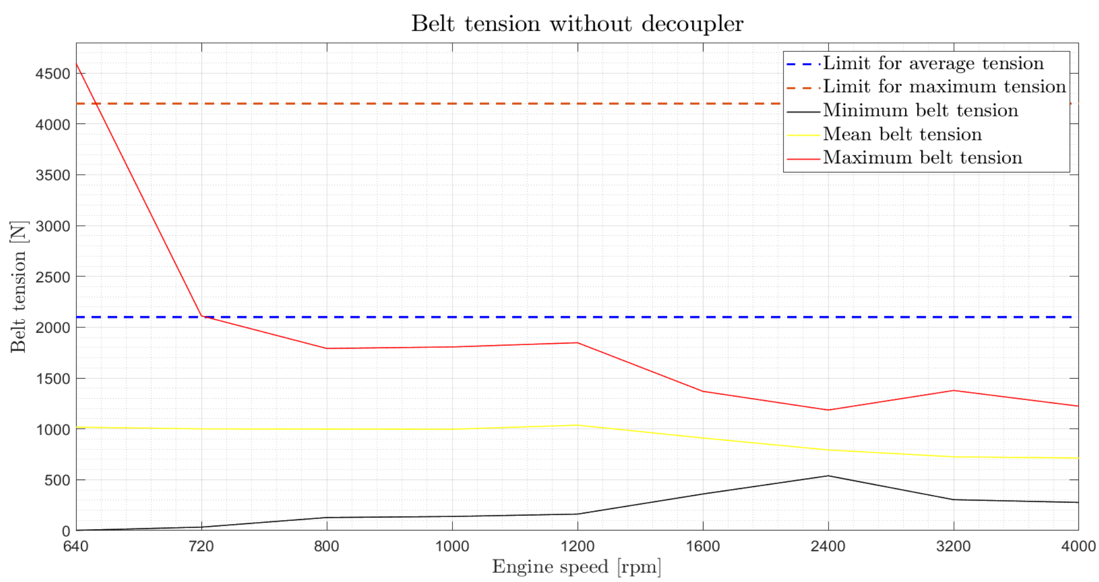

Figure 10.9: Belt tension without decoupler

Even without the decoupler this target shows good results with maximum tension exceeding the threshold only at 640 rpm and the mean tension consistently inside the acceptance range.
However, introducing the decoupler the belt tension distribution improves, as shown in figure 10.10.

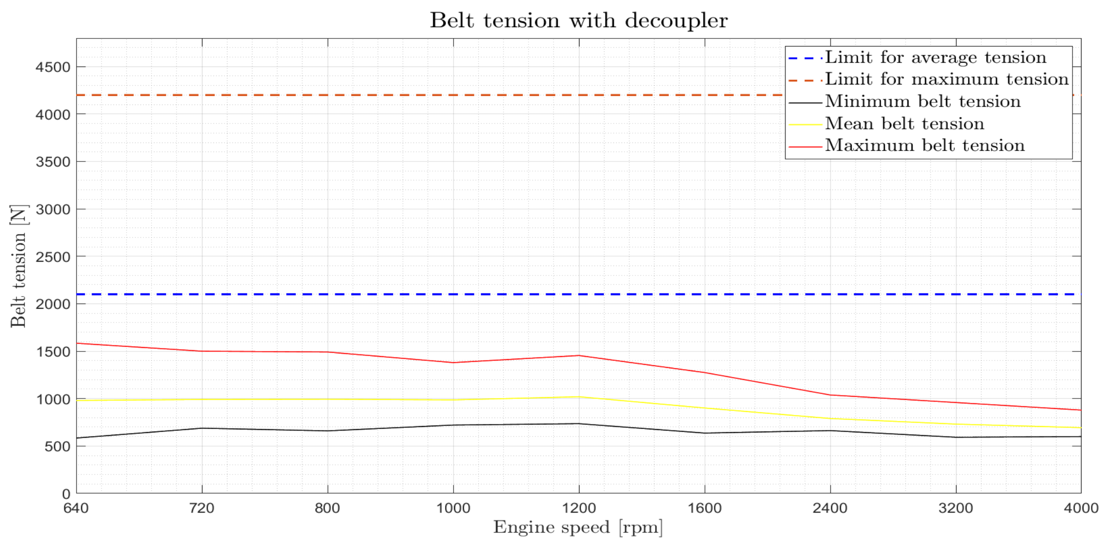

Figure 10.10: Belt tension with decoupler

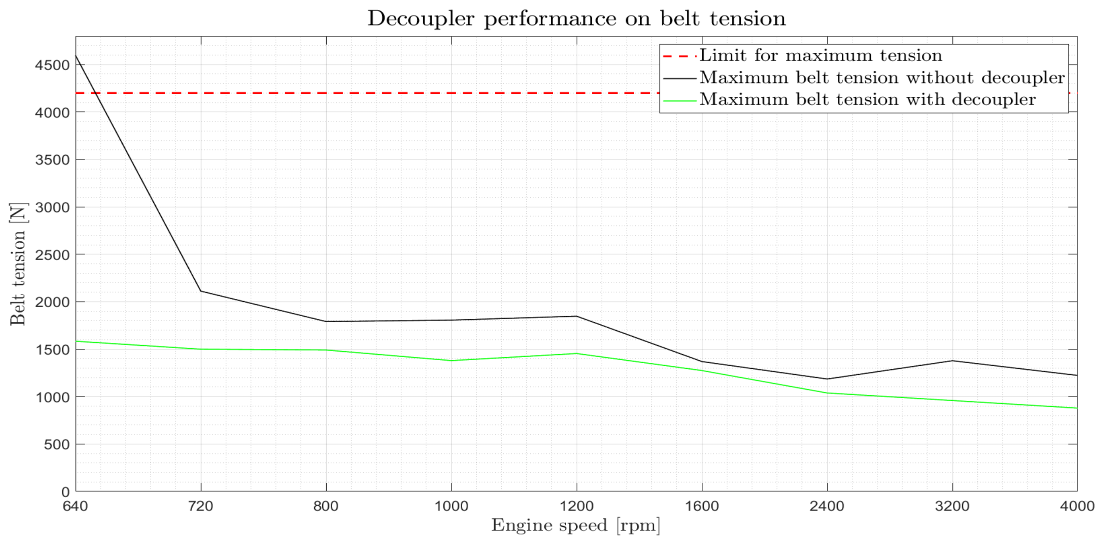

Figure 10.11: Decoupler performance on belt tension

10.2.2 Pulley global slip

The maximum tension is strongly attenuated, leading to better performances on belt life. In figure 10.11 a comparison between the decoupler is shown to highlight the decoupler action on the maximum belt tension, that is the most critical.
In addition to belt tension, the global slip of the pulley is a critical parameter that must be monitored to ensure optimal power transmission efficiency. The company has established a target global slip percentage for each pulley, with particular emphasis on the BSG pulley, as it is the only one exhibiting critical values. This is attributed to the braking torques applied to the BSG pulley during the recuperation phase.
Figure 10.12 shows the effect of the decoupler on this target.

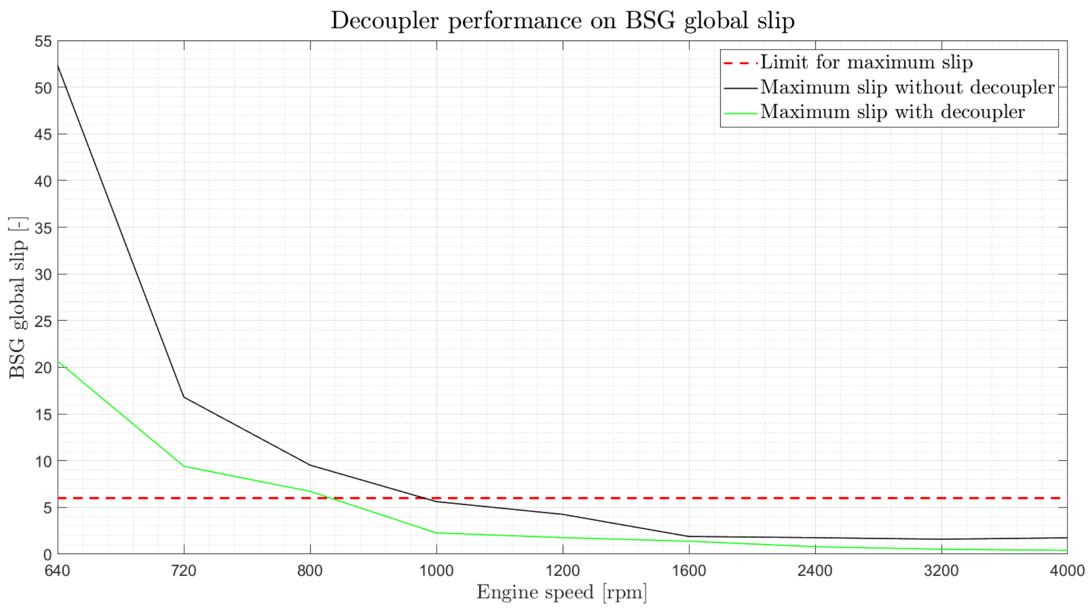

Figure 10.12: Decoupler performance on BSG global slip

The maximum slip graph exhibits peaks that surpass the acceptable thresholds for this objective. The primary issue pertains to the exceedingly low engine speeds. A high degree of slippage transpires because the engine irregularities are more pronounced at these frequencies and diminish towards higher engine speeds. Furthermore, in the model, the maximum BSG braking torques were designated as

input, which further exacerbates the BSG pulley slippage.
On the other hand, it is noteworthy that the engine will not operate at these low engine speeds very frequently and, even so, very few times would the model input torques be representative of the working condition. Furthermore, in all the summarizing plots only the worst values are being reported meaning that the results are better than shown on average.
However, the decoupler addition provides a good effect on this target with a sensible slip decrese at 640 rpm and a lower reduction when dealing with higer engine speeds. This is justified by the fact that the decoupler mainly acts on engine irregularities that decrease as the speed increases.
Nonetheless, since the virtual validation is exhibiting excessively high values, the company's subsequent course of action is to conduct a bench test to verify the accuracy of the analysis and, if necessary, transition to a different design to fulfill the imposed target.

10.2.3 Main plate rotation

The main plate peak-to-peak rotation is another target to be discussed. Figure 10.13 shows the crank angle-based main plate rotation as a function of different engine regimes without decoupler.

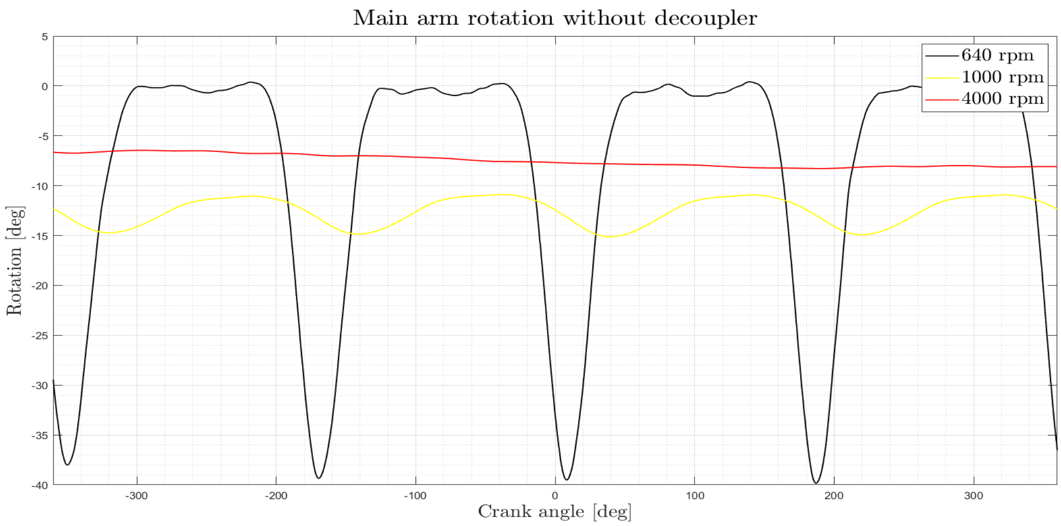

Figure 10.13: Main plate crank angle-based rotation without decoupler

The plot clearly shows the nonacceptable movement of the main plate at low engine speed with a peak-to-peak amplitude of over 35° with an acceptable 10°. Furthermore, the engine irregularities are once again highlighted at the lowest engine speeds with respect to the higher ones. The same plot changes by adding the vibrations decoupler as shown in figure 10.14.

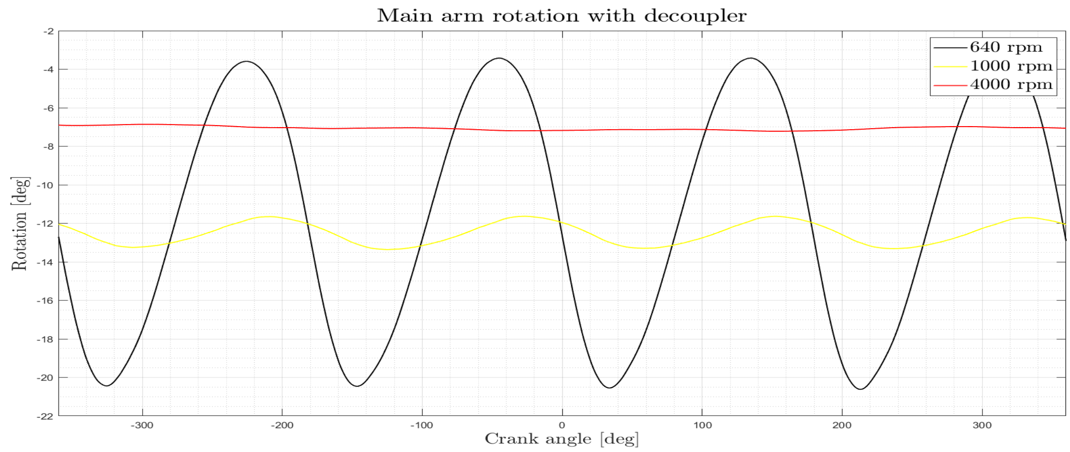

Figure 10.14: Main plate crank angle-based rotation with decoupler

The effect of the decoupler on the main plate rotation can be summed up in the following plot (figure 10.15) as a function of the engine speed.

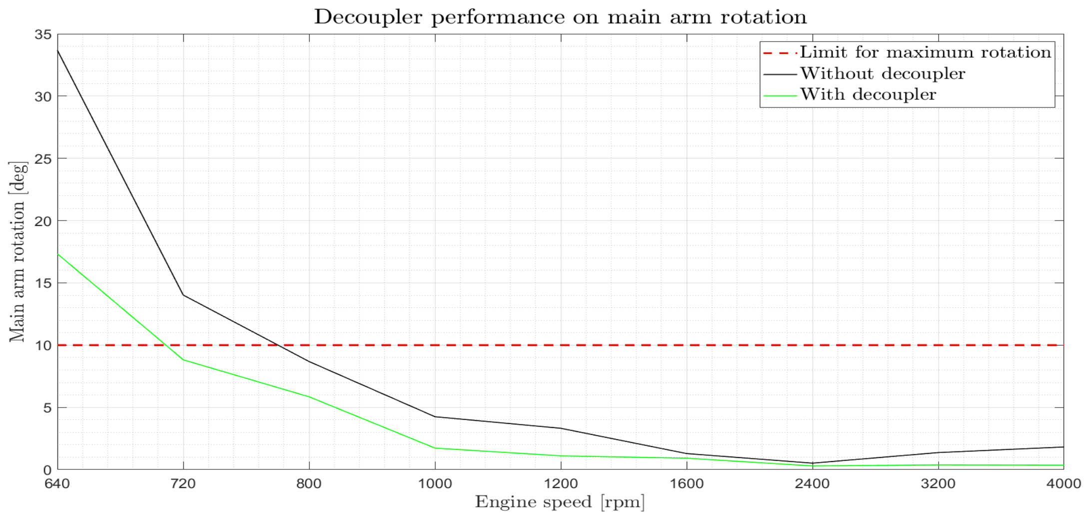

Figure 10.15: Decoupler performance on main plate rotation

As for the BSG global slip, the decoupler is strongly affecting this target but is not able to keep the rotation inside the acceptable threshold imposed by the company. This once again confirms the ability of the decoupler on damping the irregularities from the motor but not enough to filter all the peaks at low regimes. The same trend can be found for the side arm peak-to-peak rotation, which summarizing plot is reported in figure 10.16.

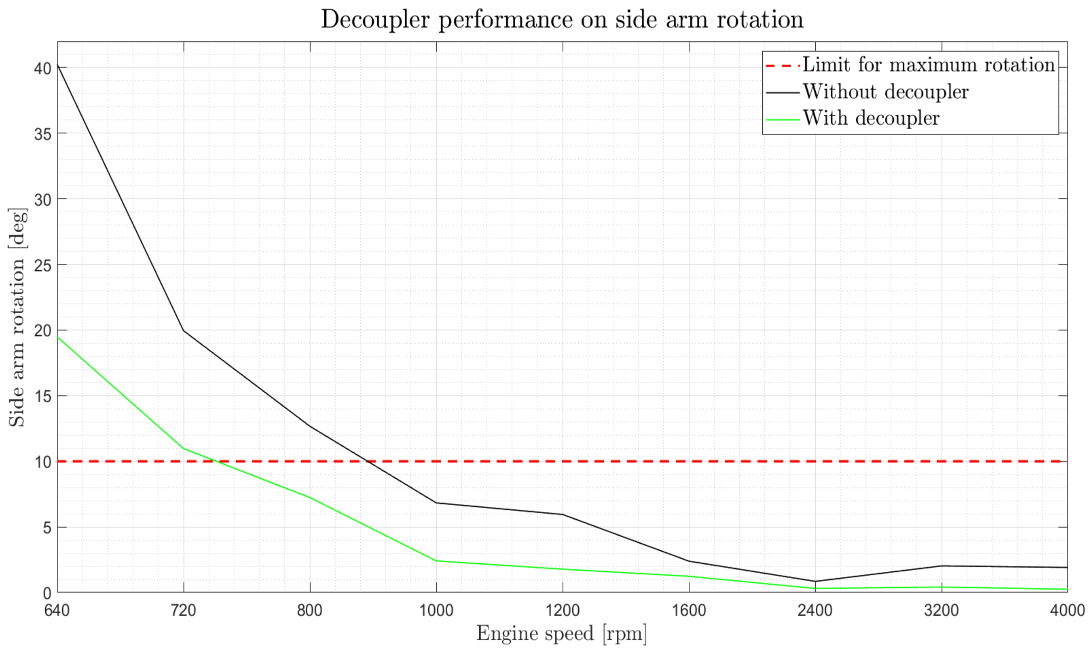

Figure 10.16: Decoupler performance on side arm rotation

10.2.4 Hubloads

From the structural point of view, the hubloads represent an important parameter to be considered. The figure 10.17 shows the maximum FEAD system hubloads without adding the decoupler.

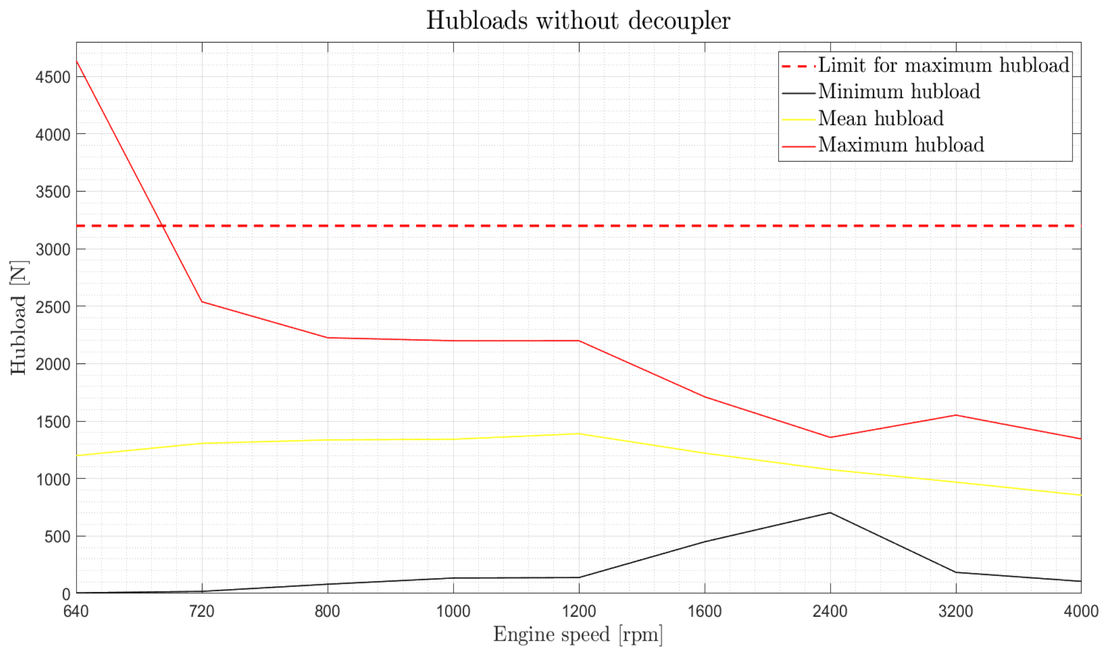

Figure 10.17: Hubloads without decoupler

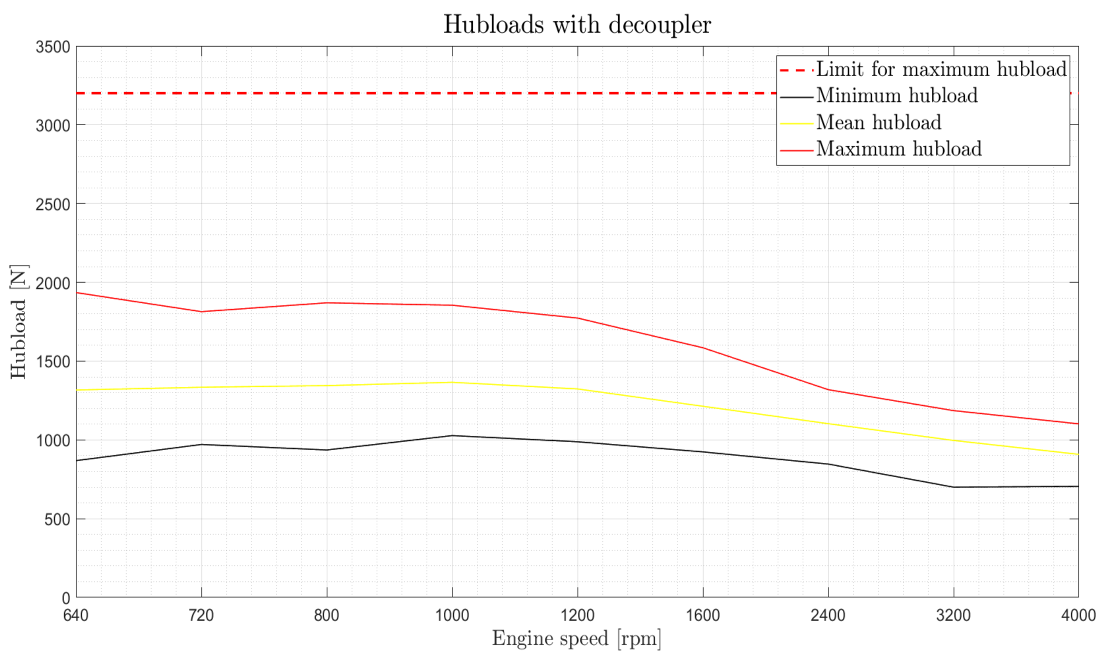

Figure 10.18: Hubloads with decoupler

Also for this target, 640 rpm seems to be the critical engine speed were the target is exceeded. Adding the decoupler a strong decrease at this range is experienced, as shown by figure 10.18.
The decoupler provides two positive effects:

1. Strongly decreases the hubloads values along all the frequency range, with a clear effect at low engine speeds;

2. Narrows the hubloads band thus decreasing the alternate component of force, providing an increase of fatigue life of the bearings.

The figure 10.19 shows the difference between the hubloads before and after adding the decoupler.

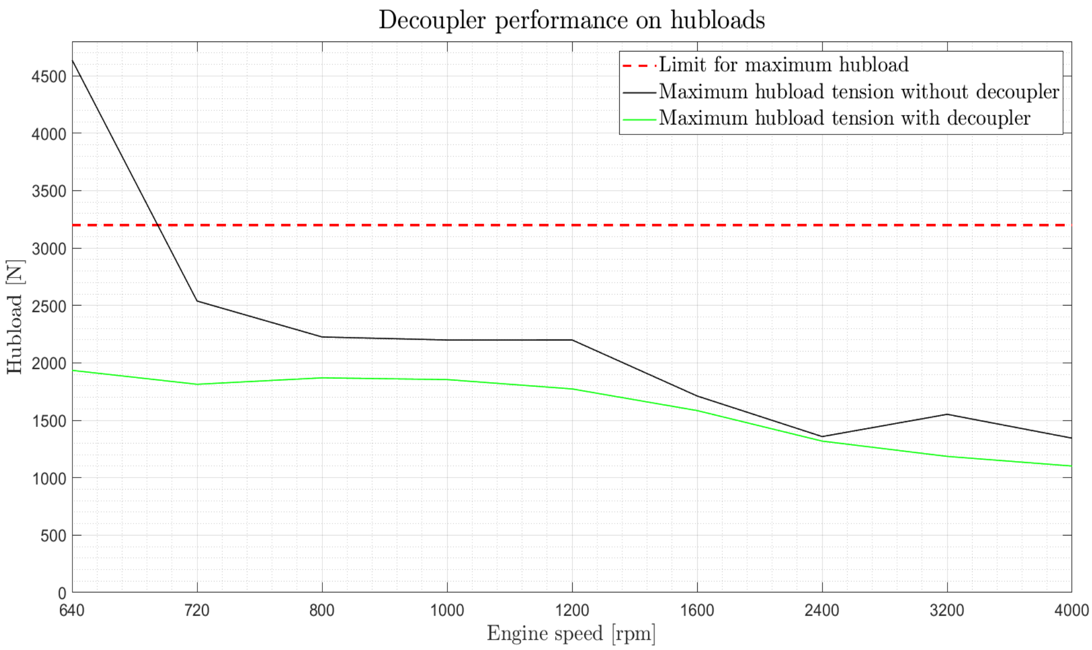

Figure 10.19: Decoupler performance on hubloads

10.2.5 Flapping

The last target to be discussed is the flapping movement of the belt while working. Even if it is a crucial parameter for what concerns the belt's corrosion, it is very difficult to be evaluated by the software.
It is computed starting from the lateral movement of the belt then relating it to the free span of the arc where the movement occurs. The uncertainty of the computation is mainly due to the belt shape and how the software manages to fit the belt on the pulleys. In this type of software is not possible to accurately define the shape of the belt, so only the physical characteristics were introduced.
However, figure 10.20 shows the effect of the decoupler on the flapping movement of the belt.

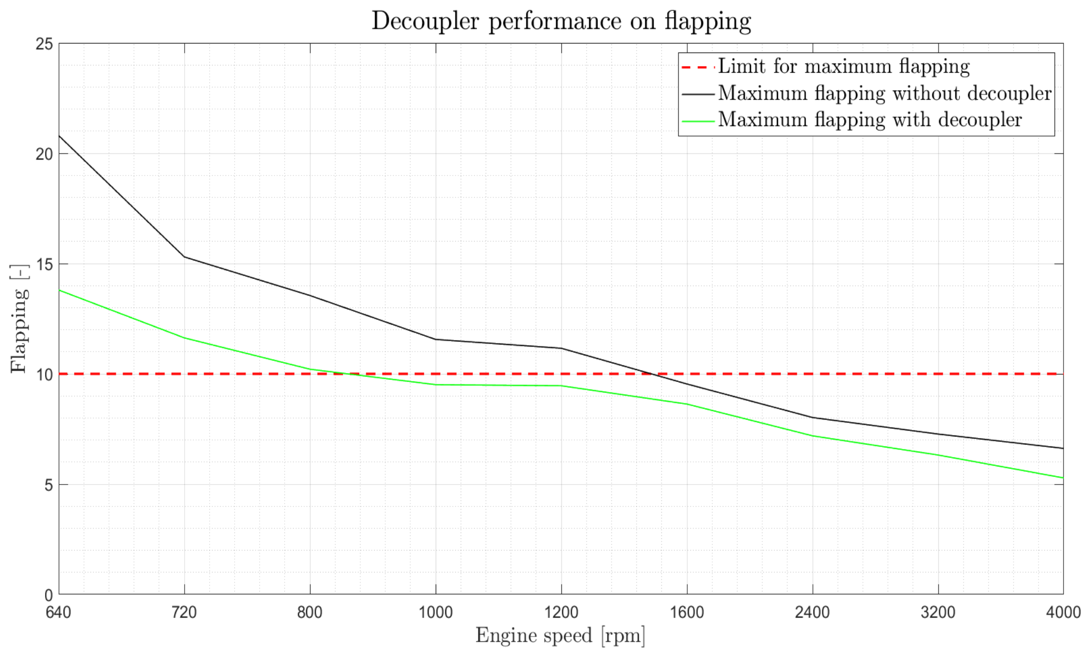

Figure 10.20: Decoupler performance on flapping

Even if there is an uncertainty on the absolute values the decoupler is clearly introducing a performance improvement, strongly decreasing the flapping in all the frequency range, again with a greater effect at low engine speeds.

Chapter 11

Conclusions

A full overview on the considered target is shown in the following two tables where the judgement criteria shown in figure 11.1 were considered:

Legend of Component Judgement		
✓	OK	(no action required)
!	Borderline	(of concern, acceptance has to be checked in detail)
✗	KO	(actions required, design modifications & further tests needed)

Figure 11.1: Legend on judgement criteria

TVD performance	without TVD	with TVD
Amplitude	✗	✓
Internal torque	✗	!
Slip torque	✓	✓

Figure 11.2: TVD performance on targets

Decoupler performance	without Decoupler	with Decoupler
Belt tension	!	✓
BSG global slip	✗	!
Main plate rotation	✗	!
Side arm rotation	✗	!
Hubloads	!	✓
Flapping	✗	!

Figure 11.3: Decoupler performance on targets

The mechanical components under consideration, namely the Torsional Vibration Damper (TVD) and the decoupler, confer significant advantages to the targets under analysis. Specifically, the TVD is indispensable for managing the magnitude of torsional vibrations and aids in maintaining internal torques below the maximum threshold. However, it does not ensure adherence to the 1.5 safety factor mandated by the company, as per simulation results.
Regarding the decoupler, it continues to positively impact Front-End Accessory Drive (FEAD) targets. Nevertheless, due to potential inaccuracies in the absolute values reported by simulations, a further examination is recommended. It's noteworthy that this issue predominantly affects low engine speed regimes, which are associated with minimal risk due to their infrequent occurrence during the engine's duty cycle.
Despite certain targets not being met across all engine speed domains, the decoupler remains a crucial component in this configuration. In line with organizational standards, additional investigations into these targets are warranted and a more efficient decoupler design may be introduced if necessary.
In conclusion, based on the provided simulations, a design incorporating both a TVD and a torsional decoupler ensures optimal system performance in terms of target compliance.

Bibliography

[1] *European Council*. URL: https://www.consilium.europa.eu/en/ (cit. on p. 1).

[2] *FPT Industrial website*. URL: https://www.fptindustrial.com (cit. on p. 3).

[3] Kibong Yoon, Jisoo Hong, and JaeYoung Shim. *A Study on Front End Auxiliary Drive (FEAD) System of 48V Mild Hybrid Engine*. Tech. rep. SAE Technical Paper, 2018 (cit. on p. 3).

[4] *Crankshaft: Parts, Function*. URL: https://www.theengineerspost.com/crankshaft-parts-and-function/ (cit. on pp. 5, 6).

[5] *Crank Mechanism overview*. URL: https://www.sciencedirect.com/topics/engineering/crank-mechanism (cit. on p. 7).

[6] *FEAD system example*. URL: https://uggadugga.com/index.php/2019/10/15/why-is-it-important-to-replace-all-front-end-auxiliary-drive-system-components/ (cit. on p. 8).

[7] *P0 mild hybrid solution by DAYCO*. URL: https://www.dayco.com/it/prodotto/bsg-mild-hybrid-solution-p0/ (cit. on p. 9).

[8] Guangming Wu, Wenku Shi, and Zhiyong Chen. «Analysis of performance parameters of torsional vibration damper under various operating conditions». In: *SAE International Journal of Passenger Cars-Mechanical Systems* 6.2013-01-1488 (2013), pp. 993–1000 (cit. on p. 17).

[9] Fasana A. and Marchesiello S. *Meccanica delle vibrazioni*. CLUT, 2006 (cit. on pp. 17, 54, 61).

[10] Giancarlo Genta. *Vibration dynamics and control*. Vol. 616. Springer, 2009 (cit. on pp. 20, 30, 31, 33, 41, 52, 62, 63).

[11] George Nerubenko. *Tuned torsional vibration damper*. Tech. rep. SAE Technical Paper, 2013 (cit. on p. 21).

[12] *Example of viscous torsional damper*. URL: `https://blog.vibratechtvd.com/blog/servicing-a-heavy-duty-engine-damper` (cit. on p. 21).

[13] Raghavan Balaji and Eric M Mockensturm. «Dynamic analysis of a front-end accessory drive with a decoupler/isolator». In: *International journal of vehicle design* 39.3 (2005), pp. 208–231 (cit. on p. 26).

[14] *Decoupler from DAYCO*. URL: `https://www.dayco.com/it/prodotto/disaccoppiatori/` (cit. on p. 26).

[15] *Single mass flywheel*. URL: `https://www.ecstuning.com/b-spec-clutches-parts/spec-single-mass-flywheel-aluminum/sb53a-2~spc/` (cit. on p. 42).

[16] *Second order tetrahedric element*. URL: `https://www.researchgate.net/figure/Example-of-a-quadratic-tetrahedron-element_fig1_270438555` (cit. on p. 48).

[17] WILSON LUIZ Guesser and LPR Martins. *Stiffness and vibration damping capacity of high strength cast irons*. Tech. rep. SAE Technical Paper, 2016 (cit. on pp. 60, 62).

[18] *Encoder working principle*. URL: `https://instrumentationtools.com/encoder-working-principle/` (cit. on p. 97).

[19] *Poly-v belt friction*. URL: `https://eng.libretexts.org/Bookshelves/Mechanical_Engineering/Mechanics_Map_(Moore_et_al.)/06%3A_Friction_and_Friction_Applications/6.07%3A_Belt_Friction` (cit. on p. 105).